

3. Blast vibration and seismology

A comparison of recent and previous pipeline blasting studies

C. Dowding

Northwestern University

T.A. Davidsavor & D.A. Provost

Barr Engineering Co.

Y. Gou

Central South University

ABSTRACT: When blasting is conducted adjacent to operating pipelines the main concern for those pipeline operators is that the pipeline is not subjected to ground motion that causes damage or over stresses the pipeline. Several studies have been conducted over the past few decades that have recorded and analysed the strains on the pipelines during blasting. These studies include surface mining blasts and response of several segments of steel and plastic test pipeline, trench blasts with small number of holes and response of water lines and decommissioned steel, and a Barr 2016 study involving trench blasting with over 50 holes parallel to and in between to two operating pipelines. This paper reviews the difference in the studies, compares observed peak particle velocity measured at surface seismographs to measured pipe strain and stress, as well as strain and particle velocity time histories. Similarities and differences of the findings are discussed. Each study indicated blasting was performed successfully without apparent damage or overstress of the pipe even at relatively low scaled distances as long as the pipe being monitored was outside of the crater zone of the blast.

1 INTRODUCTION

This paper compares measurements of strains in large diameter welded steel pipelines produced by actual trenching blasts having more than 50 holes per blast with three other theoretical studies to confirm the measured and calculated strains. Additionally, the paper comments on the intricacies of strain measurement as well as the fact that damage in the pipelines was not observed. The four studies evaluated in this paper were conducted at scaled distances between 1.0 and 30 ft/lb^{1/2} (0.5 to 14 m/kg^{1/2}) and produced strains

above 10 μ strain and peak particle velocities above 1 inch per second (ips) (12.7 mm/s). Some of the blasts were detonated as close as 4 ft (1.3 m) from the pipeline and produced strains as high as 300 μ strain. Strain and peak particle velocity attenuation relationships are compared on the same scaled distance graphs for all four studies to illustrate the effects of geology and shot type. Measured strains are compared between the studies to investigate the proper interpretation of strain time histories. Maximum stresses are calculated for comparison with the specified maximum yield stress of the pipes.

Table 1. Summary of blast parameters.

Parameter	Unit	SwRI	Study			
			USBM	VME	Barr 2016	
Number holes	Average	15	50	6	39	61
Depth holes	ft	16	40-65	10		12
Diameter holes	inch	3	10-12	?		3
Burden	ft	6	15	varies		5
Spacing	ft	6	15	varies		2.5
Total explosive wt.	lb	~225	~900	15-50	255	501
Typical no. of delays		15	20	2	78	122
Delay interval	ms	25	126-rw/ 25-hl	~1000		8
Explosive type		60% Ex Gel	ANFO?	?		Emulsion
W per delay min.	lbs	15	668	5	2.5	3.75
W per delay max.	lbs	20	964	19.5	4.16	5.83
Rock type		Igneous	Shale	?		Limestone
Depth of trench	ft	~5	~5	~5		~10
Soil thickness	ft	<5	7	2		0
Pipeline diameter	in	30	20	34		20 & 36
Pipe wall thickness	in	0.47	0.26	0.31		0.34
Pipe steel yield, σ_y	ksi	?	56	42		46

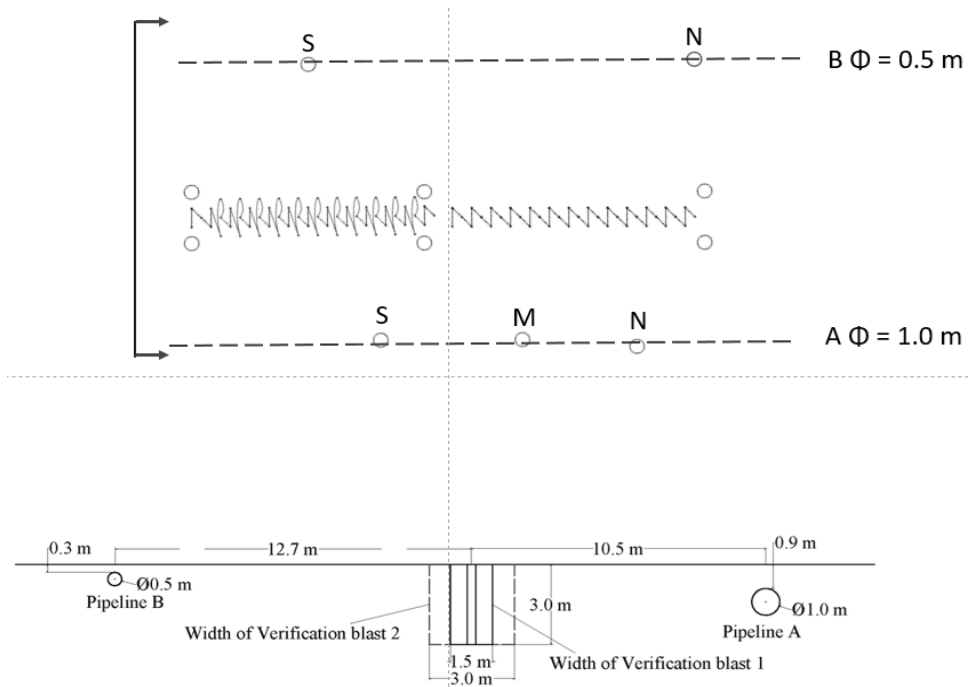
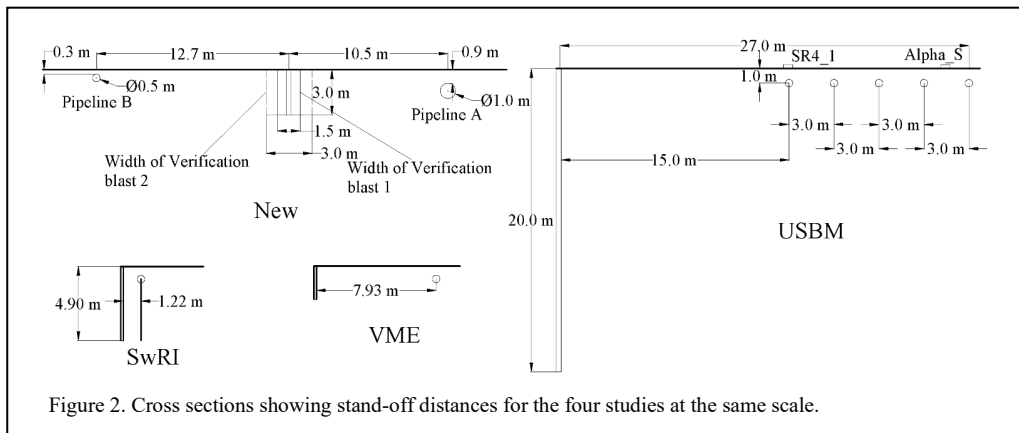


Figure 1. Blast hole and pipe measurement locations (top) and elevation view showing the stand-off distance and pipe depth (bottom) for the Barr 2016 study.



2 BACKGROUND AND BLAST DESIGN AND GEOLOGY DIFFERENCES

Details of the four studies are compared in Table 1 and the shot geometries are compared in Figures 1 & 2. More details on the Southwest Research Institute (SwRI), United States Bureau of Mines (USBM) and VME studies can be found in Dowding and Akkaya (2001) and the more recent Barr 2016 study in Davidsavor and Provost (2020).

As can be seen in Figure 1, the two shots in the Barr 2016 study differed in their design. Holes in the Barr 2016 verification blast 1 were designed as a 5 ft (1.5 m) ‘5 spot or 5-of-dice’ pattern while Barr verification blast 2 was designed as a 10 ft (3 m) wide reoccurring 3 then 2 holes per row down the length of the blast. The change in pattern was to assess the geometric responses in preparation for future blasting on the project.

As can be seen in Figure 2, the blasting geometry of the USBM surface mining study differs radically from that of the trenching geometry of the SwRI, VME, and Barr 2016 studies. The 800 to 900 lb (360 to 410 kg) per delay detonations associated with mining in the USBM study result in large stand-off distances from the pipeline. This would be expected as the USBM study focused on the effects of mining-related blasting produced by mining pattern blasts on pipe stress, whereas the other studies focused on the effect of pipeline-construction trench blasting on adjacent pipelines. Even though the scaled distances are similar for the three previous studies, the stand-off distances for the mining shots are large in an absolute and wavelength scale.

The rock type across the four studies varied considerably. The USBM mining study involved shots at a coal mining area in shale. The SwRI

trenching study did not identify the rock type, but photographs indicate that it was unlikely to be sedimentary and was most likely igneous. The VME study also did not identify the rock type, and unfortunately, there were no photographs provided to allow visual identification. However, this study was conducted for a Seattle, Washington area municipality, so the rock type is likely to be either igneous or metamorphic. The Barr 2016 study was conducted in limestone in support of active pipeline construction.

Shot designs across the four studies varied considerably. As shown in Figure 2, hole depths for the mining study were some 66 ft (20 m) deep while those for the trenching studies were only some 6 to 10 ft (2 to 3 m) deep. None of the SwRI, USBM or VME shots involved any decking. The Barr 2016 shots were decked with 1 ft to 1½ ft (0.3 m to 0.5 m) of crushed stone stemming. Only the VME study involved more than one hole being detonated at the same delay, although the use of ¾ to 1 second delay intervals in the VME study resulted in non-simultaneous detonation in several instances. The USBM and SwRI studies employed standard 25 millisecond delay intervals between single blast hole detonations. The Barr 2016 study employed nonelectric initiation with 17 ms interhole delays and 25 ms decking delays, all with 350 ms down hole delays. This resulted in nominal 8 ms separation between any individual charge. The Barr 2016 study represents present-day large-scale pipeline blasting practices.

3 INSTRUMENTATION DIFFERENCES ACROSS THE STUDIES

Instrumentation across the studies was relatively similar. Strains were measured with wire strain gages in all four studies. Both weldable and epoxy mounted gauges were employed in the USBM

study. Although not described explicitly, it appears that the strain gages were epoxy mounted for the SwRI study. The VME study employed weldable gages. The Barr 2016 study employed epoxy mounted strain gages. All four studies employed standard blast vibration seismographs. Unless modified, standard seismographs may not return sufficiently accurate readings in particle velocity environments above 5 ips, which compromised the measured PPVs in the SwRI study at small stand-off distances.

The more recent Barr 2016 study involved more intensive instrumentation of strain gages and seismographs. Above each strain gauged location, two, three-axis velocity transducers were located; one just above the pipe and the other 10 to 12 in (25 to 30 cm) below the ground surface. All seismographs were placed on and in native soil that was compacted with significant effort. Particle velocities reported herein are those of the shallow burial velocity transducers, as opposed to the transducers nearest the pipe. Two sets of strain

gages were located at the crown and each side of the pipe. Only the largest of the longitudinal and hoop strains is reported herein as was the case for the other studies.

The cross sections in Figure 2 do not reveal sufficiently the differences in the full shot geometries as well as does a plan view of the blast hole locations relative to the distance to the pipelines being monitored. Figure 3 presents blast hole geometries at the same scale and demonstrates uniqueness of the Barr 2016 study. While the other two studies that involve trench geometry are similar in location, they involve fewer blast holes in much shorter segments. While the USBM blasts involved a similar number of holes, the spacing, burden, and stand-off distance of the surface mining blast are much greater. The overall location, geometry, and arrangement of the holes and explosives in the Barr study are more typical of a production blast for a pipeline trench excavation blast.

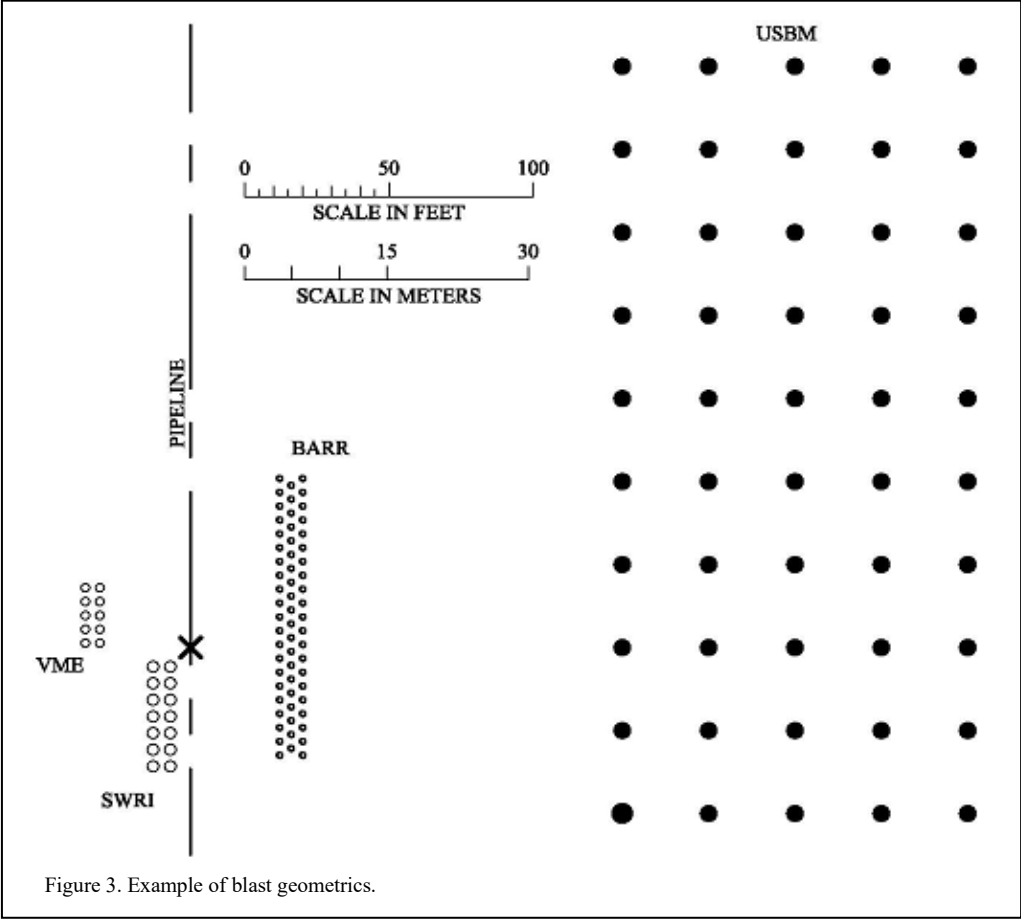


Figure 3. Example of blast geometries.

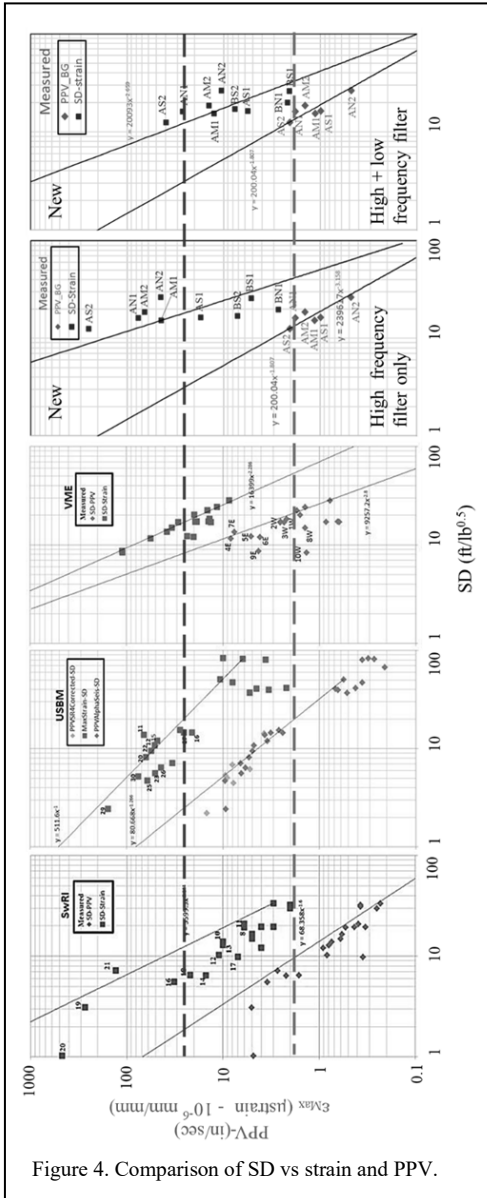


Figure 4. Comparison of SD vs strain and PPV.

4 RESULTS

4.1 Peak particle velocity

Attenuation relations for the four studies are compared in Figure 4 beginning on the left (lowest) with SwRI, and then moving right (upwards) USBM, VME, and Barr 2016 twice on the right. This order will be maintained throughout the discussion. As described earlier, the USBM blasts were those from surface coal mining and involved charges per delay of some 850 lbs (400

kg) per delay, while the SwRI, VME, and Barr studies reflected trench type construction with some 4 to 15 lbs (2 to 7 kg) per delay. Figure 4 provides a comparison of the attenuation of peak particle velocity (grey diamonds) and strain (black squares) of the single and multiple pulse interpretations of the Barr study (rightmost two graphs) and the other three (left three graphs).

Differences in PPV attenuation rates and amplitudes result from the differences in the geology, excavation and blast hole geometry, explosive type, as well as initiation sequence, and powder factor. In addition, some velocity transducers from the previous studies may not have responded properly at high PPVs. The effect of shot design will be discussed later in the section dealing with time histories. For instance, the PPV in the VME study decays more rapidly and has a higher PPVs at the same scaled distance as the other studies. The nearly seconds-long delay between velocity peaks indicates that the blasts may have involved tunnel delays rather than the more standard millisecond delays used in modern pipeline blasting. PPVs in both the SwRI and USBM studies at scaled distances below 5, fall below the attenuation slope projected from larger scaled distances. Many velocity ‘geophones’ ‘pin-out’ at PPV around 4 ips. The Barr 2016 study has the lowest PPVs at the same scaled distance and was detonated with NONEL initiation with 350 ms downhole delays with 8 ms surface delay sequences. None of the studies evaluated in this paper included the use of newer electronic delays.

4.2 Maximum strains

Despite the fall-off of the measured PPVs at small scaled distances, Figure 4 shows that the strains in all four comparative studies continue to increase according to a power function. The y axis on these graphs represents both PPV and maximum strain and requires an explanation. The whole numbers have different decimal values. The PPV whole numbers are in inches per second. The strains are micro strains or 10^{-6} times the whole number. Thus, shot 19 in the SwRI study produced a PPV of 5 ips (125 mm/s) and a strain of some 180 micro strain.

For the most part, maximum strains at small scaled distances continue to follow the power law determined from scaled distances greater than 10. There are only two shots (both in the SwRI study) that do not follow that observation in this suite of data. The two exceptions are shots 19 and 2. These two shots and shot 20, which was detonated within

4 ft (1.25 m) of the pipeline and at a distance of one quarter of the 16 ft deep blast holes. As will be discussed later, this geometry for shot 20 places the pipeline in the crater zone, and thus is not representative of prudent design or actual practice.

There are two plots of attenuation of strain for the Barr 2016 study on the right side of Figure 4. These two different interpretations of the measured strains are presented because of the techniques employed to extract peak strains from the recorded noisy time histories. They result in a single (second to the right graph) and multiple pulse strain time histories (furthest right graph). Details of these extraction techniques are not included in this paper due to space constraints. They are available upon request from C. H. Dowding or Y Gou.

4.3 Maximum Stresses

Blast induced stresses are compared in Figure 5 in the same order as were strains. Comparison of stresses calculated with the biaxial stress-strain equation (black dots) with the single and multiple pulse interpretations of the Barr 2016 study (rightmost two graphs) and the three comparative studies (left three graphs) are shown. Since only deformation or strain can be measured, stresses must be calculated regardless of the approach. Some approaches to calculating stress are more direct and more closely related to the strain, which can be measured. The calculation most closely related to the measured strain is that calculated by the biaxial stress-strain relationship, which is represented in the Barr 2016 study by the black filled circles in the three comparative studies. The equation shown in the key demonstrates the use of the hoop and longitudinal strains (ϵ_{hoop} , ϵ_L) in combination with the modulus of elasticity, E , and Poisson's ratio, ν . In the four comparative studies, maximum strains, no matter the time of occurrence, passage of the blast wave, or its sign value (positive or negative) are added to calculate the stress. Common time of the strain gauges in the Barr 2016 study have allowed calculation of stress hoop and longitudinal at the same ms time.

The other two methods of calculating maximum stress are both based upon some type of scaled distance relationship. The SwRI method, which is the most commonly used industry approach due to simplicity, is represented by the open circles in Figure 5. Stresses calculated through the compliant ground strain approach is represented by the filled squares. This method is explained in detail in Nyman, *et al.* (2008) and is abbreviated as NDO. Details of these other

methods and their use with these comparative data can be found in Dowding and Akkaya (2013) and will not be discussed further because of space constraints.

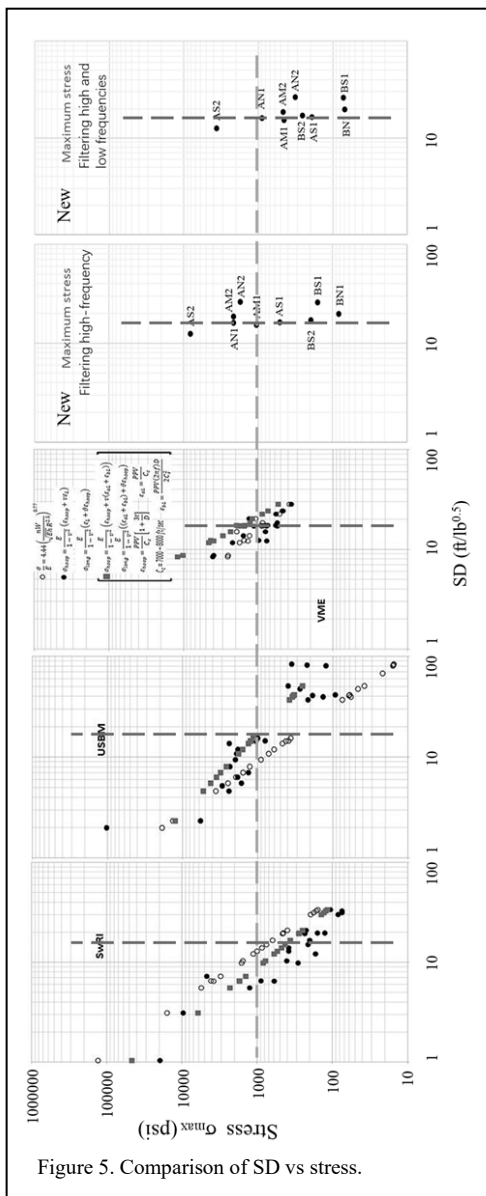


Figure 5. Comparison of SD vs stress.

As was the case with the strain – scaled distance plots, there are two plots of attenuation of stress for the Barr 2016 study on the right side of Figure 5. These two different interpretations of the calculated stresses results from the two different techniques for extracting peak strains from the noisy strain time histories. Implication of the

differences in calculated stresses will be presented in the discussion section. Both techniques result in stresses that are small with respect to the specified minimum yield stress of the pipes in the Barr study.

5 INTERPRETATION OF STRAIN TIME HISTORIES

The interpretation of the Barr 2016 strain time histories shown in Figure 6 involves three different considerations: the high noise level of the strain readings, the unusual nature of the strain shape after high frequency filtering, and the offset of the average during the recorded two seconds. Both longitudinal (top in Figure 6) and hoop/circumferential (bottom) strain time histories are shown. As shown in Figure 4, one of the highest pipe responses occurs at location AN1 (maximum response to blast 1 at position N on pipe A) The raw signal on the left in Figure 6 demonstrates the high ratio of noise to signal even for one of largest pipe strain responses.

Figure 6 compares raw and filtered pipe response strain time histories in the Barr 2016 study to blast 1, recorded at pipe A, position N (AN1) showing effects of filtering of high frequencies and filtering of high and low frequencies. Filtering of the high frequency noise shown in the centre of Figure 6 presents the resulting single pulse pipe response.

This single pulse for the high frequency filtered AN1 response is unusual as shown by the comparisons in Figure 7 with other measured pipe

responses at similar absolute and scaled distances. The single pulse pipe strain response, AN1 is shown in the top right of Figure 7. Particle velocities AN1 are shown on the bottom left. Pipe strain response and particle velocity ground motions at the pipe measured by VME from the 10-hole, 3-delay blast is shown in the centre. As shown in Figure 4 and Table 1, shot and pipe geometry and charge weights per delay are similar to the VME study. Yet, filtering of only the high frequencies results in a single pulse response for AN1 while the VME measurements result in multiple pulse pipe responses. Furthermore, the particle velocity time histories for AN1 at the pipe show multiple responses as do the VME measurements. Comparison of single (top right) and multiple (top left) interpretation of the Barr AN1 strain time histories with those from VME (centre) and the closest SwRI shot (4 ft, 1.25 m) within the crater zone (bottom right) demonstrate the unusual nature of the single pulse interpretation of the Barr 2016 AN1.

Comparisons of shot geometry and scaled distances with the other studies demonstrates that the single pulse interpretation of the AN1 distortion requires further discussion and verification. The only other single pulse strain time history of full-scale field response was produced by a 13 hole shot recorded on an inoperative pipe by SwRI shown the bottom right of Figure 7. In this instance the pipe was closer than one blast hole length as shown in the comparisons of elevation views of the blast hole – pipe geometry of the four studies in Figure 2. AN1

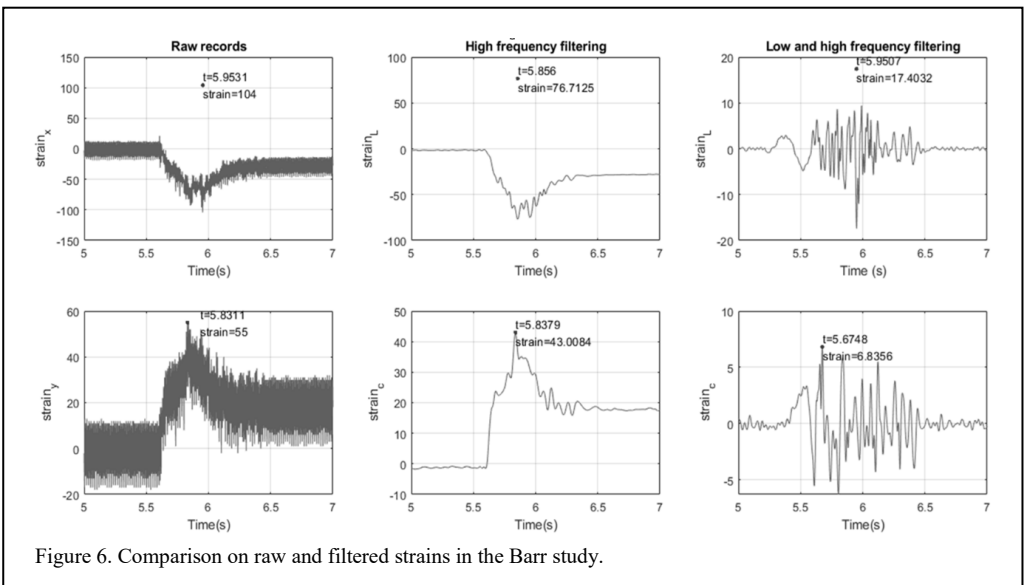


Figure 6. Comparison on raw and filtered strains in the Barr study.

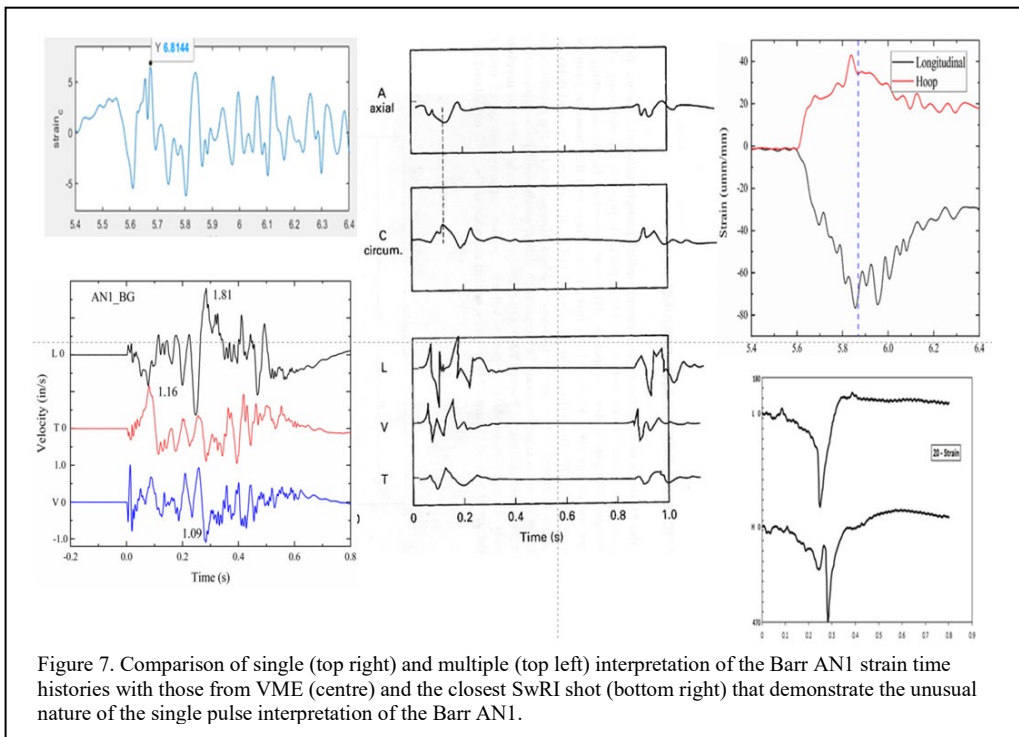


Figure 7. Comparison of single (top right) and multiple (top left) interpretation of the Barr AN1 strain time histories with those from VME (centre) and the closest SwRI shot (bottom right) that demonstrate the unusual nature of the single pulse interpretation of the Barr AN1.

was more than three blast hole lengths away. The scaled distance for the close SwRI shot was 1 (shot 20), whereas it is much greater (scaled distance of 17) for AN1 in the Barr 2016 study.

Comparisons of blast hole-pipe proximity and scaled distances of AN1 with the other-responses indicate that filtering of the low frequency component of the single pulse AN1 in the upper right of Figure 6 should be considered seriously. Time histories on the right side of Figure 6 show the results of filtering both the high and low frequency components of the raw strain time histories. In the left of Figure 7 one second of the hoop strain time history after both high and low filtering (top left) is compared with the particle velocities at the pipe (bottom left). The length of the velocity time histories is about 0.6 seconds. Whereas the length of high and high and low frequency filtered strain time histories is about 0.8 seconds.

The strain remaining at the end of the two seconds of recording in Figure 6 also requires discussion. Filtering only the high frequencies preserves the offset whereas filtering of both the high and low frequencies does not preserve the offset. The strain offsets are less than half of the peaks associated with the high frequency filtering interpretation. None of the other studies discuss or

present offsets of this nature except for shot 20 from the SwRI study at a scaled distance of 1. The question then becomes, what is the significance of these offsets? Long term measurements of crack displacement in structures (Dowding 2008) show that long term temperature and humidity distortions are significant and overwhelm any short-term offsets shown in AN1. Interpretation of the significance of the offsets requires knowledge of the long-term thermal responses of the pipelines to changes in both environmental and operating conditions including pressure and installation stresses.

The USBM study does not discuss an issue with a high frequency noise or offsets. Data logging instrumentation for the USBM study was housed in a field shed to which grounded AC power was provided. The USBM pipes were short and were isolated sections, not part of an active line. Power for the Barr 2016 project was provided by a field generator which may not have been sufficiently grounded. Additionally, pipelines monitored in the Barr study were the only operating pipelines and were subject to currents associated with cathodic protection, which induced noise. Thus, in future through additional monitoring and analysis including baseline monitoring of the cathodic signature and effective

filtering, it is possible to believe that this noise can be eliminated from subsequent full-scale tests. Ultimately, the effect of the noise of the cathodic protection on Barr 2016 active pipe is not fully understood. In either regard, effects of the strain offset were not noticeable in the pipe operation.

Comparison of the attenuation of both peak particle velocities and strains in Figure 4 of the Barr study and the other three studies provides another perspective of the two interpretations of the strain time histories. High vs. high & low frequency filtering or single vs. multiple pulses are shown in the two rightmost attenuation plots. Compared to the other three studies, the Barr 2016 study's single pulse interpretations produce strains that are unusually high for both 1) scaled distances at which they were measured as well and 2) peak particle velocities (PPV) with which they are associated. The multiple pulse interpretation of the strain time histories more closely matches strains measured in the other studies at similar scaled distances (vertical lines). They also better match the strains associated with similar PPVs. This comparison is highlighted with the horizontal (same strain) horizontal (same PPV) in Figure 4 and vertical lines (same scaled distance) in Figure 5.

6 CONCLUSIONS

The recent Barr 2016 study most closely represented actual blasting conditions during pipeline construction for nearby blasting as the work was conducted for an actual pipeline replacement project in field conditions under typical constraints and realities of a pipeline right-of-way. The scaled distances and offsets were practical and effective at achieving the desired excavation while limiting ground vibrations. While pipe stresses varied across the four studies, the maximum strains at small scaled distances continue to follow the power law attenuation relationship determined from scaled distances greater than 10. The only exception to this consistency was the SwRI study which included two measurements within the crater zone. Designing a pipeline trench or construction blast where the pipe being monitored is within the crater zone of the blast should be allowed only in extraordinary and highly controlled circumstances (e.g. near high yield strain plastic pipe). Additional studies are needed that focus on pipelines that are either in service or are adequately constructed to reflect field conditions.

Establishing a limit of peak particle velocity and measuring ground vibrations near pipelines at

the ground surface is the present industry accepted approach for blasting near pipelines. The vibration limit set for each project varies widely across owner, segment of pipe, and purpose (whether they require blasting for their own new installation or maintenance, or others are blasting for a project near their facility). Technological advancement in both monitoring equipment and data processing allow for faster interpretation of directly measured pipe strain (and therefore stress) measurement. Ultimately blasting near pipelines is constrained by regulations limiting induced stress. Measuring the induced strains (and calculating stresses) provides a more direct means of calculating induced stresses than measurement of ground vibration (and subsequent calculation of ground strain and stress). Challenges in exposing the operating pipe and installing direct-mount strain gages will remain, but continued strain monitoring while performing ground vibration monitoring near the pipe will allow for a stronger correlation of pipe strain and ground motion to be developed.

Reduction of noise in data collection can be better achieved by better shielding data collection lines, providing power from a utility rather than from a portable generator or improving generator grounding. Studying the noise in the data that is present in the pipeline from cathodic protection and other induced currents such as paralleling overhead high voltage will aid in higher quality field data and will further allow more refined signal processing. Finally, filtering the data to reduce the noise is necessary and determine what frequency ranges are appropriate to filter will allow more effective analysis of the actual strain in the pipe.

Stresses calculated from directly measured strains in the studies were low compared to the specified maximum yield stress of the pipes. No reported damage occurred to the pipelines in the studies. As a result, the studies indicate that blasting can be effectively performed in relatively close proximity to and at relatively low scaled distance to pipelines without damage provided blasting is not conducted within the crater zone.

REFERENCES

- Daidsavor, T.A. & Provost, D.A. 2020. Direct stress monitoring of pipelines and development of limitations – A Case Study. *Proceedings 46th Annual Conference on Explosives and Blasting Technique*, Denver, CO.
- Dowding, C.H. 2008. Micrometer crack response to vibration and weather. *International Society of Explosives Engineers*, Cleveland, OH, 409 pgs.

Dowding, C.H. & Akkaya, U.G. 2013. Importance of ground strain in predicting blast-induced strain and stress in pipelines. *Proceedings: RocDyn1 EFPL Lausanne*, June.

Nymon, D.J., Dowding, C.H. & Oriard, L.L. 2008. Evaluation of close-in blasting effects on welded steel pipelines. *Proceedings 7th International Pipeline Conference*, Calgary, Alberta, Canada.

Building damage due to vibration from rock blasting – instrumented test in Norway

K.M. Norén-Cosgriff & C. Madshus

Norwegian Geotechnical Institute, NGI, P.O. Box 3930 Ullevål Stadion, N-0806, Oslo, Norway

N. Ramstad

Multiconsult, P.O. Box 265 Skøyen, N-0213, Oslo, Norway

ABSTRACT: Building damage from blast vibrations is seldom observed in Norway. This may indicate that the limit values are unnecessarily strict. In this study, two instrumented blast tests were performed in a rock quarry. Two buildings made of Light Expanded Clay Aggregate (Leca) blocks, and one in cast-in-place unreinforced concrete were erected. Two buildings were founded on rock and one on top of an about 4 m thick filling. The test buildings were instrumented with geophones and strain sensors in multiple positions. The blast tests were designed to give increasing vibration values starting at low values and ending at vibration values more than five times the limit values according to the Norwegian standard. Despite this, no visible damage was detected. The results indicate that today's limit values in Norway include a large safety margin for buildings on rock as well as on compacted stiff soil, when considering damage to outer walls.

1 INTRODUCTION

Construction activities such as blasting, piling, compaction, excavation, and construction traffic can produce vibrations of enough strength to cause damage to neighbouring buildings and structures. Limit values for vibration from construction work are given in Norwegian Standards. However, building damage assumed to originate from vibrations is seldom observed. This may indicate that today's limit values are unnecessarily strict. The determination of true limit values is very important since they restrict the efficiency of the blasting process, and hence, strict limit values can delay the progress and increase the costs. Little new research has been done, and there is particularly a lack of information about which role the frequency of the vibration plays.

For this reason, two instrumented blast tests were performed in Spulsåsen rock quarry in Våler municipality in Hedmark, Norway, in November 2018 and November 2020.

2 VIBRATION GUIDELINE LIMIT VALUES IN NORWAY

The Norwegian Standard NS 8141:2001 gives guideline limits for vibration from ground work. These are values that buildings are supposed to withstand through repeated exposures and are intended to prevent damage. The effect of the vibration frequency is indirectly considered by the fact that the limit value depends on the distance, ground conditions and foundation method, in addition to the properties of the structure and vibration source. For residential buildings the

guideline limit values for vibrations measured at foundation level in vertical direction may vary from a PPV of about 3 mm/s to about 80 mm/s.

3 DESCRIPTION OF TEST SITE AND BUILDINGS

In the first blast test, two test buildings were erected at the site, one in cast-in-place concrete and one made of lightweight construction blocks. Both were founded on an approximately 500 mm levelled and compacted layer of gravel, over rock. The dimensions of both buildings were 5 x 2 x 2.4 (l x w x h) metres. The buildings had one door opening and one window opening each.

The concrete building had 200 mm thick concrete walls without reinforcement, on top of a 400 mm wide wall footing of reinforced concrete. The walls and footing were cast-in-place with C30 grade concrete. The concrete was allowed to cure for 30 days before the blast experiments were performed. The lightweight construction block building was constructed from 250 mm Leca blocks (lightweight expanded clay aggregate) with plastered outer surfaces. This building was founded on top of a wall footing made from 330 mm wide Leca foundation blocks with reinforcement. Reinforcement was also used above the door and window opening.

In the second blast test, one building made of lightweight construction blocks (Leca) was constructed on top of an approximately 4 m thick filling, established at the same location as the buildings in the first test series. The test building had one door opening and two window openings, and the dimensions were 7 x 3 x 2.4 (l x w x h) metres. The fill was constructed of material from the quarry with properties considered approximately as moraines. The fill was established in layers with careful compaction between each layer.

At the top of all building, joists were laid and filled with crushed rock to simulate the mass and ground pressure from a typical detached house on top of a basement.

The calculated guideline limit values calculated according to NS 8141:2001 were 50 mm/s for the buildings on rock and 16-23 mm/s for the building on filling. The buildings were visually inspected between each blast round to detect and document any damage. In addition, the results from the strain measurements were reviewed correspondingly to detect any changes not visible to the naked eye. Figure 1 shows two views of the test buildings and the test area.

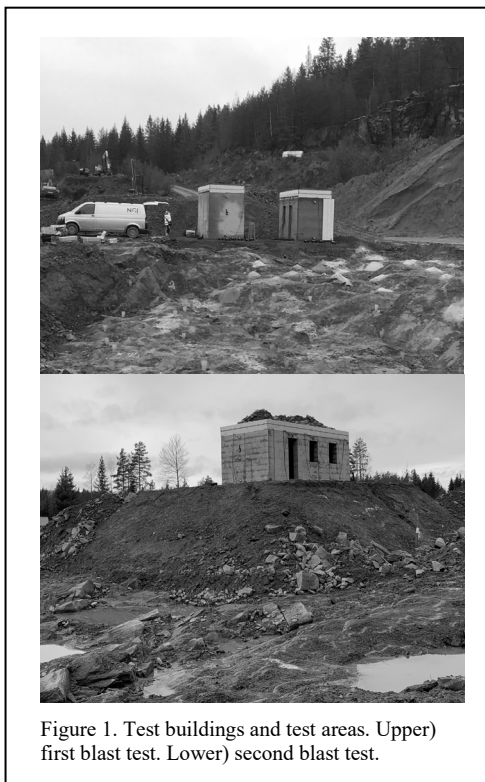


Figure 1. Test buildings and test areas. Upper) first blast test. Lower) second blast test.

Before the first blast test a geological survey of the test site was performed by use of Lidar and Orthophoto from drones. The geological survey showed fine to medium-grained red granitic gneiss containing lenses of amphibolite. The dominating direction of foliations is from the blasting area towards the buildings. In addition, the location of the buildings, sensors and boreholes were determined by GPS surveying.

3.1 Instrumentation

In the first blast test, eight three-axial velocity sensors (geophones) and eight strain sensors were mounted on each of the two buildings. In addition, vertical vibration in three positions on ground and air blast pressure in two positions were measured.

In the second blast test, 13 three-axial velocity sensors (geophones), 16 strain sensors and one microphone for air blast pressure were mounted on the walls of the test building. In addition, two three-axial geophones were mounted on top of the filling, two three-axial geophones were mounted on rock behind the filling and one vertical geophone was mounted on rock under the filling.

For the geophones and air blast microphone the AVATrace M80 measurement system was used with a 6000 Hz sampling frequency. Each three-axial sensor was connected to its own autonomous four channel logger. The fourth channel of each logger was used as a joint trigger channel. One vertical geophone in front of each building were used as trigger geophones, ensuring that all measurement channels on each building were mutually synchronised.

The strain measurements were performed with a fibre-optic measurement system from Micron Optics, using os3510 Fiber Bragg Grating Sensors (FBGS). The strain sensors were attached via rigid brackets bolted to the structures. The strain sensors were mounted on the walls in a 45° angle on intact walls, above door openings and above and below window openings. Dynamic strains were measured over a gauge length of 110 mm. The sampling frequency of the strain measurement system was 1000 Hz. This was considered enough since the frequency content of blast vibration usually are well below 500 Hz. This was also later confirmed.

4 EXECUTION OF BLAST TESTS

The blasts were designed to give increased vibration strength, starting at a low value for the longest distance and increasing progressively as the blasts came closer to the test structures.

To gain full control, repeatability and traceability of the blasts, packaged emulsion and NG-based explosives together with electronic detonators were used. The distance between the rows (burden) was about 2.0 m, and the spacing between each hole was about 2.5 m. The maximum borehole depth in each round was between 4.5 – 7 m. A 1.0 - 1.5 m crushed stone stemming was used in all holes.

In the first blast test, five blasts rounds were fired consisting of all together 143 charged holes. The number of holes detonated in one blast round varied from two single holes up to 53 holes. The

first four rounds were all shot by single hole initiation, with a delay between each hole in a row of 10 ms, while round five was shot by two and two holes simultaneously starting in the centre of the rows. The delay between the rows varied from 10 ms to 60 ms. The total amount of explosives detonated in one blast round varied from 6.5 to 404 kg, and the explosives detonated per delay varied from 3.0 to 37.8 kg. The blasts were designed to give equal dynamic loading on each of the two test structures. The first blasting round had a minimum distance of 29 m from the test structures, while the last had a minimum distance of 7 m.

In the second blast test, four blasts rounds were fired consisting of all together 220 charged holes. The number of holes detonated in one blast round varied from three to 98 holes. The first round consisted of three single constricted charges, which were shot with three seconds in between. The second and third blast rounds were shot by single hole initiation, with a delay between each hole in a row of 5-10 ms in blast round two, and 2-10 ms in blast round three. In the fourth blast round the last row was shot by three and three holes simultaneously, while the delay between the holes in the other rows was 2-5 ms. The total amount of explosives detonated in one blast round varied from 12 to 1485 kg, and the explosives detonated per delay varied from 2.0 to 47.8 kg. The first blasting round had a minimum distance of 36 m from the test building, while the last blast round had a minimum distance of 9 m.

5 TEST RESULTS

Table 1 and Table 2 show measured PPV, peak air blast pressure and peak strain during the first and second blast tests.

5.1 *Vibration frequency*

There are several methods to determine the frequency content of a signal. In this study we

Table 1. Measured maximum PPV, strain and air pressure on wall from blast test 1.

Blast round	Leca building			Air Pressure (Pa)	Concrete building		
	Scaled distance (m/kg ^{0.5})	PPV (mm/s)	Strain (□strain)		Scaled distance (m/kg ^{0.5})	PPV (mm/s)	Strain (□strain)
1	11.5	32	75	234	11.2	22	17
2	14.5	52	72	0.8	12.9	30	15
3	5.4	89	159	339	5.7	53	24
4	3.2	133	334	425	3.3	101	40
5	1	>260	733	750	1.1	>260	>1750

Table 2. Measured maximum PPV, strain and air pressure on wall from blast test 2.

Blast round	Scaled distance (m/kg ^{0.5})	PPV (mm/s)	Strain (□strain)	Air Pressure (Pa)
1	14.4	23	-	-
2	8.8	23	34	-
3	4.5	51	87	-
4	1.3	180	>3200	437

have determined the zero-crossing frequencies around each peak in the time series. The zero-crossing frequencies are determined by assuming that the time between the zero-crossing before a peak and the zero-crossing after a peak corresponds to half a period of the dominant frequency.

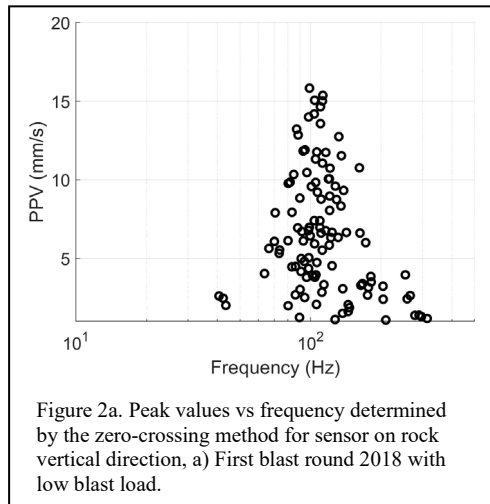


Figure 2a. Peak values vs frequency determined by the zero-crossing method for sensor on rock vertical direction, a) First blast round 2018 with low blast load.

Figure 2 shows show the zero-crossing frequencies for the sensors on rock in the first blast round in 2018, with low blast load, and in the last blast round in 2020, with high blast load. For the low blast load, the difference in zero-crossing frequencies between the vibration cycles is small. However, for the high blast load the zero-crossing frequencies differ considerably between the vibration cycles. In these circumstances, the use of a single frequency value gives a poor description of the frequency content. This indicates that if frequency dependent limit values are used, such as in the British Standard (BS 7385-2:1993) and U.S. Code of Federal Regulations, all frequencies with corresponding amplitudes from the blast need to be determined and compared to the limit value curve, and not just the frequency of the maximum

cycle, as many instruments provide as the only output.

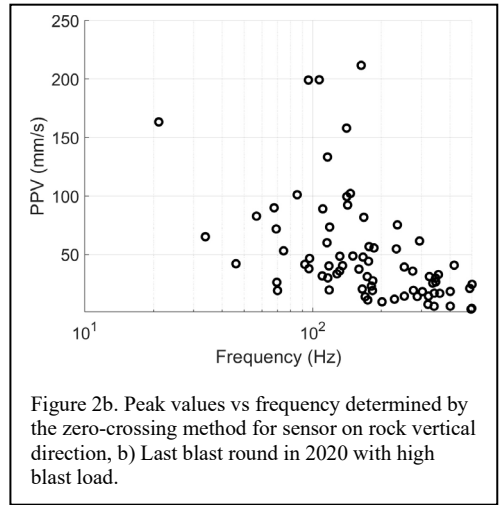


Figure 2b. Peak values vs frequency determined by the zero-crossing method for sensor on rock vertical direction, b) Last blast round in 2020 with high blast load.

Table 3 shows the zero-crossing frequencies around the maximum peak determined for the sensors on rock for all blast rounds.

Table 3. Zero crossing frequency around maximum cycle for measurements in vertical direction on rock.

Blast test	Blast round	Hor dist (m)	Frequency (Hz)
1-2018	1	35	100
	2.1	33	65
	2.2	30	81
	3	23	26
	4	18	41
2-2020	5	14	21
	1.1	52	64
	1.2	46	93
	1.3	40	72
	2	37	213
	3	22	144
	4	12	163

The results in Table 3 indicates a reduction of the dominant frequency with decreasing distance. This is not in accordance with the assumptions behind the distance factor in the Norwegian Standard and elsewhere reported in literature. However, the blast tests were designed to produce increasing vibration values, which was achieved by both increasing the charge weights and

reducing the distance for each blast round. To obtain a clearer picture of the effect of distance and charge weight, frequency and distance can be scaled with the charge weight as described in Ambraseys (1968) and Westine (1991), using the following equations:

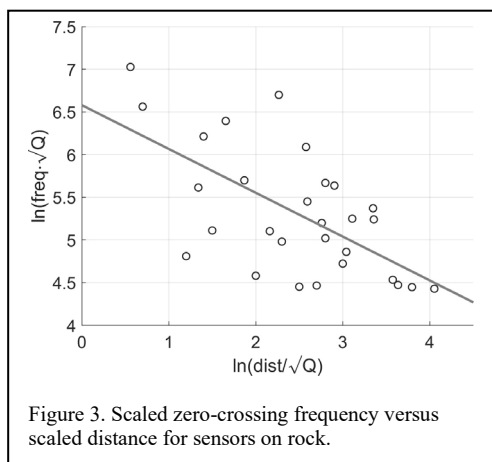
$$d_{sc} = \frac{d}{\sqrt{Q}} \quad (1)$$

$$f_{sc} = f\sqrt{Q} \quad (2)$$

Where:

- d_{sc} = scaled distance (m/kg^{0.5})
- f_{sc} = scaled frequency (Hz·kg^{0.5})
- d = distance (m)
- f = frequency (Hz)
- Q = maximum charge/delay (kg)

In Figure 3 scaled zero-crossing frequency around maximum peak is plotted against scaled distance for the sensors on rock for all blast rounds. A clear tendency towards reduced scaled frequency with increased scaled distance can be seen. This agrees with what is reported in Liu (2019).



6 CONCLUSIONS

These field blast experiments have contributed to increased understanding of vibration generation and propagation from bench blasting in rock, response of buildings to ground vibration and vibration damage mechanisms for concrete and light weight aggregate masonry buildings. Two extensive sets of high-quality synchronised vibration and strain measurement data are made

available, from well controlled, well documented rock blast rounds.

The first blast tests produced vibration values above PPV = 260 mm/s and the second blast tests a maximum PPV = 180 mm/s. These results are well above the vibration limit values calculated according to today's Norwegian Standard, which are 50 mm/s for the test buildings on rock in the first blast test and 16-23 mm/s for the test building on filling in the second blast test. The maximum measured strain levels were > 1750 μ strain in the first blast test and > 3200 μ strain in the second blast test. This is above critical strain levels reported in earlier studies. Despite this, no visible damage could be detected either on the walls or on tiles in any of the test buildings.

The zero-crossing method results reveal a large spread in the frequency between the different vibration cycles. This points to the difficulty of using frequency dependent vibration limit values.

The results of the two blast tests indicate that limit values according to the current Norwegian Standard includes a large safety margin for buildings on rock and well compacted stiff soil, when considering damages to outer walls, which this study was designed to investigate.

7 ACKNOWLEDGEMENTS

This study was performed with support from the research project Remedy (Risk Reduction of Groundwork Damage), funded by the Research Council of Norway, Grant Agreement 267674. The field test was financed by NPRA Directorate of Public Roads (Statens vegvesen Vegdirektoratet), National Railroad Authority (Bane NOR), Norwegian Association of Heavy Equipment Contractors (MEF), The Norwegian Defence Estates Agency (Forsvarsbygg) and Norwegian Contractors Association (EBA). Their support is highly appreciated. The field tests were conducted in cooperation with the upper secondary school Solør VGS. We would like to thank the responsible teacher, Øystein Johansen, and the students for excellent cooperation.

REFERENCES

- Ambraseys, N. & Hendron, A. 1968. Dynamic behaviour of rock masses. In K. Stagg, & O. Zienkiewicz, *Rock mechanics in engineering practice* (pp. 203-236). London: John Wiley & Sons.
- BS 7385-2:1993 Evaluation and measurement for vibration in buildings – Part 2: Guide to damage levels from ground-borne vibration.

- Liu, D., Lu, W., Liu, Y., Chen, M., Yan, P. & Sun P. 2019. Analysis of the main factors influencing the dominant frequency of blast vibration. *Hindawi shock and vibration, Article ID 8480905*.
- NS 8141:2001 Vibration and shock. Measurement of vibration velocity and calculation of guideline limit values in order to avoid damage on constructions. (In Norwegian).
- U.S. Code of Federal Regulations (CFR) 30 §715.19, §816.67 and §817.67.
- Westine, P.S., Dodge, F.T. & Baker W.E. 1991. Similarity methods in engineering dynamics – theory and practice in scale modelling – revised edition. Elsevir.

Effects on buildings from blast induced vibrations – a numerical pre-study

P.D. Folkow, M. Johansson, J. Leppänen, G. Edefors & A. Naseri

Chalmers University of Technology, Göteborg, Sweden

ABSTRACT: It is well known that blasting in rock may cause structural damage to nearby buildings. There are differences among most countries regarding legislation with respect to blast induced vibrations. Criticism has been raised against this unclear situation, and it is of importance to develop more reliable predictions on ground and structural vibrations. The present work has its origin based on the features within the Swedish Standard. These guidelines are related to distance and underground conditions, contrary to many other national standards which are based on frequency measures. There is a desire to update the Swedish Standard; either based on distance, frequency or some other measures. This pre-study considers numerical studies (2D FEM) for modelling blasting effects. The aim is to illustrate how various parameters (material, geometry, load) influence ground vibration phenomena as well as structural effects above-ground.

1 BACKGROUND

Blasting causes ground vibrations that may cause damages to nearby buildings and other structures. The Swedish Standard – Vibration and Shock (SIS 2011) used for ground borne vibrations states guidelines which are based on empirical data from the 1960s and depends on parameters such as distance and ground conditions. The scientific support for the guidelines may be considered weak, and criticism has been raised of its validity. In the Swedish standard, the permitted vibrations are limited only to the vertical velocity component of the ground surface. Further, in most other countries guidelines are used that are conceptually different than in Sweden, and these guidelines are based on frequency measures from the blast induced vibration (Gjödvard & Jern 2019, NGI Remedy 2019). The various national guidelines have their shortcomings and are mainly based on rules of thumb with a lack of scientific basis.

There is a desire in the industry to modernise the standard by better understanding the theoretical background of how different vibration parameters affect the damage in a building. It is considered poorly known how and when damage occurs, and more detailed studies based on numerical modeling have been particularly highlighted (Dowding 2000, Norén-Cosgriff *et al.* 2020).

The aim of this work was to study how different phenomena affect the ground vibrations and the risk of damage to buildings. Two different models were used, one for the load response and one for the structural response.

In the first model, blast induced vibrations at the ground surface were studied without any presence of buildings. The following parameters were investigated:

- Blasting parameters (distance to charge, angle of incidence)
- Ground conditions (stiffness, density, geometry)

In the second model, the structural response of a concrete wall with openings was studied using a prescribed vertical movement of the ground surface below the wall sole. The wall geometry was fixed but the ground stiffness was varied to simulate various ground conditions. Further, the prescribed vertical vibrations were applied in the ground using combinations of various load frequency and ground wave speed.

The work presented here is a summary of a numerical pre study (Folkow *et al.* 2021), and a series of subsequent works are planned to obtain a deeper physical understanding on the effect on buildings from blast induced vibrations. The long-term aim is to contribute knowledge to revise the current Swedish standard.

2 WAVE PROPAGATION PHENOMENA

In this study, blast induced vibrations were studied by numerical analyses using two dimensional (2D) linear finite element (FE) analyses, both in time and frequency domain. First, the blast induced vibrations, both in horizontal and vertical directions, were studied by varying the load (amplitude, frequency content, duration, distance to charge and angle of incidence). Furthermore, the wave propagation phenomena (wave speed, damping, frequency content) were studied and interaction between the ground materials rock and clay, by varying the layer thickness of the clay above rock, and the boundary effects at the ground surface (reflection, change of wave type, displacement field). Thereafter, the structural response was studied by using a prescribed vibration with a given frequency.

In the model used for studying the load response, the effects in the near field from the blast were not included. Only the far field wave propagation was studied by assuming a symmetrical pressure wave, which propagated in a radial direction from the blast, resulting in a linear wave propagation with a pressure wave (P-wave) propagating in radial direction, which may transform to a Shear wave (S-wave), for instance at the interface between the rock and the clay. The P-wave propagates faster than the S-wave, and in an isotropic material the wave propagation velocities can be determined as:

$$c_p = \sqrt{\frac{E(1-\nu)}{\rho(1+\nu)(1-2\nu)}} \quad (1)$$

$$c_s = \sqrt{\frac{E}{\rho \cdot 2(1+\nu)}} \quad (2)$$

where ρ is the density, E is the modulus of elasticity and ν is the Poisson's ratio. The ground wave speed c does not depend on the frequency content of the wave, and the relationship between the wavelength λ and the frequency f can be determined as:

$$\lambda = \frac{c}{f} \quad (3)$$

At the ground surface, in addition to wave transformation at interfaces, various forms of surface waves will be created, and the most dominant surface wave is the Rayleigh wave (R-wave), which propagates slower than the S-wave, and its speed is commonly approximated as:

$$c_R = \frac{0.862 + 1.14 \cdot \nu}{1 + \nu} \cdot c_s \quad (4)$$

However, the R-wave has much lower damping than both the P- and S-waves, and in addition to the vertical component in the displacement field, a significant component in the horizontal direction is created, which is approximately 50% of the vertical component.

3 LOAD RESPONSE

3.1 Geometry, material and load

Numerical calculations have been performed using the general finite element programme COMSOL Multiphysics® (COMSOL 2019) using two-dimensional (2D) plain strain models assuming linear elastic response. The use of 2D models for these studies is a simplification of reality, and in a conceptual pre-study as this, it is deemed to be good balance between accuracy and 'cost' regarding calculation time. The ground vibration obtained are a direct effect of the applied load and the purpose of the analyses performed has never been to fully seek to imitate an actual blasting sequence in rock. Hence, it is also not of interest to focus on individual vibration values in the presented results; instead, focus should be on how the resulting vibrations conceptually vary with changed parameters.

The geometry, boundary conditions and application of blasting are shown in Figure 1.

The material parameters for rock and clay are listed in Table 1 and the blast load properties are shown in Figure 2.

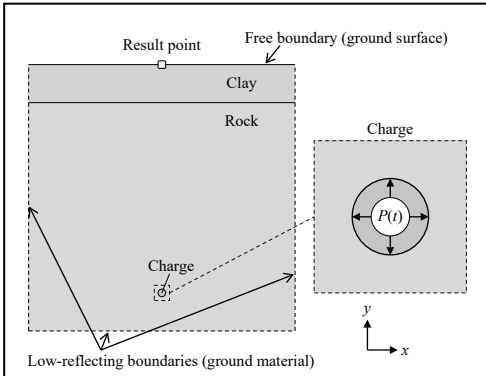


Figure 1. Geometry and boundary conditions of FE model. The blast load was applied as a pressure $P(t)$ located inside a circle (diameter 32 mm) according to the enhanced picture.

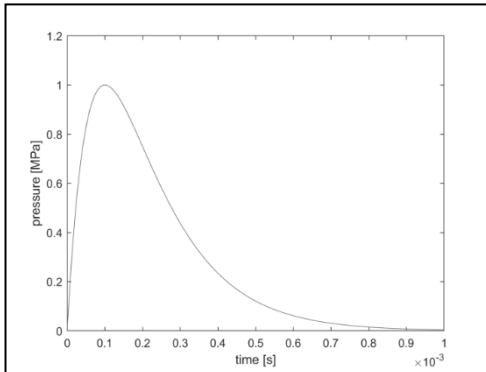


Figure 2a. Blast load properties: (a) pressure-time relation $P(t)$.

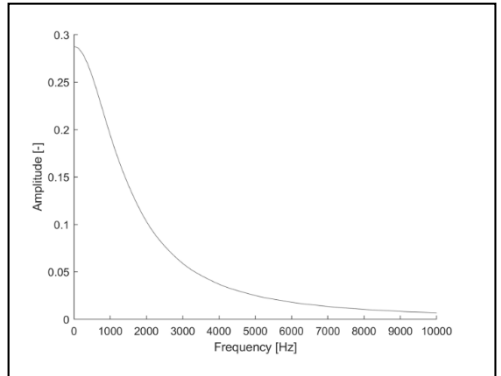


Figure 2b. Blast load properties: (b) frequency content.

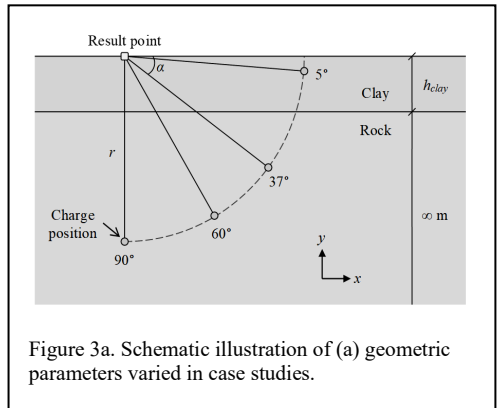


Figure 3a. Schematic illustration of (a) geometric parameters varied in case studies.

Table 1. Material properties for rock and clay, wave speeds are rounded values based on properties used.

Type	E	ν	ρ	c_P	c_S	c_R
	[GPa]	[-]	[kg/m ³]	[m/s]	[m/s]	[m/s]
Rock	60	0.25	2,600	5,300	3,000	2,800
Clay	0.050	0.495	1,700	1,000	100	95

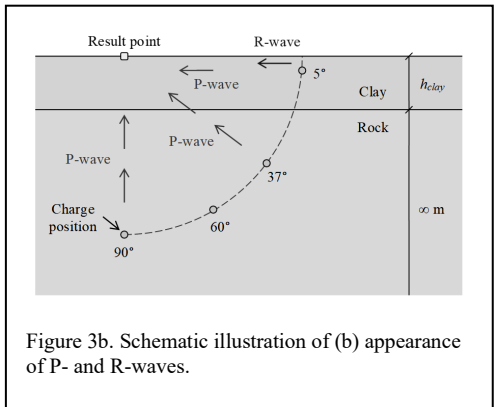


Figure 3b. Schematic illustration of (b) appearance of P- and R-waves.

Several case studies were made varying the geometric parameters schematically shown in Figure 3a:

- Distance to charge: $r = [30, 50, 100]$ m
- Angle of incidence: $\alpha = [5, 37, 60, 90]$
- Thickness of clay layer: $h_{clay} = [0, 2.5, 5, 10]$ m

3.2 Results

In the case studies, the resulting vibrations in the horizontal (x) and vertical (y) directions were determined. Special focus was put on the appearance of P- and R-waves, as schematically

illustrated in Figure 3b. Here, the P-wave propagates from the centre of explosion at a speed higher than that of the R-wave. Therefore, the P-wave, regardless of charging location, always reach the result point first. However, when the P-wave reaches the free ground surface, S-waves are also generated as a boundary effect and for a charge located near the surface, interaction between P- and S-waves will give rise to R-waves that propagate along the surface.

Figure 4 shows examples of the vibration $v_x(t)$ and $v_y(t)$ in the horizontal and vertical direction, respectively, at various angles of incidence α ; here for a distance $r = 50$ m. The peak obtained at time $t \approx 0.009$ s is caused by the P-wave when it reaches the result point. However, for $\alpha = 5$, a secondary peak is also obtained at $t \approx 0.018$ s, i.e. a time which coincides well with the theoretical value for the arrival of an R-wave and hence it is also deemed to be caused by such a wave. However, no corresponding peak for the R-wave can be observed when $\alpha = 37-90$.

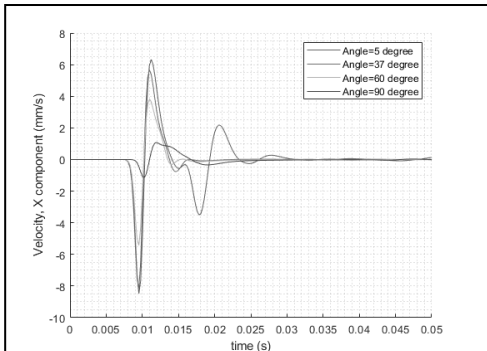


Figure 4a. Examples of vibration-time relationships in (a) horizontal direction $v_x(t)$ for distance $r = 50$ m and varying angle of incidence α . Theoretical arrival times for P- and R-waves are approximately 9.4 ms and 17.9 ms, respectively.

In Figure 5 the maximum velocity amplitude in the horizontal (x) and vertical (y) directions are compared for various distances r and angle of incidence α when $h_{clay} = 0$ m. The results are distinguished of whether being caused by a P- or R-wave, where the latter is assumed to cause the vibrations at times larger than the theoretical arrival time of an R-wave. From this comparison it can be noted that an increased angle of incidence means that horizontal vibrations v_x decrease while vertical vibrations v_y increase. Further, for the horizontal vibrations it can be noted that similar values are obtained for each distance r when $\alpha =$

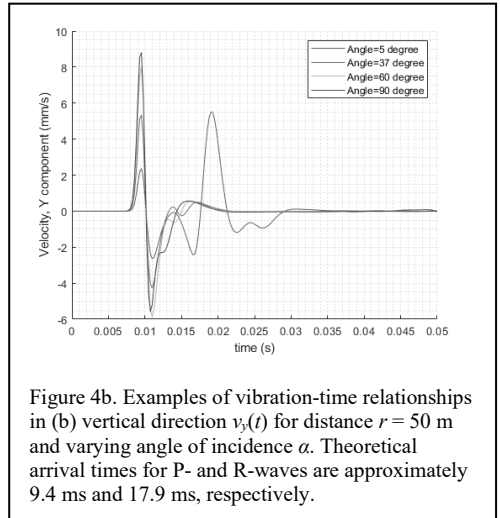


Figure 4b. Examples of vibration-time relationships in (b) vertical direction $v_y(t)$ for distance $r = 50$ m and varying angle of incidence α . Theoretical arrival times for P- and R-waves are approximately 9.4 ms and 17.9 ms, respectively.

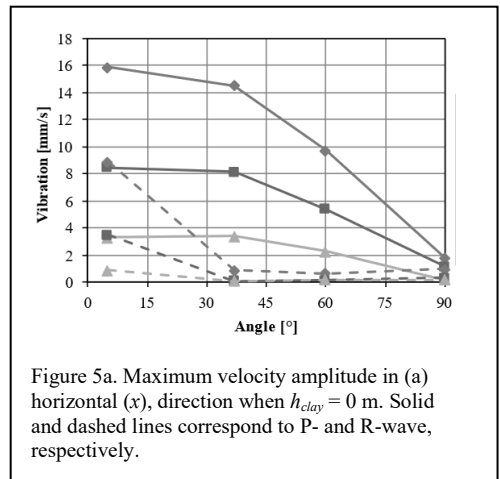


Figure 5a. Maximum velocity amplitude in (a) horizontal (x), direction when $h_{clay} = 0$ m. Solid and dashed lines correspond to P- and R-wave, respectively.

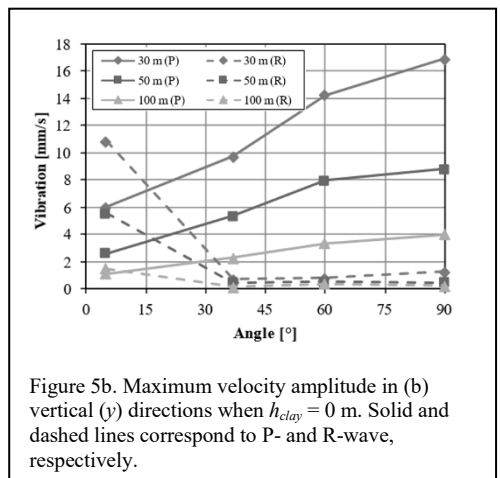


Figure 5b. Maximum velocity amplitude in (b) vertical (y) directions when $h_{clay} = 0$ m. Solid and dashed lines correspond to P- and R-wave, respectively.

5-37, and for the vertical vibrations the same observation can be made when $\alpha=60-90$. It is also worth noting that the horizontal and vertical vibrations are of similar magnitudes when $\alpha = 37-60$, i.e. there must be a rather flack or steep angle of incidence to obtain a significant difference in amplitude of horizontal and vertical vibrations.

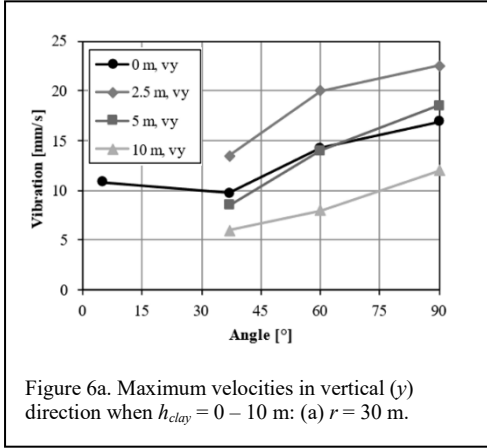


Figure 6a. Maximum velocities in vertical (y) direction when $h_{clay} = 0 - 10$ m: (a) $r = 30$ m.

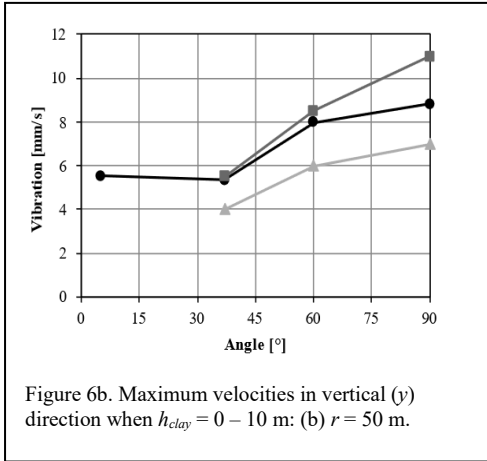


Figure 6b. Maximum velocities in vertical (y) direction when $h_{clay} = 0 - 10$ m: (b) $r = 50$ m.

Figure 6 compares the maximum velocities in the vertical (y) direction for various combinations of distance r and angle of incidence α when $h_{clay} = 0 - 10$ m. From this it can be observed that a large depth of clay ($h_{clay} = 10$ m), in most cases, leads to reduced vibrations compared to a case with no clay ($h_{clay} = 0$ m); i.e. the clay has a dampening effect on the vibrations. However, for a small depth of clay ($h_{clay} = 2.5$ m) the vibrations increase; i.e. a thin layer of clay may cause amplification effects through interference in the rock/clay layer and the free ground surface.

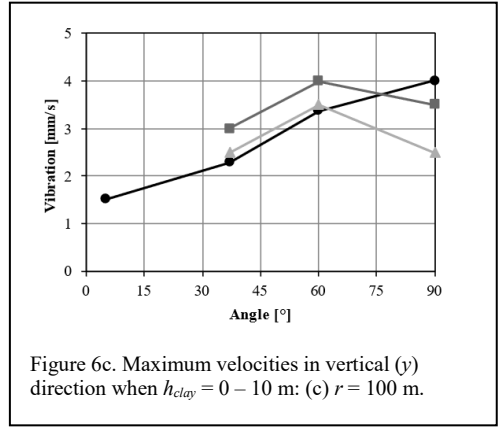


Figure 6c. Maximum velocities in vertical (y) direction when $h_{clay} = 0 - 10$ m: (c) $r = 100$ m.

4 STRUCTURAL RESPONSE

4.1 Geometry, material and load

To study the influence of vertical vibrations in the ground on the structural response, a simplified wall structure with openings was simulated using the general FE programme Abaqus/CAE (Dassault 2019). The ground vibration was simulated using a vertical movement

$$v_y(t) = v_A \cdot \sin \omega t \quad (5)$$

which came in from the left side of a wall, moving in the horizontal direction with a speed according to the ground wave speed c , see Figure 7a for a schematic illustration. The applied vibration was given a duration

$$t_{vibr} = 3 \cdot T \quad (6)$$

where T is the eigenperiod of the vibration determined as

$$T = \frac{1}{f} = \frac{2\pi}{\omega} \quad (7)$$

The time it takes the vibration to pass the building is

$$t_{wall} = \frac{l_{wall}}{c} \quad (8)$$

which means that, depending on the combination of wall length l_{wall} , wave speed c and load frequency f , it is possible that the vibration load is terminated at the front end of the wall before any vibration load has even reached its far end.

Figure 7b shows the geometry of the wall with openings that have been studied in this report. The geometry was chosen to be the same as used in blasting tests carried out in Norway (Norén-Cosgriff *et al.* 2020). In these tests, the structure was founded on an approximately 0.5 m levelled and compacted layer of gravel, over rock. The simulations were made using linear elastic, first order 2D plane stress elements (square shape, side 0.1 m) with reduced integration. To model the ground, linear 2-node springs were used which were attributed a constant stiffness to simulate various ground conditions. The top nodes of the springs were fixed to the bottom of the wall sole while the bottom nodes were velocity controlled using $v_y(t)$ according to equation (5).

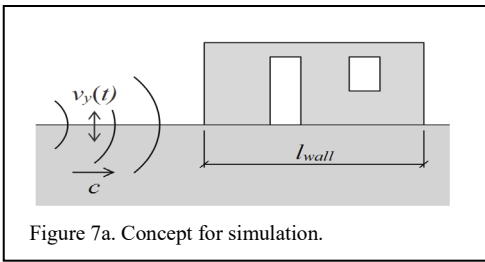


Figure 7a. Concept for simulation.

Material parameters in wall and spring stiffness:

$$E_c = 30 \text{ GPa}, \nu = 0.2, \rho_c = 2500 \text{ kg/m}^3, m_{roof}' = 240 \text{ kg/m (extra mass on top of wall)}$$

$$k = [0.04, 0.16, 1, 10] \text{ GN/m}^2$$

Load parameters:

$$v_A = 100 \text{ mm/s}$$

$$f = [25, 50, 100, 200] \text{ Hz}$$

$$c = [500, 1000, 2000, 4000] \text{ m/s}$$

A ground stiffness of $k = 0.04 \text{ GN/m}^2$ was estimated based on the conditions used in the tests made by Norén-Cosgriff *et al.* (2020). However, an increased stiffness ($k = 0.16 \text{ GN/m}^2$) was needed to reproduce the lowest eigenmode of the wall observed in the tests, see Section 4.2. The higher ground stiffnesses, $k = [1, 10] \text{ GN/m}^2$, were then included as part of the parametric study.

The purpose in this study was never to study the wall response values in detail but rather to observe trends and principles. Therefore, simplified load values were used, e.g., an amplitude $v_A = 100 \text{ mm/s}$ and to restrict $v_y(t)$ to just include a single frequency. Further, the ground wave speed was chosen to approximately represent that of both P- and R-wave for various type of ground conditions.

4.2 Results

Figure 8 shows the first four eigenmodes and corresponding eigenfrequencies for the wall structure for all cases studied.

The first eigenfrequency for the wall in Norén-Cosgriff *et al.* (2020) was observed to be $f_1 \approx 26 \text{ Hz}$; i.e. approximately corresponding to a ground stiffness of $k = 0.16 \text{ GN/m}^2$ in the analyses, compare with Figure 8b in which $f_1 \approx$

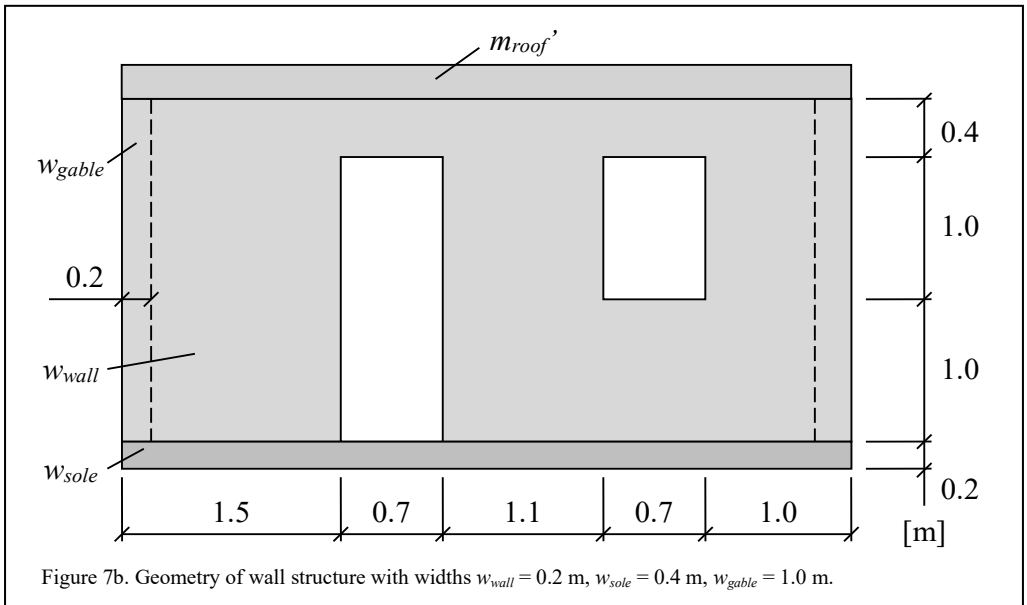
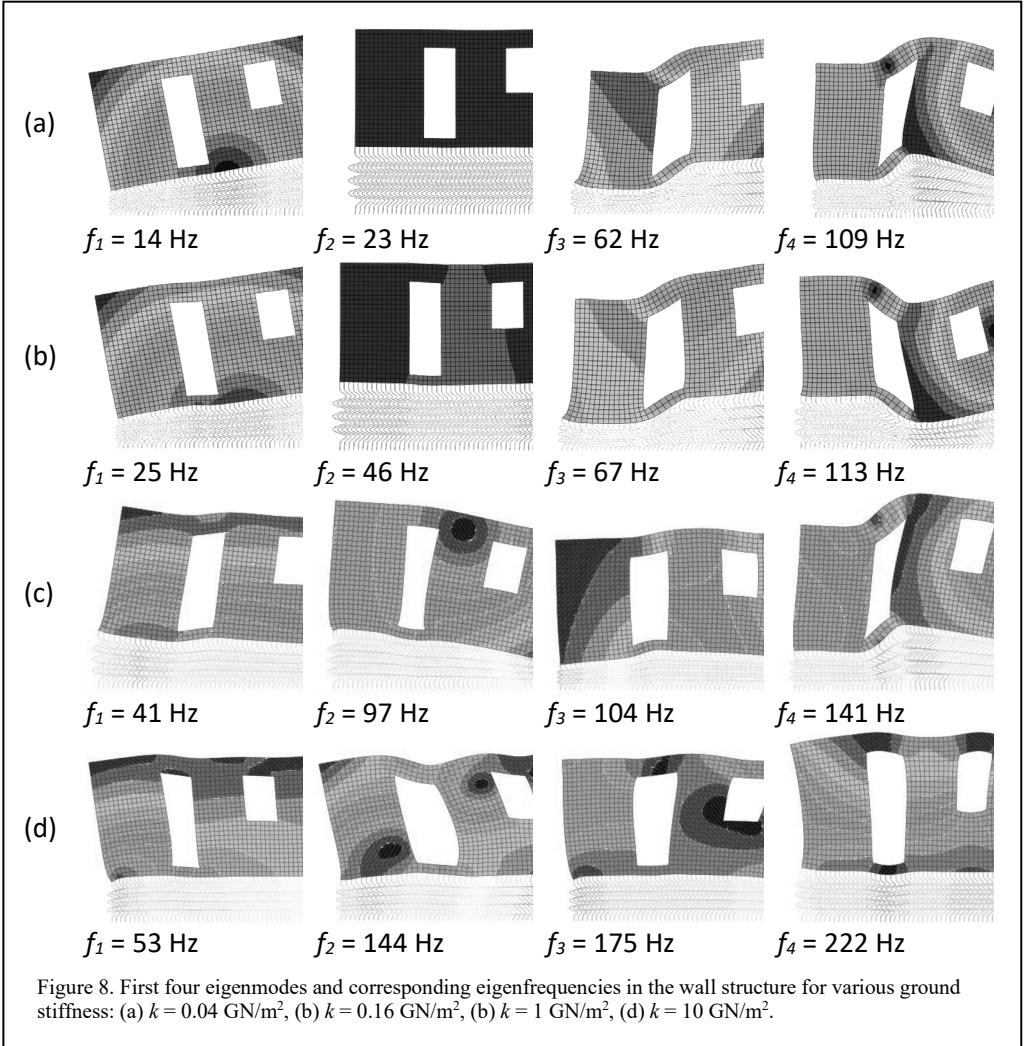


Figure 7b. Geometry of wall structure with widths $w_{wall} = 0.2 \text{ m}$, $w_{sole} = 0.4 \text{ m}$, $w_{gable} = 1.0 \text{ m}$.



25 Hz. When $k = [0.04, 0.16] \text{ GN/m}^2$ the first two eigenmodes are dominated by the low ground stiffness and approximately correspond to rigid body motions of the wall structure. However, for all other combinations the eigenmodes are clearly affected by the wall stiffness.

Figure 9 shows some examples of the maximum tensile stresses obtained in the wall structure due to various combinations of vibration load and ground stiffness and from this it is indicated that the critical stress stage may be obtained at various load frequencies, depending on e.g., the ground stiffness. Further analyses were made in which the wave speed c and ground stiffness k were varied for load frequencies $f = [25, 50, 100, 200] \text{ Hz}$. The resulting maximum tensile

stresses from those analyses are summarized in Table 2 and from this it can be concluded that there is no clear trend of which load frequency or ground wave speed that produce the most critical tensile stresses in the wall structure. The structural response of the wall is also affected by its eigenfrequencies but comparing the frequencies of the first eigenmodes shown in Figure 8 with the critical load frequencies in Table 2 does not explain the combinations of f , c and k found critical.

To further investigate this, the maximum tensile stresses obtained in the corner regions of the wall's two openings have been studied, see Figure 10 for location and denotation. Based on the plots in Figure 9, this is where the maximum

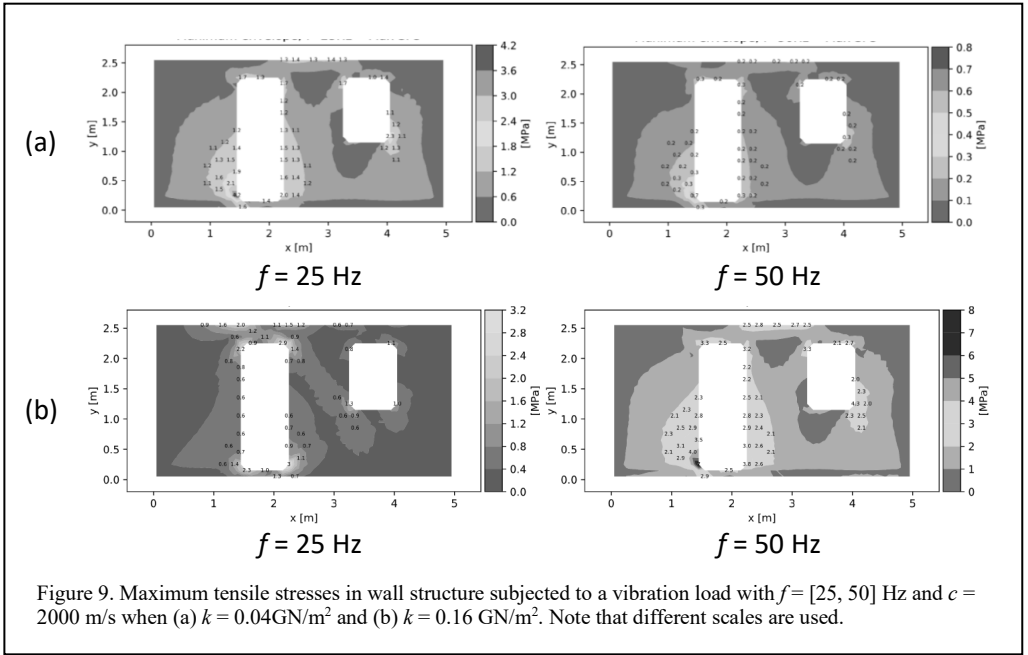


Figure 9. Maximum tensile stresses in wall structure subjected to a vibration load with $f = [25, 50]$ Hz and $c = 2000$ m/s when (a) $k = 0.04$ GN/m² and (b) $k = 0.16$ GN/m². Note that different scales are used.

Table 2. Maximum tensile stress in the wall structure for various combinations of load frequency f , wave speed c and ground stiffness k .

k [GN/m ²]	0.04		0.16		1		10	
c [m/s]	500	2000	500	2000	500	2000	500	2000
f [Hz]	σ_{max} [MPa]							
25	-	4.2	11	3	3	1	2.5	0.5
50	-	0.7	5	7	32	12	5.5	2
100	-	0.6	6	3	10	11	10	10
200	-	0.1	< 0.5	0.5	2	4.5	8.5	15

tensile stresses appear and in Figure 11 it is shown how the maximum tensile stresses varies in the eight corner regions for various f and c when $k = [1, 10]$ GN/m². Here, it can be seen that the maximum tensile stress in the corner regions does not always appear for the same combination of f and c ; when e.g., $c = 2000$ m/s and $k = 1$ GN/m², the maximum tensile stress is obtained at $f = 50$ Hz in three corner regions and at $f = 100$ Hz in five corner regions. In Figure 8 the first four mode shapes and eigenfrequencies for this case is shown: $f_i = [41, 97, 104, 141]$ Hz; i.e. two eigenfrequencies close to 100 Hz. Hence, these frequencies indicate that a load frequency of 100 Hz should be critical for the wall structure, but as can be seen in Figure 11, this is not necessarily the case.

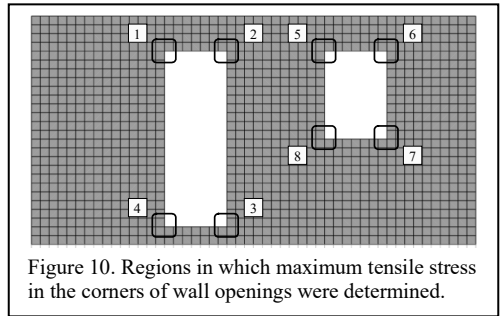


Figure 10. Regions in which maximum tensile stress in the corners of wall openings were determined.

Table 3 shows a summary of all the analyses of the wall structure in which it is shown (marked with ●) at what load frequency f the maximum tensile stress is obtained for a given combination of wave speed c and ground stiffness k . Further, in

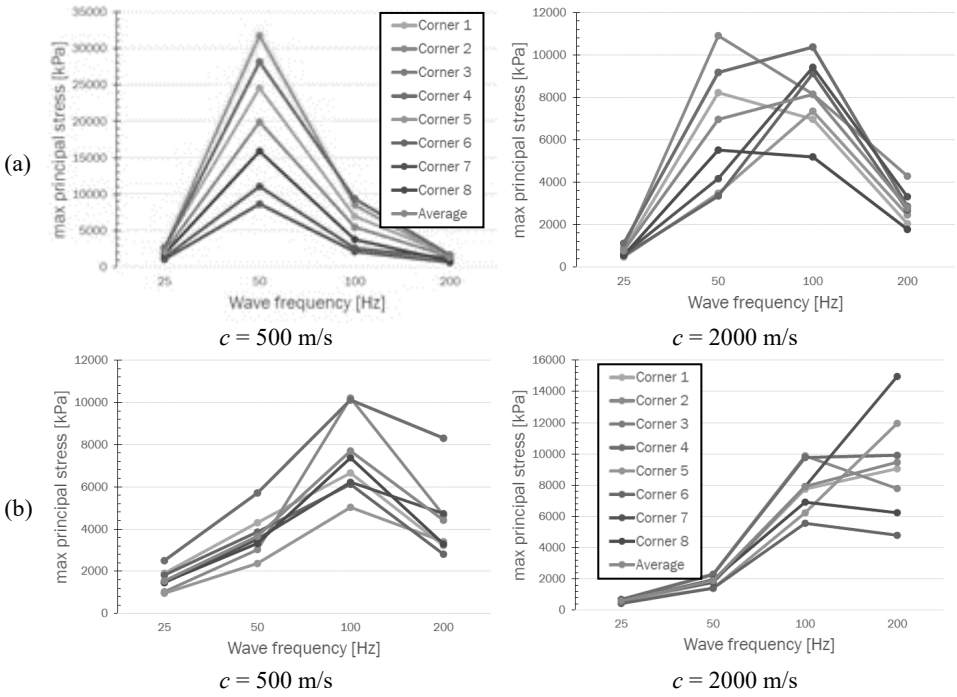


Figure 11. Maximum tensile stresses in corner 1 to 8, according to Figure 10, when the wall structure was subjected to load frequency $f = [25, 50, 100, 200]$ Hz at wave speed $c = [500, 2000]$ m/s when (a) $k = 1 \text{ GN/m}^2$ and (b) $k = 10 \text{ GN/m}^2$.

Table 3. Summary of for what combinations of load frequency f , wave speed c and ground stiffness k that maximum tensile stresses were obtained in the wall structure.

f [Hz]	$k = 0.04 \text{ GN/m}^2$		$k = 0.16 \text{ GN/m}^2$		$k = 1 \text{ GN/m}^2$		$k = 10 \text{ GN/m}^2$	
	c [m/s]		c [m/s]		c [m/s]		c [m/s]	
	500	2000	500	2000	500	2000	500	2000
25	-	•	•	-	-	-	-	-
50	-	-	-	•	•	•	-	-
100	-	-	-	-	-	○	•	-
200	-	-	-	-	-	-	-	•

- = Maximum stress in wall.
- = Maximum stress in at least one corner region according to Figure 10.
- = Not studied.

those cases when at least one corner region reaches its maximum tensile stress at another load frequency than this, this is shown as well (marked with ○). Based on this compilation it can be concluded that it is difficult to predict in advance what combination f and c will result in the most critical case for a given structure. Further, based on the maximum stresses listed in Table 2 it is also

clear that there is no clear trend of what load combination leads to the highest tensile stresses; the results obtained indicate that high stresses may be obtained for both low and high load frequencies and for low and high wave speeds. The trend observed is that the critical load frequency f increases with an increased ground stiffness k .

5 CONCLUSIONS AND FUTURE WORK

This pre-study has focused on studying wave propagation and vibration effects from blasting from both the load response and structural response perspectives. Below, the most important observations are listed:

- Load response (ground vibrations generated by blasting):
- Ground vibrations at the surface have in many cases a significant horizontal component, in addition to the vertical component that is considered in the Swedish Standard.
- The ground vibrations are largely affected by the position of the explosive charge (distance and angle of incidence).
- With looser foundations (e.g., clay on rock), the thickness of the clay layer may have a considerable effect on the ground vibrations and depend on e.g., its resonance effects.

Structural response (effects of ground vibration on a building):

- Based on studies of a simplified wall structure, it has been noted that it is complex to predict how the magnitude of the resulting stresses is affected by different parameters.
- It is not obvious in advance that a given combination of load frequency f and ground wave speed c will result in large tensile stresses.
- Varying combinations of f and c can give significant differences in stress, both up and down, without observing any clear context in the effect of various parameters. Resonance effects can only partially explain the observed scattering in results.

Future works:

- Continued studies of how the ground vibrations are affected by various ground conditions and the location of the charge.
- Parametric studies of wall structures with various geometry and ground conditions (including less stiff ground).
- Comparison of numerical simulations of wall structure with experimental results obtained from full-scale tests in Norway. Test data are available for various kind of wall structures and ground conditions.

6 ACKNOWLEDGEMENTS

The research presented in this paper was financed by Swedish Transport Administration (Trafikverket) and Rock Engineering Research Foundation (BeFo).

REFERENCES

- COMSOL 2019. *COMSOL Multiphysics®* v. 5.5, COMSOL AB, Stockholm, Sweden, 2019.
- Dassault 2019. *Abaqus/CAE*, Dassault Systèmes Simulia Corp, US, 2019.
- Dowding, C.H. 2000. *Construction vibrations*, Prentice Hall, Englewood Cliffs, NJ, 2000.
- Folkow, P., Johansson, M., Leppänen, J. 2021. Skadeverkan mot byggnad av markvibrationer från sprängning (Structural damage on buildings due to blast induced ground vibrations. In Swedish), *Chalmers University of Technology, Report ACE 2021:1, 2021.*, Göteborg, Sweden.
- Gjödvdad, J.F. & Jern, M. 2019. Vibration monitoring standards connected to the use of explosives in Europe, *EFEE 10th world conference on explosives and blasting*, Helsinki, Finland, 2019.
- NGI Remedy 2019. Vibration induced damage due to construction work – State of the art report, WP4. *Vibrations induced by construction activity” Deliverable 4.1, rev 0, NGI Remedy Project*, Norway, 2019.
- Norén-Cosgriff, K., Ramstad, N., Neby, A. & Madshus, C. 2020. Building damage due vibration from rock blasting, *Soil Dynamics and Earthquake Engineering*, 138, 2020.
- SIS 2011. Vibration and shock - Guidance levels for blasting-induced vibration in buildings, *Swedish standard SS 460 48 66*, Stockholm, Sweden, 2011.

Elevated pipeline response to shaft blasting

C.T. Aimone-Martin

Aimone-Martin Associates, LLC

J. Redyke

Dykon Blasting Corp.

B.M. Meins & O.C. Meins

Detecht, LLC

ABSTRACT: Two 9.1 m diameter shafts were excavated by blasting from elevations -24.7 to 38.4 m at nominal distance of 12 m from a 1.6 m diameter welded steel water pipeline elevated on concrete piers. Shafts will convey water through a new 1.83 m pipe via microtunnels crossing beneath the Canadian River in Oklahoma. The 60-year-old pipeline was instrumented at the support pier and at the unsupported midspan with circumferential and longitudinal strain gauges to compare with global shear and elongation strains calculated from velocity measurements. Maximum midspan lateral and vertical displacements were 0.67 and 0.55 mm producing computed global shear strains of 30.8 and 35.3 $\mu\epsilon$, respectively. The highest hoop and elongation strain measurements at the midspan pipe crown were 14.1 and 6.3 $\mu\epsilon$ when the peak ground vibration was 17 mm/s. Blast-induced pipeline deflections and resulting strains were considered to be highly safe and protective of the aged pipeline.

1 BACKGROUND

Microtunneling beneath the Canadian River Crossing was required to replace an existing elevated water supply pipeline, constructed in 1962, and add a second line to increase water supply into Oklahoma City in the U.S. from outlying reservoirs. The existing 762 mm-diameter welded ductile iron pipeline is supported on concrete piles adjacent to the river crossing. Access for the two replacement pipelines and micro tunnel boring machine (MTBM) construction required excavation of two, 10.4 m diameter shafts in close proximity to the pipeline, shown in Figure 1, to a final depth of 38.1 m. The upper 21.3 m comprised a secant pile liner within unconsolidated materials and lower 16.8 m a liner

plate through hard rock that required blasting. Additional blasting was needed to complete two launch portals for the MTBM. The construction site was within the adjacent river floodplain, requiring several meters of cobblestone fill to serve as a working platform.

Figure 2 shows details of the pipeline supporting elements, concrete pier bases, pinned connections to concrete piers and upper rings. The pipeline properties are given in Table 1. As built drawings did not identify the pipeline grade and it was assumed that the material is ductile iron with properties similar to a grade C steel available at the time of construction. Concrete pier P13 height above the ground surface is 2 m and the total height to the pipe top is 6.7 m. Blast and monitoring plans were submitted for review by the

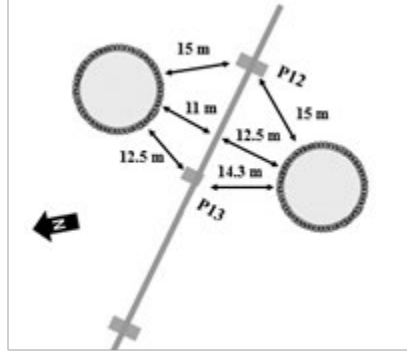


Figure 1. Aerial view of shafts on either side of the elevated pipeline after completion of secant piles (left) and distances from shaft perimeters to piers P12 and P13.

owner’s consultants. Plans included provisions to limit and monitor differential displacements and strains at critical locations within the supporting structure. Of greatest importance were vertical and lateral deflections at the unsupported pipe midspan and controlling amplification of structure motions relative to pier base excitations. Concerns arose during plan reviews that comprehensive soil structure interaction (SSI) dynamic modelling of the piers supports was not performed. The approach taken by the blast and monitoring team was to limit dynamic (blasting) midspan deflections and resulting axial and hoop strains in accordance with AWWA M11 (2017) and meet simply-supported steel pipeline guidelines by Bonds (2017). In the simplest form, the recommended allowable midspan deflection limit for pipes can be taken as 5% of the outside diameter or this case 0.16 m. This was

accomplished by controlled blasting methods and appropriate time delays.

Table 1. Ductile iron pipeline properties.

PIPE PARAMETERS	
Welded steel Grade	C
Pipe OD (m)	1.6
Wall thickness (mm)	25.4
Unsupported length between piers (m)	24.84
Total load over unsupported length (pipe+water) (Mg)	72.5
Young's modulus (GPa)	200
Tensile strength (MPa)	413.7
Minimum yield strength (MPa)	206.8
Design Factor (%)	50
Allowable Pipe wall hoop stress (design strength) (MPa)	103.4
Allowable strain ($\mu\epsilon$)	517.0

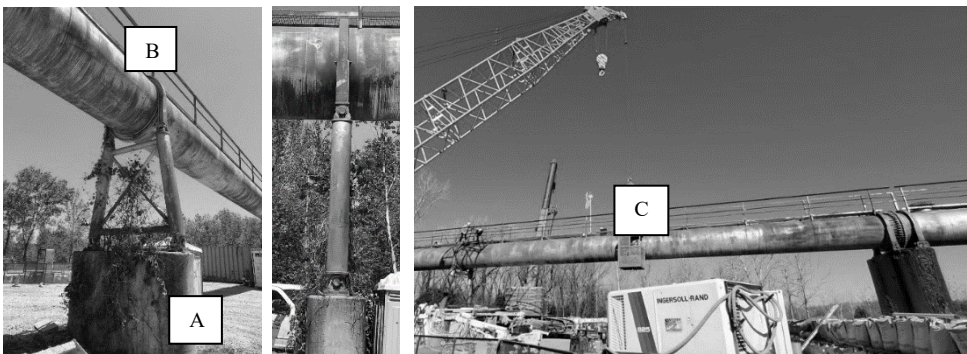


Figure 2. Concrete pier P13 supporting steel pipe bents with rocker and sliding connections and single upper support ring (left and middle) and deploying strain gauges from elevated cage at unsupported midspan (right); A through C denote locations of instrumentation.

2 BLAST DESIGN

A total of eight blasts were conducted by Dykon Blasting between December 2020 and July 2021. Holes drilled 76.2 mm in diameter were loaded with 50.8 mm by 406 mm cartridge emulsion with a cartridge density of 1.23 g/cc, 0.34 and 0.454 kg PETN boosters, det cord for tunnel round pre-split holes and electronic detonators. Charge weights per delay ranged 2.86 to 10.5 kg. Sinking shots with a centre pull utilised 8 to 22 ms delays outward with perimeter holes fired 25 ms. Drill hole spacings were 1.22 m and depths ranged 2.4 to 3.7 m with powder factors of 0.9 to 1.5 kg/m³. Tunnel rounds were designed with a burn cut, 0.9 m hole spacings, drill depths of 2.7 to 3.2 m and powder factors ranging 2.93 to 3.45 kg/m³.

3 VIBRATION AND STRAIN MONITORING

Geophones were deployed to measure ground, pipeline, and pipeline supporting structure vibrations to calculate global strains between locations identified in Figure 2 as the pipe top or crown (B) and midspan (C). Strain gauges, used to directly measure pipeline strains, were affixed to the pipeline at the pier top (B) and midspan (C) shown in Figure 3 at both the pipe crown and springline. Geophones were affixed to structures using hot glue and strapping around the pipe and the in-ground geophone was buried 0.15 m at location (A).

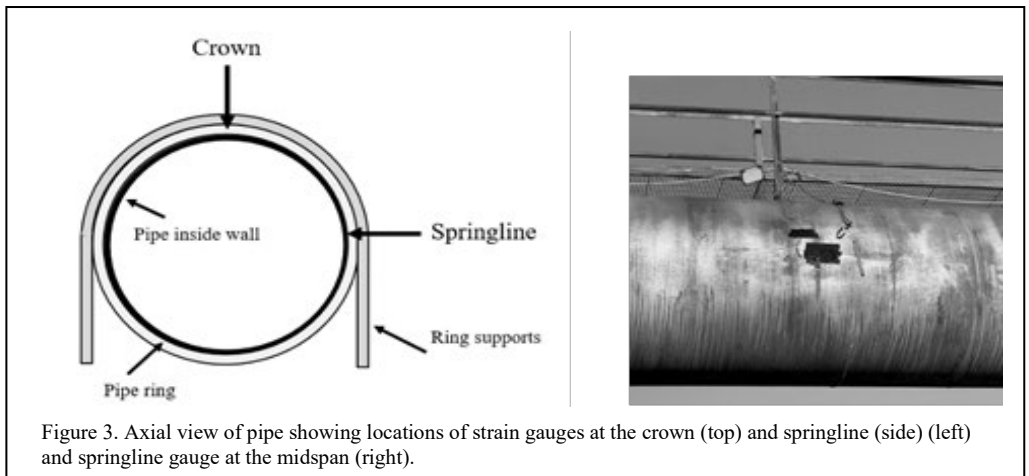
All recording systems using sample rates of either 16,384 or 4096 sec⁻¹, were co-triggered with the master seismograph at (A). In this manner, the vibratory responses of the pier and pipeline were recorded simultaneously to enable analysis of differential structure motions and calculate global

strain to compare with measured strains.

Wire strain gauges were affixed to the pipeline above P13 and at the midspan at the springline and crown to record longitudinal and hoop strains in the pipeline wall. Strain gauges, manufactured by HBM, were series Y 90-degree 'T' rosettes with a 6.0 mm measurement grid length, model K-CXY3-0060-1-350-4-050-N and attached to the pipeline with HBM Z70 adhesive. Strain measurements were recorded using an EDAQ Lite manufactured by HBM with an 8-channel Wheatstone bridge layer. A sample rate of 5 K sec⁻¹ was used. The EDAQ was powered by one 12-V battery connected to a 20 W solar panel. Both the EDAQ and seismographs were connected to modems to allow remote downloading of data via telemetry as needed.

Strain gauge data were filtered and time histories analysed for crown and springline peak hoop and longitudinal strains representing strain at localised sites of mounting. Pipe-mounted velocity records were integrated to calculate displacement time histories to determine peak global axial strains between the connection at the pier top and midspan and bending strains at the midspan.

This project provided the opportunity to compare midspan global elongation strains computed using velocity sensors with strain gauge measurements for an elevated pipeline. To the authors' knowledge, this has never been performed. For this comparison, a total axial strain was computed with contributions from both pure axial elongation, derived from the geophone radial (R) component parallel with the pipe, and bending in each the vertical and lateral directions. Perpendicular vertical motions (V component) contributed to bending strains at the crown while perpendicular horizontal motions (T component)



contributed to bending strains at the springline. It was not possible to compute hoop strains from geophone measurements.

4 RESULTS

4.1 Ground motions

Table 2. Ground vibrations in terms of velocity (V) and displacements (D) measured at the base of P13.

Blast	RADIAL		VERTICAL		TRANSVERSE	
	V	D	V	D	V	D
	(mm/s)	(mm)	(mm/s)	(mm)	(mm/s)	(mm)
1	6.1	0.036	12.8	0.148	7.1	0.091
2	16.3	0.229	34.5	0.279	29.2	0.262
3	10.9	0.141	17.0	0.072	14.2	0.147
4	9.7	0.053	17.7	0.153	7.0	0.104
5	10.8	0.077	18.1	0.142	14.8	0.126
6	12.4	0.168	13.7	0.122	18.7	0.170
7	6.8	0.049	10.6	0.163	6.0	0.092
8	3.8	0.019	5.6	0.040	4.9	0.027

A summary of ground motions in terms of velocity and displacements are given in Table 2. Component ground velocities at the closest pier support base ranged 5 to 34.5 mm/s. Peak frequencies for all components averaged 53 Hz. As such, the highest ground displacements were

only 0.279 and 0.262 mm in the vertical and transverse directions.

4.2 Pipeline vibration response - natural frequency and damping

Figure 4 shows typical component velocity time histories measured at the midspan crown for blast 7 and the near harmonic blast response in the V and T components. The fundamental frequencies in the T component were a consistent 3.8 Hz with damped oscillations lasting up to 20 sec. The V component was initially 7.3 Hz reducing to 5.2 Hz lasting well over 20 sec. The percentage of critical damping for the T component (β) was approximated for the T and R components computed using the following relationship:

$$\beta (\%) = \frac{1}{2\pi} \left(\ln \frac{P_2}{P_1} \right) \quad (1)$$

where P_2 and P_1 are successive peaks. In this case, damping in the T component is 2.8% and is typical of the range of damping for all blasts.

4.3 Strain Measurements

Table 3 presents a summary of pipe strain measurements at the crown and springline atop of

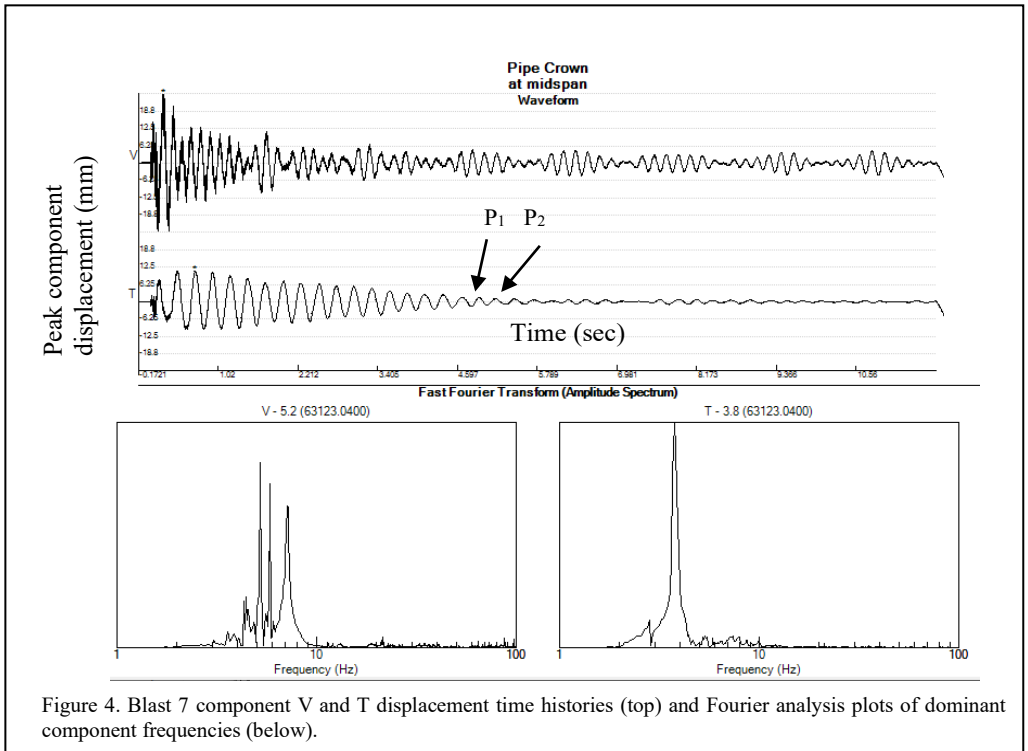


Table 3. Maximum hoop and longitudinal pipe strains at the crown and springline of the midspan and at the pier top for eight blasts.

Blast	MIDSPAN Measured strain ($\mu\epsilon$)				PIER Measured strain ($\mu\epsilon$)			
	Hoop (ϵ_L)		Longitudinal (ϵ_H)		Hoop (ϵ_L)		Longitudinal (ϵ_H)	
	crown	springline	crown	springline	crown	springline	crown	springline
1	2.69	6.72	7.50	3.22	2.82	2.07	4.56	1.53
2	6.93	13.22	19.9	10.0	8.49	4.15	10.20	5.18
3	8.72	nu	20.2	20.0	14.14	6.30	12.91	4.56
4	7.97	4.28	14.0	6.37	8.52	2.96	7.99	3.11
5	3.34	nu	4.22	5.19	3.67	2.54	3.69	2.44
6	3.37	nu	5.03	5.26	3.51	2.21	4.57	3.44
7	4.22	5.01	8.89	4.60	3.94	2.28	6.26	2.92
8	2.12	nu	2.23	nu	nm			

nu - not usable; strain data within the noise

nm - not measured

the pier and at the midspan. Typical strain time histories are provided in Figure 5 for blast 3 over the initial 0.5 sec recording time. The pipe crown longitudinal peaks at the pier support shows uniform 166 Hz oscillations while the hoop crown frequencies are less uniform, averaging of 132 Hz.

Time histories clearly show an underlying low frequency component that persists in the pipe in the vertical and lateral components in some cases well over 20 sec. Interestingly, these pipe displacement oscillations are perfectly matched by strain gauge records as demonstrated in Figure 6 at the crown and springline during blast 7. The strain gauge and displacement time histories are compared over a 10-sec window and show the same overall response characteristics.

4.4 Blast-induced pipeline wall stresses

Pipeline integrity engineers are responsible for the performance of pipelines carrying liquids and gases ensuring that pipeline operations meet standards and requirements for safety and regulations. It is often the case that pipeline engineers are not acquainted with the safety precautions exercised by blasters and monitoring experts to ensure pipelines can be protected to a high safety factor when subjected to transient blast excitations at distances beyond permanent rock displacement limits of the blast.

To illustrate the degree of safety to which shaft blasting was performed, factors of safety (FOS) were computed for the pipeline by considering

hoop and elongation stresses generated during blasting based on measured strains at the crown. Dynamic elongation limits are set by the minimum yield strength for grade C steel shown in Table 1 as 206.8 MPa while allowable hoop stress is set by a design factor applied to yield. For the aged pipe, the monitoring team applied a 50% reduction factor or 103.4 MPa. The pipe working pressure of 1.3 MPa in the absence of possible surge pressures were low and not included in the stress calculations.

Biaxial stress-strain equations were used to compute longitudinal (axial) and hoop stress based on measured strains are:

$$\sigma_L = \left(\frac{E}{(1-\nu^2)} \right) (\epsilon_L + \nu \epsilon_H) \quad (2)$$

$$\sigma_H = \left(\frac{E}{(1-\nu^2)} \right) (\epsilon_H + \nu \epsilon_L) \quad (3)$$

Where σ_L and σ_H are longitudinal and hoop stress, ν is Poisson's ratio of 0.3, and E is the modulus of elasticity (200 GPa).

Blast 3 generated the highest strains. Midspan hoop and longitudinal stresses were 3.3 and 5.0 MPa resulting in FOS values of 31 (103.4/3.3) and 41 (206.8/5.0), respectively. At the pier top, hoop and longitudinal stresses were less than 4.0 and 3.8 MPa resulting is FOS greater than 26 and 54. Clearly, shaft blasting generating very low strain amplitudes was highly protective of the elevated pipeline.

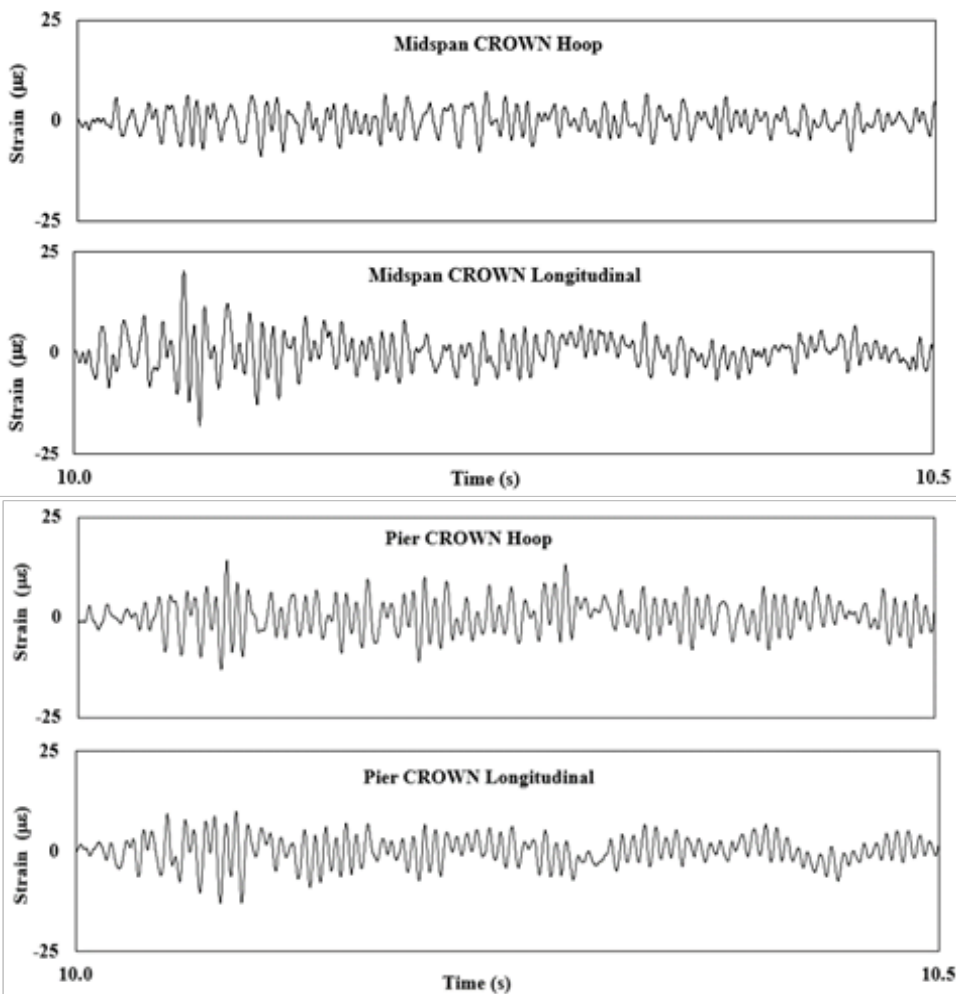


Figure 5. Pipeline crown hoop and longitudinal strain time histories recorded during blast 3 at the midspan and at the pipe overlying pier P13 showing 10 Hz and 7.3 Hz underlying frequencies at the pier top and midspan, respectively.

Table 4. Global strains compared with measured strains (all units are µε).

Blast	Computed Strains							Measured axial strains	
	Shear		Peak Pure Axial	Peak Bending		Time-correlated Computed total axial strain			
	vertical (V)	horizontal (T)	radial (R)	crown	springline	crown	springline	crown	springline
1	34.0	19.2	8.5	3.3	1.9	11.0	8.8	7.5	3.2
2	not measured							19.9	10.0
3	35.3	46.9	16.1	1.3	1.8	17.0	16.4	20.2	20.0
4	35.3	36.6	8.7	3.4	3.5	11.1	10.1	14.0	6.4
5	12.6	23.0	3.1	1.2	2.2	4.1	4.2	4.2	5.2
6	12.9	26.6	4.1	1.3	2.6	4.4	5.3	5.0	5.3
7	44.2	30.8	9.9	4.3	3.0	13.0	10.9	8.9	4.6

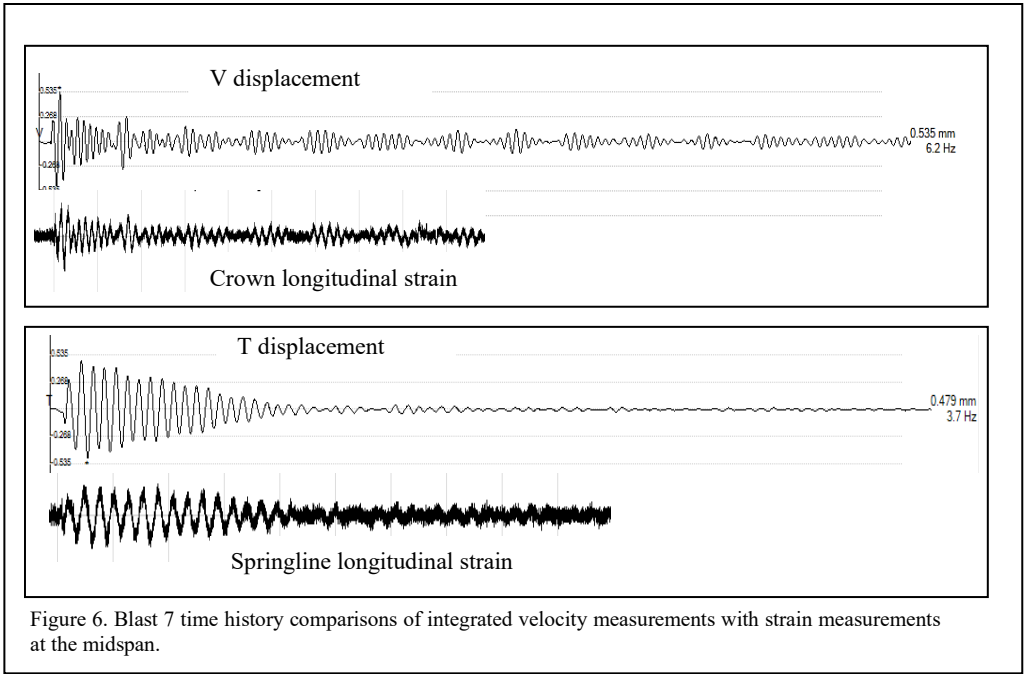


Figure 6. Blast 7 time history comparisons of integrated velocity measurements with strain measurements at the midspan.

4.5 Computed axial global strains compared with measured strains

There is great interest in using velocity transducers to globally estimate blast-induced strains in pipelines based on the ease of field deployment and reliability of long-term measurements in comparison to the difficulties strain gauges can pose. In this regard, global axial strains computed from time correlated differential displacements between the pier top and midspan measured using velocity sensors at the pipe crown were compared with measured axial elongation strains at the crown and springline to establish correlations. These data are summarized in Table 4.

Shear strain in the vertical, transverse (perpendicular to the pipe axis), and pure axial (elongation) strains in the radial are simply $\Delta\delta_i/(L/2)$, where $L/2$ is the half span length between supports and $\Delta\delta_i$ the maximum time-correlated differential deflection between the pier and midspan displacement measurements integrated from velocities where $i = V, T,$ or R component. The bending strain (ϵ_b) is computed as:

$$\epsilon_b = \frac{(\delta_{max} \epsilon D)}{L^2} \quad (4)$$

where δ_{max} is the time correlated differential displacement in either the V or T directions

applied at the crown and springline, respectively, D is pipe outside radius, and L is the full length of the unsupported pipe (Dowding 1985). Total axial strain is the maximum of time-correlated addition of both the pure axial and the bending. Note the total axial is not the sum of the peak axial and peak bending as constructive and destructive strain addition occurred at different points in strain-time history.

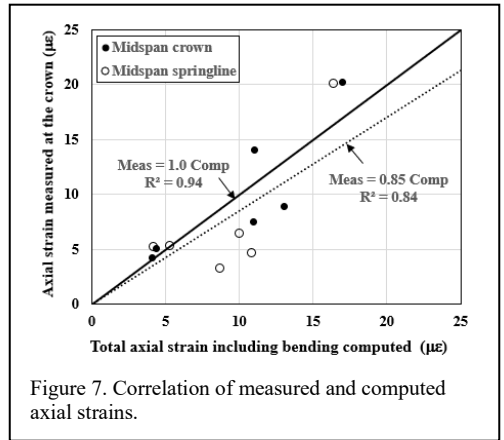


Figure 7. Correlation of measured and computed axial strains.

Computed total axial strains are compared to measured longitudinal strains in Figure 7 at the midspan. Strong correlations exist for both the crown and springline. However, computed

springline strains overestimate the actual, local strains, likely due to the location of the geophone used for computation, which was only on the pipe crown. On average, the computed crown strain is nearly a perfect predictor for actual, local strain with a relationship factor of 1.0 and correlation coefficient of 0.94.

4.6 Amplification of pipe response

Displacements time history plots over 5 sec are given in Figure 8 for blast 4 comparing ground vibration measurements with the pipe overlying the pier (a) and with the midspan (b). Although the main blasting ground excitation lasted 90

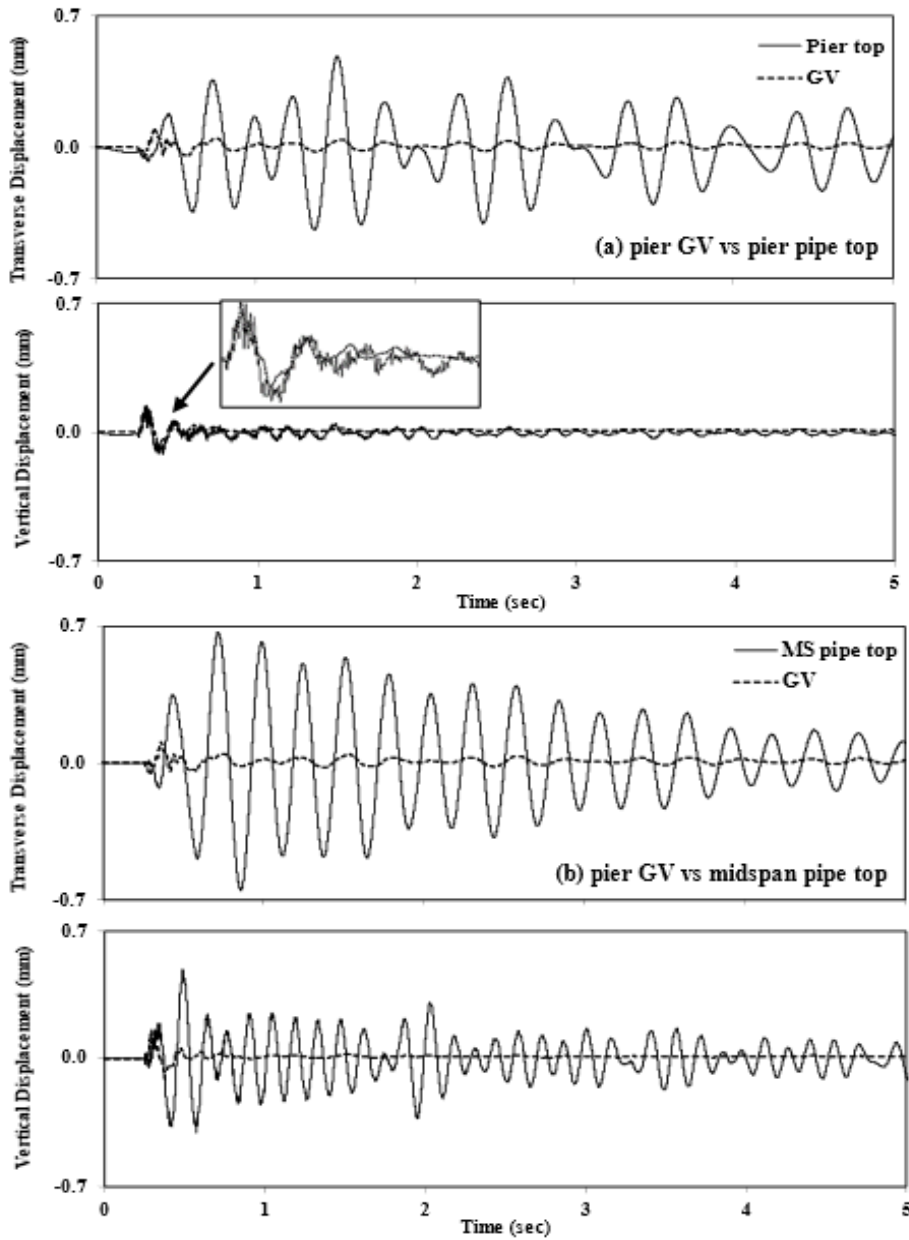


Figure 8. Blast 4 transverse and vertical displacement time histories comparing (a) ground vibrations at the pier base and top of the pipe overlying the pier, (b) ground vibrations at the pier base with the midspan pipe top.

milli-seconds, low amplitude horizontal ground motions continued for well over 10 seconds at predominant frequencies of 2.8 and 3.8 Hz. This long-term, residual ground motion is likely due to the saturated ground around the pier bases within the river floodplain. The residual ground motions matched the natural frequency of the pipe midspan which was 3.8 Hz, as shown in Figure 5, resulting in high amplifications in the midspan and pier top lateral directions relative to transverse ground excitations. Similar lateral amplification was observed between the ground and pier top while vertical motions were not amplified and somewhat constrained by the ring supports.

Maximum amplifications of ground motions at the pier midspan crown for shallowest and deepest shaft blasts and one tunnel heading round are shown in Table 5 in terms of displacements. Time-correlated values are computed as maximum differential displacement between the pipe and ground divided by the ground. In general, vertical amplifications decreased with blast depth while transverse amplifications increased with increased confinement. The tunnel heading round with horizontally drilled holes generated the highest and lowest transverse and vertical amplifications, respectively. Despite the amplifications, the phase of oscillations match in most comparisons resulting in the observed low strains.

Deploying triaxial velocity transducers onto the pipeline surface is far easier and provides a stable measurement system in comparison to the challenges affixing strain gauges onto the surface for long-term measurements.

REFERENCES

- American Water Works Association (AWWA). 2017. M11 Steel Pipe: A Guide for Design and Installation, Fifth Edition.
- Bonds, R. W. 2017. Design of ductile iron pipe on supports. *Ductile Iron Pipe Research Association (DIPRA)*.
- Dowding, C. H. 1985. Blast vibration monitoring and control. Prentice-Hall, Inc.

Table 5. Amplification of crown midspan relative to ground motions by component.

Blast	Vertical	Transverse
1 shaft	46.8	13.3
5 tunnel	2.8	50.4
7 shaft	10.7	38.6

5 CONCLUSIONS

Ground vibrations from shaft blasting within a river floodplain generated low frequency, in-phase response of an elevated pipeline. Measured hoop and axial pipe strains were deemed highly protective of the pipe integrity and far below allowable yield stresses for grade C steel resulting in a minimum FOS of 26. Using velocity transducers affixed to the pipe crown to compute time-correlated, global axial strains with contributions from pure axial elongation and perpendicular bending appears to be an acceptable approximation of measured axial (longitudinal)

Magnitude 2.8 Earthquake Caused by 90 Pounds (41 kg) Per Delay! Not So Fast

T.A. Davidsavor, P.E. & J. Aiken

Barr Engineering Co., Duluth & Minneapolis, Minnesota, USA

R.E. Burnham, & J.K. Ratliff

Reminger Co., L.P.A., Fort Mitchell, Kentucky, USA

I.G. Wong

Lettis Consultants International, Concord, California, USA

C.T. Aimone-Martin

Aimone-Martin Associates, LLC, Lemitar, New Mexico, USA

ABSTRACT: A small quarry blast was conducted and shortly afterwards, area residents sensed ground motion and building shaking indicative of an earthquake. In addition, seismometers up to 250 miles (400 km) away recorded a magnitude 2.8 earthquake located in the area. Positioned in a seismically inactive area, southern Minnesota is not known for earthquakes. The earthquake was originally described by the USGS to be a surface blast at the quarry. Analysis showed that the earthquake occurred shortly (approximately seven seconds) after the quarry blast some distance away and well below the surface. This paper describes the evaluation of the 'seismic events' including the blast, the following earthquake, initial governmental response, and provides the framework for assessing the relationship between the blast and the earthquake. The paper also discusses management of large volume claims from a complex event and presents a claims management strategy with best practices.

1 INTRODUCTION

On April 25, 2017 at approximately 11:00 am CDT a routine controlled quarry blast was conducted at the Jefferson Quarry located in Mankato, Minnesota, Unites States of America. The blast was a regularly performed activity in a region of the United States well known for production of high-quality dimension stone and proppant used in the fracking process of hydrocarbon production. Mankato and its sister city, North Mankato, comprise a city of approximately 60,000 people. The Jefferson Quarry had been active for several

decades and is in the middle of the city. The project location is shown in Figure 1.

Shortly after the blast, some Mankato area residents reported perceptions of ground motion, shaking of objects, as well as sensations of building movement in the downtown Mankato area. In addition, seismometers up to 400 km (~250) miles away recorded a 2.8 magnitude earthquake in the area. The earthquake was originally described by the United States Geological Survey (USGS) to be a surface blast at the Jefferson Quarry. Early media reports attributed the reported ground vibration as a



Figure 1. Site location – Mankato, Minnesota, USA.

weather-related phenomenon associated with the quarry blast. Ground motion was noted by residents throughout the area and media coverage of the rare seismic event was extensive. Social media aided in documenting some of the initial responses. After the earthquake, which was unlike any observed seismic activity in the past decades of blasting, numerous damage claims were made. The quarry owners and contractors acted quickly to offer evaluation of property conditions to those who claimed damage from the earthquake. In most cases, the claimed damage was found to obviously have occurred before the seismic event.

How was such a ground motion possible from a normal blast pattern which utilised a maximum of 41 kg (90 lb) of bulk emulsion per delay? Immediately after the earthquake, teams focused on assessing how the blast may have caused the earthquake, how to evaluate and resolve damage claims, and how to permit the mine to return to production as the blasting was not substantially different than any other blast performed at the property. In assessing the seismic event, Barr's blasting engineers, mining engineers, and geologists, with the assistance of seismologists at Lettis Consultants, adopted a multiple working hypothesis approach that included collecting available data, evaluating reasonable explanations, and attempted to find the best fit to explain the observations. The best fit explanation for the observed effects was that the timing of the quarry blast with the earthquake that occurred approximately 7 seconds later was simply coincidence. As a result of the Barr Engineering report, the quarry's permit to operate was reinstated. However, the public was not entirely satisfied with the study revealing several interesting gaps in our ability to communicate

information about blasting to the general public as well as persistent myths about blasting, ground vibrations, and their connection to effects on structures. The law firm of Reminger was assisted by Dr. Aimone-Martin and focused on establishing a process for claimants, assessing damage claims, and providing claim resolution on behalf of their client, the insurer, and the contract blaster.

2 BACKGROUND

To provide context on the project, background related to the blasting practices, geology, and seismic records are provided.

2.1 Geologic background

The Jefferson Quarry is located where the Early Ordovician Prairie du Chien Group is exposed in the bluffs of the Minnesota River. Early mining at the property an in the general area focused on production of high quality, thick-bedded Oneota Dolomite, which was used extensively as building stone and high-quality aggregate products. The underlying Jordan Sandstone is Upper Cambrian and was found historically to be an ideal source of silica for glass making and more recently, as a proppant. The Jordan Sandstone is known to be well-sorted and consist of well-rounded sediments which are highly durable. As a result of the size and mechanical properties of the sand grains, the Jordan Formation is mined extensively as a proppant for hydraulic fracturing. The sand is processed and added to fracking fluids for the purpose of keeping induced hydraulic fractures open. The consistency of the Jordan Sandstone combined with the thickness of the unit, its relatively poor cementation, and its proximity to major waterways and roadways has caused the

sandstone to be heavily mined in the area and shipped across the United States. Blasting for the development of the sandstone is performed to allow excavation.

2.2 Blasting background

Blasting in the sandstone utilized 101 mm (4-inch) diameter holes on a 9.1 m (30 ft) bench that are drilled to a depth of approximately 10.1 m (33 ft) below grade to allow for sloughing of material in the holes. The design depth for the explosive column was on average 8.5 m (28 ft) with no subdrill. The holes were typically water-filled due to operations occurring in the base of the quarry. The drill pattern was based on a 3.7 m (12 ft) burden and a 4.3 m (14 ft) spacing and each blast generally contained 30 to 65 holes in a staggered pattern. Stemming heights have varied from 1.8 m to 4.9 m (6 to 16 ft) with 9.5 mm (3/4 inch) crushed stone used as the stemming material. The explosive used in the sandstone was an emulsion/ANFO blend consisting of 70% emulsion and 30% ANFO. The density of this product is 1.28 to 1.30 g/cc. The emulsion blend is pumped from the bottom of the hole. The holes were primed with one 500 gram (1 lb) cast booster. Non-electric detonators were used to initiate each blast hole. The blast used a timing of 42 ms between holes in a row and 67 ms between rows.

Blasting was conducted in a typical bench blasting operation (with or without free faces) depending on the area and the local circumstances. The Jefferson Quarry is located near a residential area with homes in relatively close proximity to the operation, so there was the potential for ground vibrations and/or airblasts from the operation to be perceived by nearby residential homeowners and these issues were considered in design and past blast execution.

A review of the past blasting activities found a total of 55 blasts had occurred at the site in the preceding year with an average charge weight/delay for all blasts in the past year at 31 kg (68 lb) and the charge weight/delay had varied from 12 to 59 kg (27 to 130 lb). The charge weight/delay for the blast on April 25, 2017, was 41 kg (90 lb) per delay. Based upon standard rules of attenuation, the amplitude of the ground vibration at 300 m (1000 ft) from a blast using a charge weight of 31 kg (68 lb) would be 4.3 mm/s (0.17 in/sec), whereas a charge weight of 41 kg (90 lb) at the same distance would yield a ground vibration amplitude of 5.3 mm/s (0.21 in/sec), which is not able to be differentiated by the average human.

The average powder factor for all blasts the previous year had been 0.32 lbs./ton and the powder factor ranged from 0.12 kg/ton to .21 kg/ton (0.24 to 0.42 lbs./ton). The powder factor

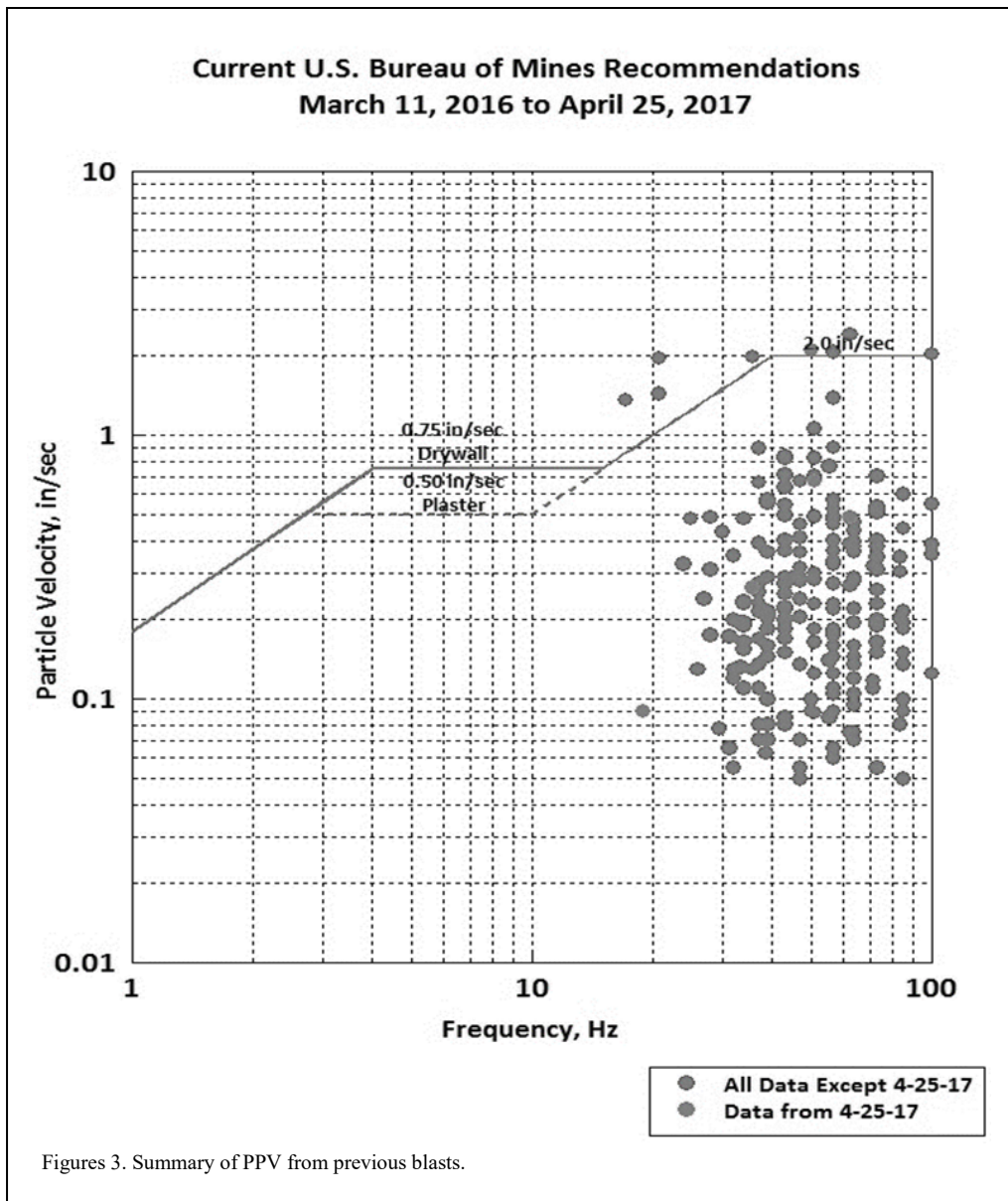


Figure 2. Sandstone upon blasting/seismic event.

for the blast on April 25, 2017, was 0.17 kg/ton (0.23 lbs./ton), the lowest powder factor over the past year. The Jordan Sandstone is a consolidated formation but is only lightly cemented and does not require much energy to loosen the material for excavation, so the lower powder factor for the blast on April 25, 2017 was not significantly low enough to be a concern. Figure 2 shows the blast area after the April 25, 2017 blast indicating the blast performed normally with no evidence of unusual performance.

2.3 Blasting seismic data

Ground vibrations were recorded by Vibra-Tech from the blast on April 25, 2017 and the peak particle velocities (PPV) at several locations were very similar to the past blasting activities with the maximum PPV recorded on the mine property at a distance of 74 m (243 ft) at 53.6 mm/s (2.11 in/s) at a frequency of 50 hertz and at a nearby residence at a distance of 195 m (640 ft) within the US Bureau of Mines recommended limits set forth



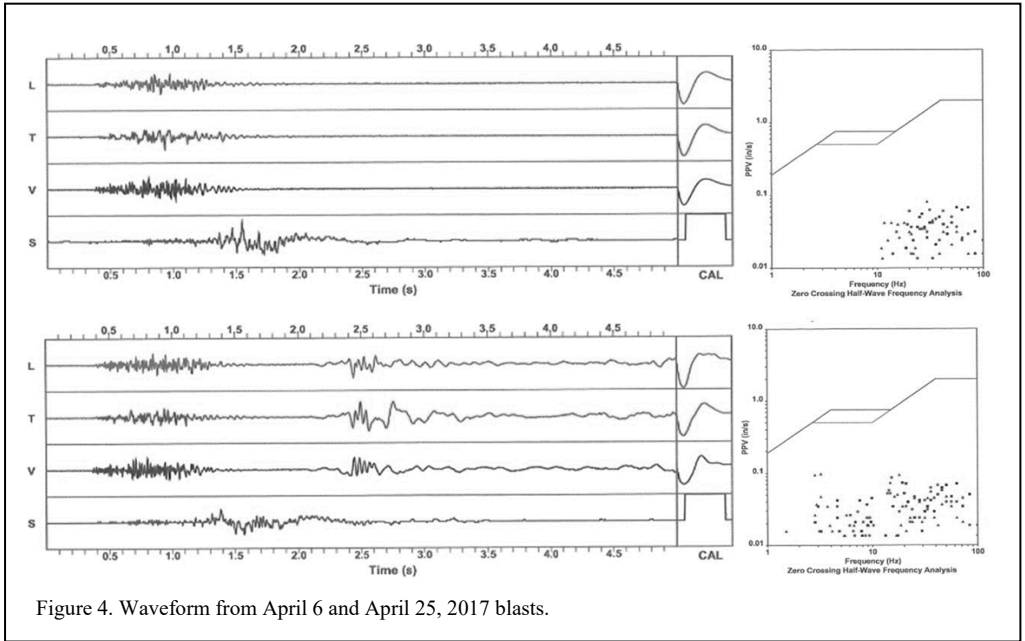


Figure 4. Waveform from April 6 and April 25, 2017 blasts.

in Report of Investigation 8507 at 17 mm/s (0.67 in/s) at 51 hertz. A seismograph at a home at a distance of 254 m (834 ft) recorded a PPV of 12 mm/s (0.49 in/s) at a frequency of 62.5 hertz. A similar PPV of 6.7 mm/s (0.265 in/s) was recorded at a distance of 277 m (907 ft) at a similar frequency of 35.7 hertz. A seismograph located at the city wastewater treatment plant at a distance of (1083 ft) recorded an initial PPV of (0.093 in/s) with general frequencies above 10 hertz, much higher than another separate impulse with the same magnitude, but with frequencies of about 3 hertz. Figure 3 provides the waveform recorded at the nearby wastewater treatment plant on April 6, 2017, and of the blast that occurred on April 25, 2017. The second event (the earthquake) with significantly lower frequency is clearly visible in the record. Figure 4 provides a summary of the PPV from all blast events recorded over the past year. The data in Figure 4 plots the recorded PPV and frequency of the peak, clearly showing the April 25, 2017 blast behaved very much in line with the previous blasting at the property.

From the summary of the recently blasting data, Figure 4 shows that the PPV from the April 25, 2017 blast falls within the bounds of the historical data for blasts in the Jordan Sandstone formation. Vibra-Tech aided the team greatly in seismic data summary and analysis to evaluate the blast in question in comparison to past blasting

activity. Since the blast appeared unremarkable, seismologists were engaged.

3 UNEXPECTED OUTCOME

Earthquakes in Minnesota are rare and according to Chandler (2020), “Minnesota has one of the lowest occurrence levels of earthquakes in the United States, but a total of 20 small to moderate earthquakes have been documented since 1860.” These earthquake locations and the location of documented regional faults are shown in Figure 5.

The most intense documented earthquake was the Long Prairie earthquake (location 1) in 1860 and was estimated to be a magnitude 5. Others including a magnitude 4.7 (New Prague, location 2, 1860), a magnitude 4.6 to 4.8 (Morris, location 11, 1975), and a magnitude 4.1 (Dumont, location 18, 1993) in addition to an additional 13 greater than magnitude 2.8 have been documented. The nearest previous earthquake to Mankato was centered near New Ulm (40 km, 25 miles northwest of Mankato) in 1881 and was estimated to be between magnitude 3.0 and 4.0.

The USGS located the event at the Jefferson Quarry despite an apparent discrepancy between the relatively large magnitude of the event and that expected from a quarry blast. This was possible due to the relatively large uncertainty associated with automated location of the event using sparse seismograph coverage. Their automated solutions

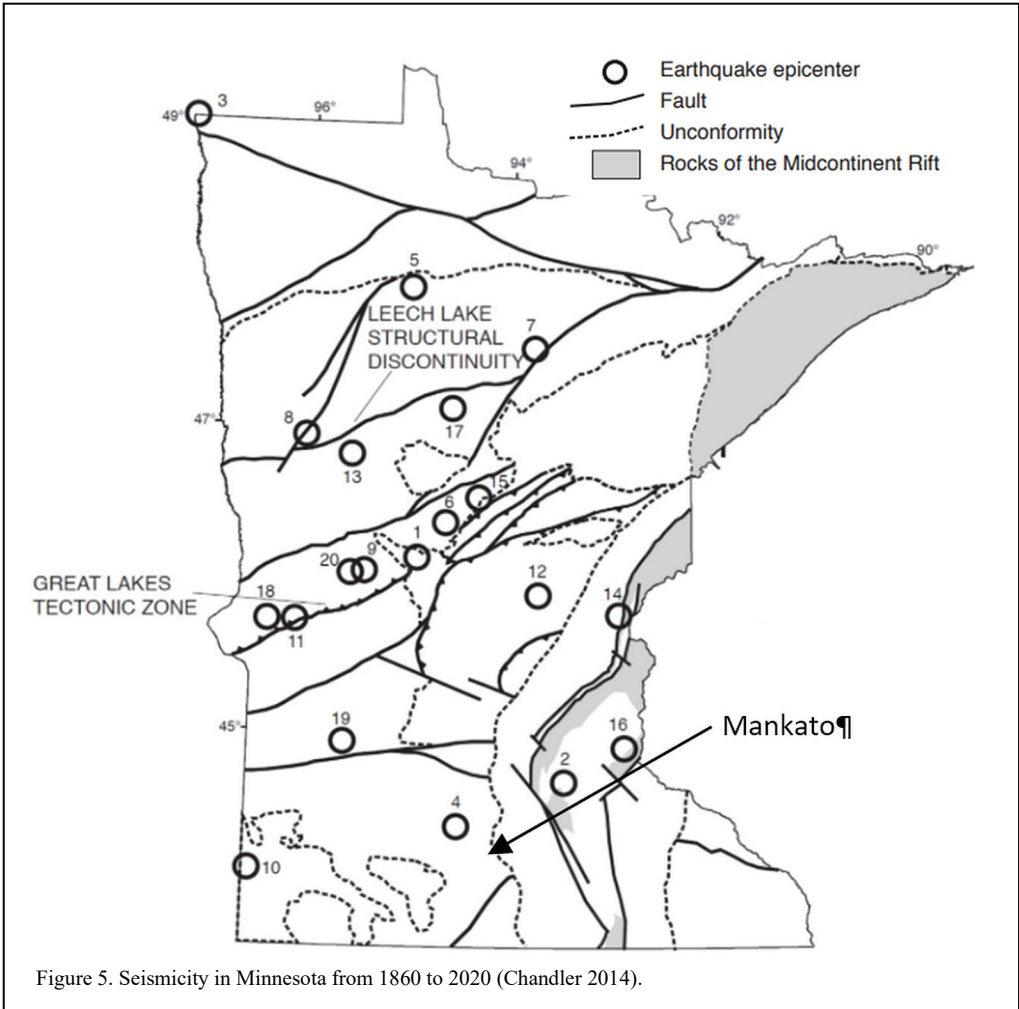


Figure 5. Seismicity in Minnesota from 1860 to 2020 (Chandler 2014).

were based only on P-wave arrival times and resulted in locations at 6 km northwest of the Jefferson Quarry, with depth at 8 km +/- 10 km. Given the range of uncertainty, and media reports circulating about the earthquake occurring at about the same time as the quarry blast, they located it at the Jefferson Quarry without a thorough review of available data. The USGS was not able to refine the location of the epicentre accurately using standard automated modelling and initially located the epicentre near another quarry approximately 10 km (6 mi) north of the Jefferson Quarry. Other modelled locations were further to the southwest. Ultimately, the USGS attempted to find the best fit for the data and settled on the Jefferson Quarry in Mankato. According to the USGS, there were questions about the energy levels possible to cause a response on a seismometer over 200 km (125 mi)

away, but given the uncertainty caused by relatively few seismic monitors in area, they settled on the quarry as a reasonable location.

3.1 Media and Social Media response

It seems clear that media reports, social media response to those reports, as well as web-based crowd sourced information played a significant role in identifying the Jefferson Quarry as the source of the earthquake. Perhaps the biggest role was that of the gap in understanding between the energy levels involved in a typical quarry blast as compared to the energy required to cause an earthquake that is felt hundreds of kilometres from the source area. Had the operators of the Jefferson Quarry known at the time that the earthquake occurred several seconds after the blast, they may

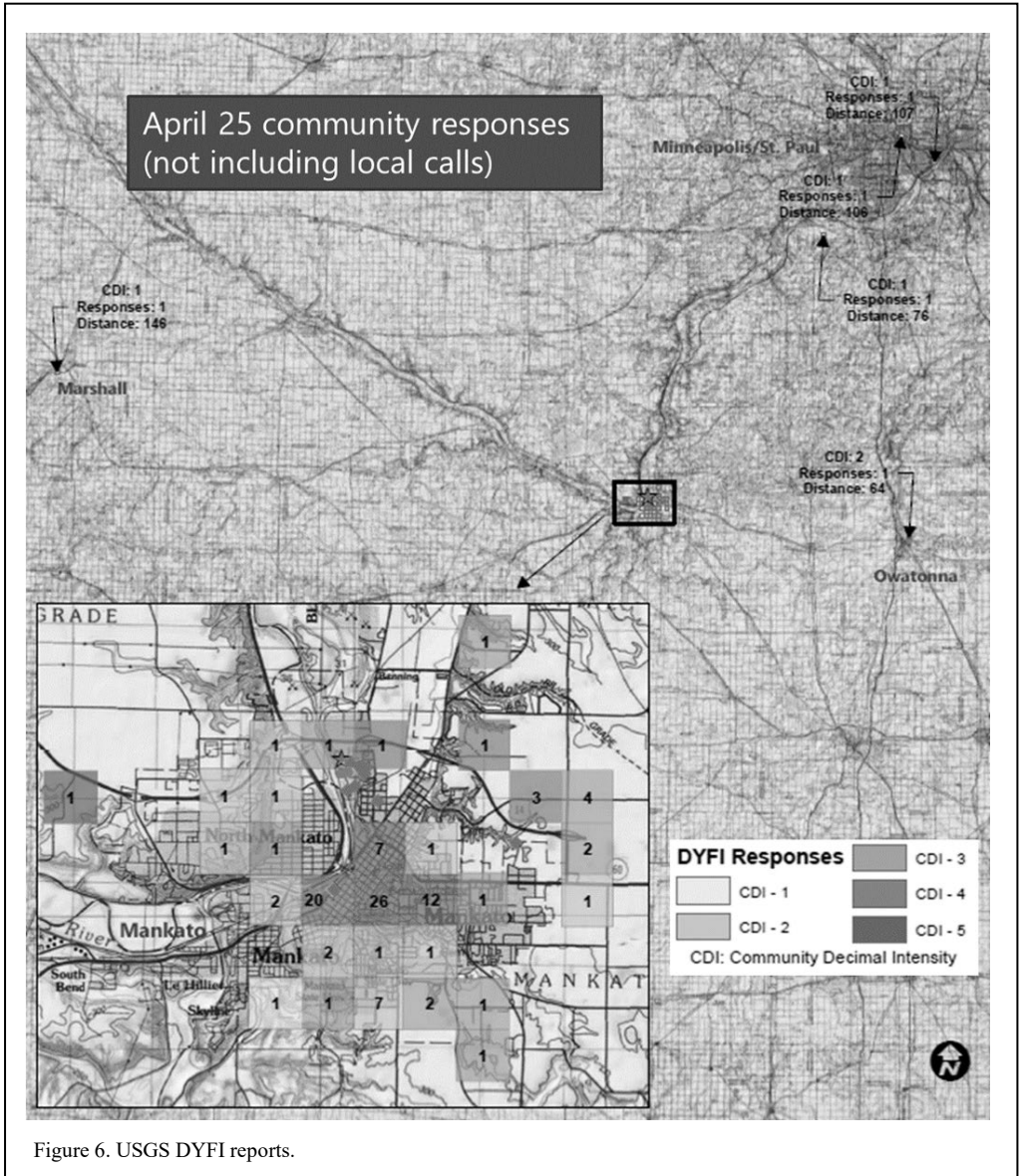


Figure 6. USGS DYFI reports.

have made different statements to the media. However, the proximity in time resulted in the assumption that the two events were correlated. While the traditional media and social media reports were putting out information linking the Jefferson Quarry to the earthquake, the USGS was running automated software that put the epicentre somewhere near downtown Mankato. It is not known why the USGS decided to attribute the earthquake to a quarry blast. However, it is known that the USGS made their determination and selected the Jefferson Quarry after assigning

preliminary locations that did not identify the Jefferson Quarry.

It's a fair assumption that most scientists do not regard social media as a reliable or even useful means to conduct scientific inquiry. However, in this case, there was information available from a large crowd sourced data platform hosted by USGS called 'Did you Feel it.' Most responses were from the downtown Mankato area which is not unusual given the greater population density than more rural areas. However, it was notable that despite the comparable geology and population

density between the downtown area and the area near the Jefferson Quarry, there were proportionately more subjective reports of shaking to the south of the Jefferson Quarry that fit the modelled locations by LCI. Figure 6 shows the frequency and locations of the DYFI reports.

The social media reports combined with the location model added confidence to an epicentre location that was significantly different from the location initially identified by the USGS.

3.2 Felt reports

To add an additional constraint to the assessment of the location of this earthquake, data collected by the USGS on felt intensities is shown in Figure 6. These data are earthquake effects reported by citizens aggregated in geocoded squares 1 km in size. The traditional Modified Mercalli (MM) felt intensities are converted to Community Decimal Intensities (CDI) to give an average assessment of felt effects in the box. Although the CDI maps are prone to bias (population density, type of structures, interest in reporting, etc.) it can provide useful, if anecdotal, information on the location of the earthquake epicentre. In Figure 6 the locations of the geocoded boxes are identified by squares and are labelled with the CDI for that box. The palest shading indicates a CDI of 1 where the darkest shading indicates a CDI of 5 and the number in each block indicates the reports on the DYFI and does not include local calls. Most responses are in the centre of Mankato with CDI corresponding to the MMI values of III-IV. Comparing the relocated epicentres for this study and the CDI data suggests that the earthquake epicentre is located south of the Jefferson Quarry and not at the locations determined by the NEIC.

4 USGS RESPONSE

In an email exchange with the Director of the National Earthquake Information Centre (NEIC) of the USGS, we learned that the earthquake located by the NEIC had its location fixed at the Jefferson Quarry because their free location was sufficiently close to the Jefferson Quarry that they could not distinguish it from the Jefferson Quarry given the location uncertainties. The USGS believed the timing of the event coincided with the blast, but they did question the origin of the event because it seemed too large for a blast. The event was initially located by the NEIC in response to news reports of strong ground shaking in the Mankato area. The NEIC fixed the location at the Jefferson Quarry and indicated that there are two

additional solutions, one with the depth fixed at the surface and one in which the depth was allowed to vary along with the other hypocentral parameters. The NEIC location in which the focal depth was fixed at the surface and the epicentral location was allowed to vary, locates 4 km northwest of the Jefferson Quarry. The NEIC solution in which all the parameters were allowed to vary is located 6 km north of the Jefferson Quarry. The focal depth for this solution was 10 ± 8 km. Therefore, the NEIC locations have considerable uncertainties associated with them.

In February of 2022, the National Earthquake Information Centre of the USGS acknowledged that the event was an earthquake and updated the event to include the following text: "Based on news media reports, low regional seismicity, and proximity to a quarry, this event was originally labelled a quarry blast. Subsequent independent analysis of nearby data shows the signals observed on the regional seismograms are most likely from an earthquake. The observed event is most likely an earthquake that occurred several seconds after a quarry blast."

5 SEISMIC ANALYSIS

It was apparent that the energy released by the 41 kg/delay (90 lb/delay) quarry blast was not capable of producing ground motions that were felt as far away as 235 km (146 mi), and a separate earthquake was the concern. Barr teamed with Ivan Wong, of Lettis Consultants International (LCI), to evaluate the seismic data, locate the hypocentre of the earthquake and to opine on the comparative energy and seismic signature of the quarry blast. LCI found that although a precise location was difficult to calculate due to the paucity of nearby seismographs, it could be concluded that the quarry was most certainly not the hypocentre of the quake. Using standard seismological techniques and selection of an appropriate crustal model, the hypocentre was likely several miles south of the quarry, and at least 1 km below the surface.

The earthquake epicentre was assessed using the program HYPOINVERSE-2000 (version 1.40, Klein 2014) to verify the NEIC locations and to test the sensitivity of these locations to variations in crustal velocity structure. HYPOINVERSE is an earthquake location algorithm developed by the USGS that has become the standard for locating earthquakes and other seismic events throughout the U.S. Its purpose is to use the arrival times of seismic P- and S-waves records at seismograph stations and calculate the event location.

It requires as input a velocity model of the crust, a list of station locations, and a file of seismic phase arrival times. The relocation procedure focused on improving the selection of P-wave arrival times, adding S-wave arrival times, and using several different regional velocity models to evaluate the sensitivity of the solutions to variations in crustal velocity.

The seismograms from the regional seismograph stations were obtained from the Incorporated Research Institutions for Seismology (IRIS) website (download date 19 May 2017). Records of the event were from three-component broadband seismometers ranging in distance from 50 to 800 km away. The initial NEIC location only used the P-wave arrival times. These arrivals were reviewed and in some cases the P-wave arrival time was repicked. The event was relocated using a simple three-layer velocity model and the travel time residuals examined to assess the accuracy of the pick. Then the S-wave phase arrival times were picked. The S-wave phase is more prominent on the records than the P-wave arrivals, which were often very emergent. Adding S-wave phase data to the location procedure is very useful in constraining the hypocentral location. The event was relocated to check the accuracy of S arrivals.

Once confidence was established in the selected phase arrival times, the event was relocated several times using different velocity models. These models were taken from the literature and were selected based on how well they represented the average crustal velocity of the North American Midcontinent. Because most of the stations are at least 100 km from Mankato, the details of velocity variation near the surface is unimportant. At these distances, most of the seismic energy travels through the mid to lower crust or is refracted along the Moho. The closest station, N4I37B, was about 50 km from the Jefferson Quarry and several relocations were made using a model relevant to the crustal structure in the Mankato region. This was the Gambler High model (Braile 1989), which is tied to the midcontinental gravity high that extends from Lake Superior southwest to about the latitude of Mankato. While the use of a specific velocity model for station N4I37B resulted in reasonably good hypocentral solutions, it was not materially different from those solutions using just a single model for all stations. HYPOINVERSE was run numerous times using several velocity models and different weighting schemes for the P and S arrival times to arrive at a suite of hypocentral solutions with acceptable error statistics.

Only solutions that had an RMS error of less than 0.30 sec were considered. The focal depths range from very shallow (0.4 km) to mid-crustal depths (10 km). The horizontal errors are on the order of 1 km and the vertical errors range from 1 to 2 km. Since the location statistics are very similar for each of these model runs, it is difficult to select the best solution. This is often the case for earthquakes that are located using data from regional seismograph stations. Unless there is a station within about 10 km of the epicentre, locations are typically not well constrained.

5.1 Can a blast cause an earthquake?

The assessment simply concluded that there was no evidence of a causal relationship due to the relatively small energy of a blast compared with the much higher levels associated with ground movement felt hundreds of kilometres away. One possible theory is the ‘hair-trigger’ hypothesis which states that tectonic stresses are so high that a small stress perturbation is sufficient to set off a critically stressed fault. The problem with this argument is plausibility. Every week there are hundreds of quarry blasts within the roughly 200 km range of the seismographs that reported this earthquake, including dozens of blasts that had occurred before this event at this same quarry as well as at least a half dozen other quarries in the vicinity of Mankato. If the stress build-up on a fault was so close to rupture that a relatively small blast and/or accompanying rock movement could set it off, why hadn’t the earthquake occurred during larger blasts that had previously occurred at this or nearby quarries?

Although most blast experts would discount the potential for a quarry blast to result in an earthquake, many in the public and potentially the USGS, believe that the quarry blast was the earthquake. This would require one to believe that the response felt 200 km away was a quarry blast. A USGS geophysicist was quoted in the Mankato Free Press as stating that the raw seismological data indicated that the explosion caused the shaking and was quoted as stating “I would say it looks fairly blasty.” Of course, the obvious problem with this position is that one would have to explain why hundreds of other blasts within the region would not have triggered a similarly distant seismological response and the significant difference in energy between a magnitude 2.8 earthquake and a quarry blast that generated low ground vibration. In addition, the onsite monitors showed a clear reduction in the blast energy within

hundreds of metres, not hundreds of kilometres. In addition, the seismic signature of the quarry blast was shown by LCI to be demonstrably different (much higher frequency) than the signature observed by USGS.

6 CLAIMS AND RESOLUTION FROM LEGAL PERSPECTIVE

Within minutes of the earthquake, social media accounts were flooded with reports of buildings shaking and widespread property damage. As a result, city officials set up a phone number to report damage concerns and maintained a list of each resident who called, regardless of the nature of the complaint. By this time, overall suspicion and the majority of initial reports focused on the blast event at the quarry as the likely cause of the earthquake.

City officials suspended blasting operations and the blasting company immediately contacted its insurance company. Within 24 hours, the insurance company reached out to counsel for advice. Working with the blasting company, Reminger immediately contacted city officials and gained access to the list of the more than 50 residents who had reported damage concerns. Assuming an average of just \$20,000 per claim, we were facing an aggregate claim of potentially more than \$1,000,000. Additionally, at least one of the homeowners alleged the earthquake triggered a landslide behind his home, with more than \$100,000 in estimated repairs.

Counsel took a proactive approach to investigating and responding to all claims. Our first step was to convince city officials to allow us to actively manage the damage investigation. We did not want City engineers, or others without experience in identifying blast damage issuing damage assessments or causation opinions, since they likely lacked objectivity and the necessary experience. City officials were eager to turn the claims management and investigation over to experts, along with the list of residents who had expressed damage concerns. As legal counsel for the blasting company, our next step was sending letters to each resident asking for a written description of the alleged damage, along with photographs, and other proof of their claims. In our experience, when asked to take affirmative action to assert a claim, a number of people will decide not to pursue it further. This approach also separated residents who called because they were anxious, but who had not actually identified cosmetic or structural damage.

6.1 Damage evaluation

Of the approximately 50 letters initially received, about 35 responses from residents identified damage they believed was from the earthquake and were seeking compensation. Upon receipt of the responses, each homeowner was contacted to inform them that their claim would be evaluated by a qualified engineer, at no cost to them, and to set up appointments to inspect each property. This process resulted in a few more residents dropping their claims. At the time of inspections, 27 damage claims remained. Most claims were clustered within 0.5 kilometres (1,500 ft) of the quarry, with one outlier 1.5 km (1 mi) away. Within 120 days of the earthquake, the inspections were complete. Counsel also held interviews with the local authorities, who were considering criminal charges against the blaster who controlled the blasting permit for the quarry. Ultimately, no criminal charges were filed, and the blasting permit was reissued.

Of the 27 homes inspected, all but three showed signs of damage that obviously existed prior to the earthquake, which was another advantage of a quick response and investigation. Recent structural damage is relatively easy to identify, and often includes jagged edges to cracks, the lack of foreign material inside the crack, and dust and other material from inside the crack surrounding the area. By asking the homeowners for specific information during the inspections, including when they last painted areas where issues were present, evaluators were able to eliminate most damage complaints, since most of the cracks had paint in or over them. However, a delay of six months or more would have made it much more difficult to distinguish between a pre-existing and new crack. If the inspections occurred after the homeowners had performed repairs or repainted, a substantial portion of evidence would have been lost.

Based on the inspections, only three homes appeared to have recent damage. These homes all suffered full or partial chimney collapses. From an engineering perspective, this type of damage makes sense relative to the ground motion of an earthquake. Low frequency ground vibrations tend to result in resonance of low frequency structures such as chimneys, with upper structures more likely to suffer movement and resulting damage. The chimneys were likely already in poor condition and the average age of the houses which experienced chimney damage was at least 80 years. Figure 7 provides a view of one of the chimneys with loose brick visible on the shingles.

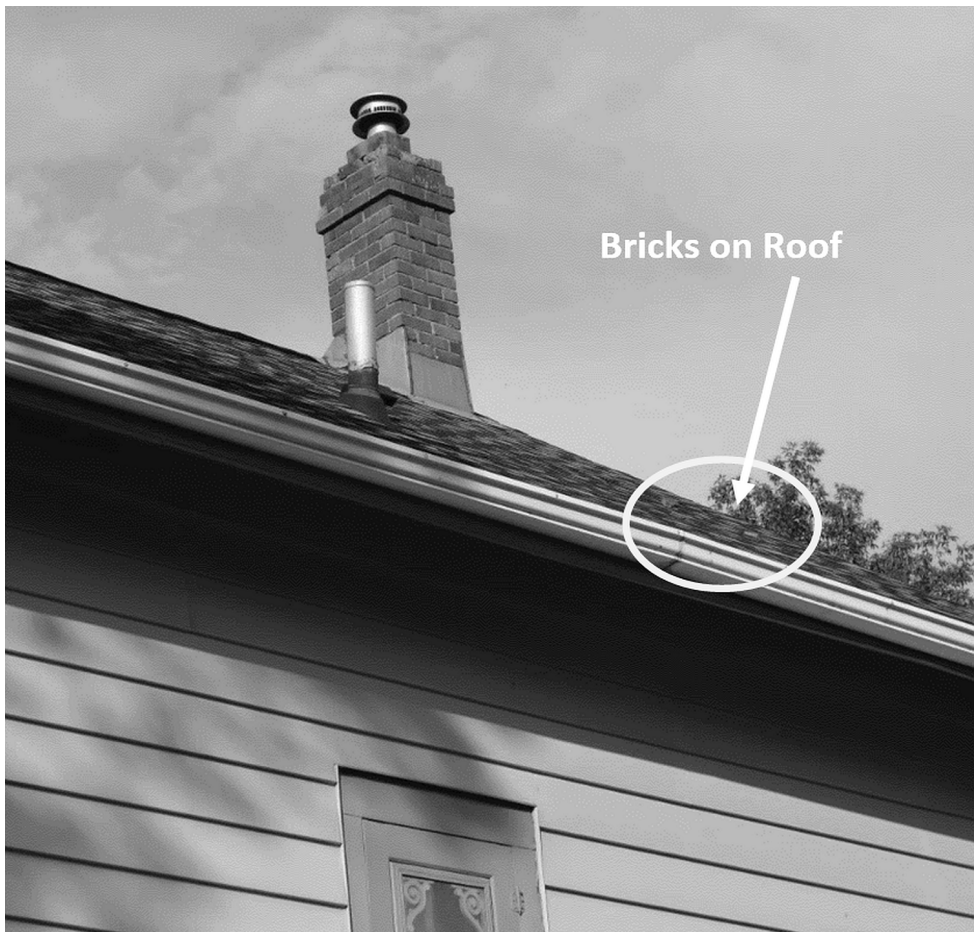


Figure 7. Chimney damage.

6.2 Claim settlement

The investigations were followed with written reports from the structural engineer to each homeowner, utilising photographs from the inspections to explain why the damage was not seismic-related. Having established how each claim was not consistent with vibration damage, the information from the engineer and the data from the seismology report concluded no causal relationship existed between the blast on April 25, 2017, and the earthquake that occurred the same day, but seconds later. Additionally, published USGS data that showed a magnitude 2.8 seismic event was unlikely to cause structural damage. Without admitting fault, the claims of the three homeowners who alleged damaged chimneys were able to be resolved for less than \$15,000 US Dollars. Although counsel agreed with the

conclusion that the earthquake was unrelated to the blast event, the motivation for settling the three chimney claims was to appease the local authorities with the goal of maintaining the blast permit for the quarry. As a result of the proactive investigation and response, all claims were settled quickly for a nominal amount, and the Quarry was able to maintain its blasting permit and eventually resume operation.

7 SIMILAR EVENTS

In research of this event, similar events have occurred where earthquakes were noted within close timing to a quarry blast.

7.1 *McCook, Illinois - 2013*

One identified was relatively recent in 2013 at the Federal Quarry in McCook, Illinois, USA.

A summary of the findings from the Illinois Department of Natural Resources Quarry Inspection summarises:

The Department initially responded to the reported seismic event on 11/4/2013 and conducted a blasting records and site inspection the following day. This inspection included a comprehensive review of all blasting and seismograph records, seismograph locations and a physical inspection of the quarry and blasting sites. This inspection revealed that all blasting activity at this site was conducted in accordance with the ground vibration requirements set forth within 62 Ill Admin. Code 300.225.

The operator monitors its blasting activities with four (4) permanently installed seismographs surrounding the quarry and supplements monitoring with an additional portable seismograph which it positions at the nearest protected structure to each blast. On 11/4/2013, these seismographs were positioned between 809-ft and 1,257-ft from the surface blast, and recorded two separate events. The first event occurred at approximately 12:39 P.M. and is attributed to the surface blast conducted at the quarry. The subsequent event, recorded approximately seven (7) seconds later, is of unknown origin. Again, analysis of the records and seismograph information indicates that the surface blast on 11/4/2013 was conducted in accordance with the applicable standards.

This earthquake was also indicated by the USGS to be a quarry blast as summarised from a report from the Chicago Tribune that day that read:

The blasting was strong enough to register 3.2 on seismographs. But the U.S. Geological Survey said the wave patterns do not match those from a quake. "Based on what they've looked at, we're pretty sure it's from a blast," said Paul Caruso, a geophysicist with the Survey. "It is not an earthquake." The Survey initially reported the magnitude as 3.7 and added it on a list of earthquakes. But it later reduced the magnitude to 3.2 and added: "Quarry blast."

Again, the ability to generate a magnitude 3.2 earthquake from a relatively small quarry blast is not possible from an energy standpoint. Very similar to the earthquake that occurred in Mankato, the lower frequency, higher energy earthquake occurred about 8 seconds after the quarry blast with the quarry blast showing unremarkable PPV for the blast.

7.2 Drummond island, Michigan – 2016

In Michigan, USA, in 2016, an earthquake was associated with a quarry blast at a limestone operation in a remote area of the Upper Peninsula near the US-Canada border. A report from the radio station 100.5 The River – Grand Rapids states:

It's been a couple of years since Michigan experienced an earthquake, but a mining explosion on Drummond Island came close. The explosion registered 2.7 on the Richter scale. The explosion at a dolomitic limestone mine on Drummond Island took place on June 28, 2016. The Drummond Island mining operation is run by Carmeuse Lime & Stone. I spoke with Ray LeClair, Carmeuse Lime & Stone's Director of Operations. He oversees the operations in the Great Lakes region including the Drummond Island operation. LeClair said the mining site on Drummond Island has been open since the late 1940s and after checking the report from June 28, 2016, they found "nothing abnormal about the report" and he was "not quite sure why it registered." LeClair said the blast was similar to others that they do on the island about ten times each year.

The 2.7 registered by the blast is smaller than the earthquakes felt in 2015 when two earthquakes were recorded in lower Michigan. An earthquake registered 4.2 in Galesburg on May 2 and a 3.3 was recorded near Battle Creek on June 30. It is not entirely unusual for a mining explosion in Michigan to set off USGS monitors. On February 16, 2015 a 2.5 was recorded from a mining explosion near Alpena. On January 12, 2015 a 2.3 was recorded near Negaunee in the Upper Peninsula.

7.3 Clintonville, Wisconsin – unrelated to blasting – 2012

In Clintonville, Wisconsin, USA, complaints of earthquakes over a five-day period in an area that is seismically inactive and not near a quarry were noted for several days in March of 2012. Over 300 complaints were made over the five-day period. Although much rarer than in seismically active areas, earthquakes do occur in seismically inactive areas. The occurrences tend to be obviously more infrequent and of lower average magnitude. With mining operations spread around the country, and blasting happening at hundreds of properties, the simple chance of an earthquake happening in close timing to a small blast cannot be simply ignored.

8 RECOMMENDATIONS

A prompt and thorough investigation was key to resolving the damage claims. Certainly, given the hysteria over the event, if we had delayed even six months, the outcome would have been drastically different. Another key effort was convincing city officials to allow us to take the lead in investigating the damage claims, rather than allowing a city housing inspector or someone with no damage investigation experience, much less blasting experience, to conduct the investigations. Individuals, even engineers, without blasting experience tend to be swayed by the general belief that blasting vibrations are highly likely to damage structures. We avoided that prejudice by using structural engineers with strong blasting experience. Additionally, by forcing concerned homeowners to actively identify and provide proof of their claims, we eliminated a significant number of complaints. The early response enabled us to mollify the hysteria by providing a source to direct homeowner concerns and establish trust, which enabled completion all the inspections within four months of the event.

Ultimately, the key to the successful resolution of this matter was to have an experienced team in place which allowed an immediately response. From the onset, the blasting company, insurance company, counsel and experts aggressively took the position that blast event did not cause the earthquake. But experience told us we needed to adopt an initially neutral stand and investigate each claim on its merits. Once the team was assembled, it was simply a matter of completing the investigation and finalising the reports.

In the case of the blast at the Jefferson Quarry in Mankato and the Federal Quarry in McCook, the operations would have benefitted from monitoring vibrations for a longer period of time after the blast occurred to clearly demonstrate the ground motions from the blast and the separate earthquake. Modern seismographs allow for recording times of relatively long duration, and it would benefit from recording at least 20 to 30 seconds after each blast to document any subsequent seismic events.

9 CONCLUSIONS

Our analyses strongly indicate that the seismic event recorded and located by the USGS on 25 April 2017 at 11:02 CDT was an earthquake and not a blast at the Jefferson Quarry that occurred about 7 sec earlier. The precise location of the earthquake is uncertain because of the lack of

close-in seismic stations but it appears that it occurred to the south of the quarry by a few kilometres at a depth typical of earthquakes in the central U.S. Examination of the records of the earthquake and felt reports indicate that it was the earthquake that was felt by the local population and not the blast. As recorded by seismographs around the Jefferson Quarry, the blast was too small to be felt at distances outside the immediate vicinity of the quarry. This earthquake occurred at a similar magnitude and occurred at a similar time to the earthquake that was observed in McCook, Illinois in 2013.

The relationship between the blast and the earthquake is unknown. If the earthquake was located at depth and a few kilometres south of the Jefferson Quarry, we believe it is unlikely that there is a cause-and-effect relationship. In our judgement, the size of the blast would be too small to trigger an earthquake even on a critically stressed fault.

Should a similar situation arise where an earthquake occurs within close timing of a small blast, Important takeaways include being proactive in addressing concerns, claims, and complaints and being transparent with respect to what is known and unknown regarding cause and effect. One of the unfortunate gaps in the data was that the on-site seismometers were set to shut off 5 seconds after blasting. Had they run only 20 seconds longer, we would have had a much more complete picture of the differences between the quarry blast and potentially a more accurate location of the epicentre with clear separation of the quarry blast from the earthquake.

REFERENCES

- Mankato Earthquake Investigation Report - Regional Seismic Event on April 25, 2017, June 14, 2017, Barr Engineering Company.
- Braile, L.W., Hinze, W.J., von Frese, R.R.B. & Randy Keller, G. 1989. Seismic properties of the crust and uppermost mantle of the conterminous United States and adjacent Canada. *Geophysical Framework of the Continental United States, Chapter 28.*, edited by L. C. Pakiser; Walter D. Mooney, Geol. Soc. Of Am., Boulder, Colo.
- Chandler, V.W. 1991. Aeromagnetic anomaly map of Minnesota, *State Map Series S-17*, University of Minnesota, Minnesota Geological Survey.
- Chandler, V.W. 2020 & 2014. Minnesota at a Glance Earthquakes in Minnesota, *University of Minnesota, Minnesota Geological Survey.*

Persistent link at: Minnesota at a Glance Earthquakes in Minnesota (umn.edu).

Klein, F. 2014. User's guide to HYPOINVERSE – 2000, a Fortran program to solve for earthquake locations and magnitudes, version 1.40, *U.S. Geological Survey Open-File Report 02-171* revised June 2014.

Mooney, H.M. 1979. Earthquake history of Minnesota, *RI-13, University of Minnesota*, 20 p.

Mooney, H.M. 1979. Earthquake history of Minnesota, *Minnesota Geological Survey Report of Investigations 23*, 20 p.

Runkel, A.C., Meyer, G.N. & Lusardi, B.A. 2011. C-26 *Geologic Atlas of Blue Earth County, Minnesota [Part A]*. University of Minnesota, Minnesota Geological Survey.

USGS (June 12, 2017), M 2-8 Quarry Blast – 2 km N of Mankato, Minnesota. *Webpage & Data Archive, including community reports located at: "https://earthquake.usgs.gov/earthquakes/eventpage/us10008kr5#executive"*.

<https://www.chicagotribune.com/news/breaking/chipolice-tremors-in-western-suburbs-from-quarry-blast-20131104-story.html>

Report: Earthquake, not blasting to blame for April shake | Local News | mankatofreepress.com

<https://abc7chicago.com/archive/9313036/>

<https://www.reuters.com/article/us-booms-wisconsin/wisconsin-town-haunted-by-booms-traces-noise-to-small-quakes-idUSBRE82M11J20120323>

<https://rivergrandrapids.com/mining-explosion-on-drummond-island-registers-2-7-on-richter-scale/>

<https://cse.umn.edu/mgs/earthquakes>

New approaches for evaluating building response to blast vibrations

M.I. Álvarez-Fernández, M.B. Prendes-Gero, L. Conde-Fernández
& C. González-Nicieza

Rock Dynamics Research Group, University of Oviedo, Asturias, Spain

ABSTRACT: Artificial intelligence techniques and numerical simulations are employed to analyse the response of a structure to the dynamic effects of a blast. As artificial intelligence techniques, a neural network is used because it is one of the simplest techniques to apply. As numerical models, the finite differences are employed. Both techniques are applied in a real case, a scale building built in the vicinity of an open-pit mine, with the end of comparing the advantages and disadvantages of the techniques. During the tests, the real response of the building is monitored using accelerometers located in different elements of its structure. The results show that the neural network allows to obtain a reliable and simple predictive tool capable of characterising the behaviour of the building. The numerical simulation, although more complex, allows to analyse the behaviour of the structure and determine its weak points.

1 INTRODUCTION

The increasing development of open pit mining, driven by the growing demand for minerals, has contributed to an increase in the use of blasting explosives. To this day, explosives are the most efficient source of energy for breaking and excavating rock. When an explosive detonates inside a blasthole, it instantly releases a large amount of energy in the form of pressure and temperature. However, only a small portion of this energy is used to break the rock, so the remaining explosive energy is wasted in producing unwanted effects such as vibrations, noise, subsequent breakage, airwave propagation, etc.

Ground vibration is literally a wave motion that propagates from the point of detonation in the same way as the wave created by a stone falling into a pond. When the vibration wave passes through structures on the ground surface, it transmits the vibration to those ones. These vibrations can cause the affected structures to

resonate if the ground vibration frequency matches the natural frequency of the structure and, because of this, the amplitude of the vibration can grow and become larger than the inducing vibration.

Frequency (F) and peak particle velocity (PPV) are the two most commonly used parameters for measuring ground vibration. Some authors highlight the importance of frequency because the structural response depends on the frequency of ground vibration. This vibration is influenced by a large number of parameters such as the physical and mechanical properties of the rock mass, the characteristics of the explosive used and the blast design itself. Furthermore, this vibration is a complex combination of different wave types (Brinkmann 1987). In general, variables such as acceleration and velocity of a point over time are used to describe it, together with the frequency and propagation velocity of the wave (Bender 2006).

However, once the wave reaches a structure, not only the intensity, frequency or duration of the wave must be taken into account to establish its

safety, but also other variables directly related to it, such as its damping coefficient or its natural frequency.

Although there are numerous studies related to dynamic behaviour and damage in structures (Faramarzi *et al.* 2014, Dogan *et al.* 2013, Dowding 1996, González-Nicieza *et al.* 2014), the major drawback is that each country has its own standards without consensus between them. In general, it can be said that in most standards the PPV or maximum velocity at which a particle moves due to the effect of a wave is the parameter that reflects the intensity of the wave, although some consider its maximum value and others the modulus of the velocity vector. Other standards consider the frequency of vibration as a determining factor, although in a simplistic way, without taking into account that the different elements of a structure have different natural frequencies (Dowding 1980, Medearis 1996). There is a second damage criterion based on energy, either taking into account the acceleration peak and the frequency at that peak (Crandell 1949), or expressed in terms of velocity (Nicholls *et al.* 1971). More recently, it has become necessary to take into account the energy carried by the wave at the characteristic frequency of the structure, which can be calculated either from the energy spectrum (Guosheng *et al.* 2011), or from the waveform captured with geophones (Chandar & Sastry 2015).

In recent years, the research has focused on analysing the effect that an explosion can have on both civilian and military buildings. To this end, equipment capable of simulating explosions has been designed, such as the so-called shock tubes (Schleyer *et al.* 2007, Haris *et al.* 2018, Poulin 2018, Lacroix & Doudak 2018), blast pendulum systems (McDonald *et al.* 2018, Jing *et al.* 2014) or blast simulator (Stewart *et al.* 2014, Rodriguez-Nikl *et al.* 2011) among others. However, the most realistic representation of blast loading can be obtained only with full-scale field tests which best mimic real-life situations (Draganić *et al.* 2018). Although, the blast experimentation is usually conducted on scaled samples what reduces the need for large explosive quantities and consequently lowers the overall danger of injury.

However, these tests are limited due to security restrictions and a lack of the considerable resources required. Therefore, numerical modelling and simulation have been proven to be a valuable tool in simulating the behaviour of structures under blast loading. Although blast

phenomena can be difficult to model, because of the large number of variations in parameters which describe material models, finite element types and sizes, and boundary conditions and explosive loading, numerical models can be used to predict structural behaviour with fairly good accuracy in comparison to experimental tests (Ivančo *et al.* 2019, Draganić & Varevac 2018).

In recent years, a rapidly emerging approach in this area focuses on using neural networks, machine learning algorithms, and neural fuzzy to predict, simulate, and optimise blasts. The results of these studies show the artificial intelligence as a powerful tool that can solve problems in diverse and effective ways. Applications of ANNs include predicting blast-induced ground vibrations (Khandelwal & Singh 2009, Shahri & Asheghi 2018, Das *et al.* 2018, Álvarez-Vigil *et al.* 2012), quantification of blast loading on a building behind a blast wall (Remennikov & Rose 2007) or along simple city streets (Remennikov & Mendis 2006). More recently, neural networks have been applied to do prediction of blast loading in internal environment (Dennis, *et al.* 2021). However, the limitations of predictive models developed by the ANN technique lie in the narrow scale of application since it is designed under the conditions and properties of a specific area and cannot apply widely in other sites (Al-Bakri & Sazid 2021).

In this work full-scale field tests have been done with the end of developing a neuronal network as a predictive tool and carrying out numerical simulations to analyse the behaviour of the structure and determine its weak points. The end is to know the variation of the values of the different parameters that characterise one wave, once this wave has gone through the structure (going into it by the foundations and going out by the beams of the roof). The analysed variables have been the acceleration, velocity, frequency and duration in the three axes (X, Y, Z) and the energy.

2 LOCATION AND CASE OF STUDY

An operational open-pit mine is chosen for the tests. In this mine, blasting is carried out constantly and, therefore, it is possible to carry out a continuous study over time. The mine is located in Santa Marina of Piedramuelle near the city of Oviedo, capital of the Principality of Asturias in Northern Spain. In its square a 2 m high concrete structure with a base of 2.5 x 2.5 m was built on a spread foundation (Figure 1).



Figure 1. Process of construction of the real-scale structure.

3 METHODOLOGY

Once the structure is built:

- The structural elements to be measured are defined
- Accelerometers type Syscom, Etna, 9043, 5033, are installed and the maximum acceleration, is recorded
- The neural network is developed
- The numerical simulation is implemented

3.1 Definition of the elements

Measurements are made on two structural elements at the bottom of the structure where the input parameters are recorded and on two structural elements at the top where the output parameters are recorded:

- NLB: North lower beam
- NUB: North upper beam
- SUB: South upper beam

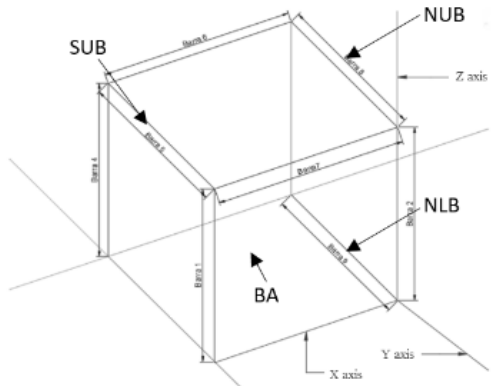


Figure 2. Structure and nomenclature of the beams.

Table 1. Maximum acceleration collected for each axis.

Date	Ele.	Ax (mm/s ²)	Ay (mm/s ²)	Az (mm/s ²)	Ele.	Ax (mm/s ²)	Ay (mm/s ²)	Az (mm/s ²)
20/03/19	BA	14.41	20.09	12.83	NUB	49.63	74.95	74.9
26/03/19	BA	16.03	29.08	17.85	SUB	48.73	92.52	41.97
16/04/19	BA	37.7	67.26	113.9	NUB	67.73	52.73	29.85
06/05/19	BA	169.49	191.49	422.18	NUB	71.85	54.94	35.28
15/05/19	BA	46.01	60.26	25.19	SUB	137.68	214.21	78.79

Table 2. FFT for each axis.

Date	Ele.	FFTx (Hz)	FFTy (Hz)	FFTz (Hz)	Ele.	FFTx (Hz)	FFTy (Hz)	FFTz (Hz)
20/03/19	BA	11.71	11.42	12.3	NUB	19.53	20.5	93.99
26/03/19	BA	42.72	28.02	20.01	SUB	19.53	20.26	93.5
16/04/19	BA	7.81	16.79	30.85	NUB	20.38	0.24	0.73
06/05/19	BA	8.05	8.05	23.92	NUB	20.01	0.97	0.49
15/05/19	BA	16.3	16.45	32.27	SUB	0.48	0.48	0.49

– BA: Base or structure slab

3.2 Installation of the accelerometers

Once the elements are defined, and the accelerometers are placed on them, controlled blasting is carried out. At this point, it should be noted that due to the pandemic, blasting is stopped for a period of 1 year.

With the exception of the accelerometer SYSCOM 3 that records the velocity, the rest of them record for each axis and each element the maximum acceleration (Table 1), while the velocity is obtained indirectly through the integration of acceleration, and the energy is calculated as the sum of the squares of the velocity components.

To obtain the Fast Fourier Transform (FFT) (Table 2), a MATLAB algorithm is used to calculate the dominant frequency from the recorded waveform. In addition, the value obtained is compared with the one obtained with the SismoSignal software that treats seismic signals coming from earthquake-type events. The

objectives are:

- Determine the FFT and compare it with the one obtained in MATLAB verifying the implemented algorithm
- Determine the event duration (Table 3) by the significant duration or interval in seconds, between 5% and 95% of the Husid function, where most of the energy is concentrated (Trifunac & Brady 1975, Husid 1973)

3.3 Development of the neural network

It is used a feedforward backpropagation (FFBP) network as the most suitable model for resolving an identification problem. In a neural network, the numbers of neurons and layers can be the difference between success and failure. To choose the number of hidden neurons the geometric pyramid rule is employed (Masters 1993), where the number of neurons follows a pyramid shape. First, one must set the number of neurons in the input layer i and the number of neurons in the output layer o . Table 4 lists several equations

Table 3. Event duration for each axis.

Date	Ele.	tx (s)	ty (s)	tz (s)	Ele.	tx (s)	ty (s)	tz (s)
20/03/19	BA	1.48	1.2	1.73	NUB	1.37	1.75	1.54
26/03/19	BA	0.19	0.18	0.13	SUB	1.12	1.51	0.97
16/04/19	BA	0.38	0.14	0.07	NUB	2.15	2.74	2.10
06/05/19	BA	0.33	0.27	0.14	NUB	1.91	2.82	2.69
15/05/19	BA	0.66	0.57	0.60	SUB	1.98	2.19	2.37

associated with the calculus of the hidden layer neurons for one hidden layer h_1 and two hidden layers h_2 , while Table 5 summarises the architecture of the neural network, initially employed.

Table 4. Computation of the number of hidden layer neurons using the geometric pyramid rule.

Hidden	Geometric pyramid rule layers		
1	$r = \sqrt{i \times o}$	$h_1 = r$	
2	$r = \sqrt[3]{i/o}$	$h_1 = o \times r^2$	$h_2 = o \times r$

3.4 Implementation of the numerical simulation

In addition to the neural network as a predictive tool, the application of numerical computation techniques has been explored, using FLAC3D, v.7.00, from Itasca Group Consulting. With this end, a geometric model of the analysed structure has been developed and available measurement campaigns have been used to calibrate the parameters of this model (Figure 3).

Once the structure has been modelled, a real

vibration wave corresponding to a blast is applied to its base and the theoretical response is recorded in the different elements (foundations, beams, columns, etc.) to compare them with the real measured records.

Table 5. Neural network architecture.

No. of input neurons	13
No. of output neurons	13
No. of hidden layers	1
No. of hidden neurons	13
No. of training cycles	100
Training data items	70%
Validation items	15%
Test items	15%

Figure 4 shows the vertical component of the acceleration measured at the base and used as input to the model, with a maximum value of 2.52 cm/s^2 , together with the response recorded at one of the beams, whose maximum value is 6.4 cm/s^2 in the simulation, very similar to the 7.8 cm/s^2 obtained in reality.

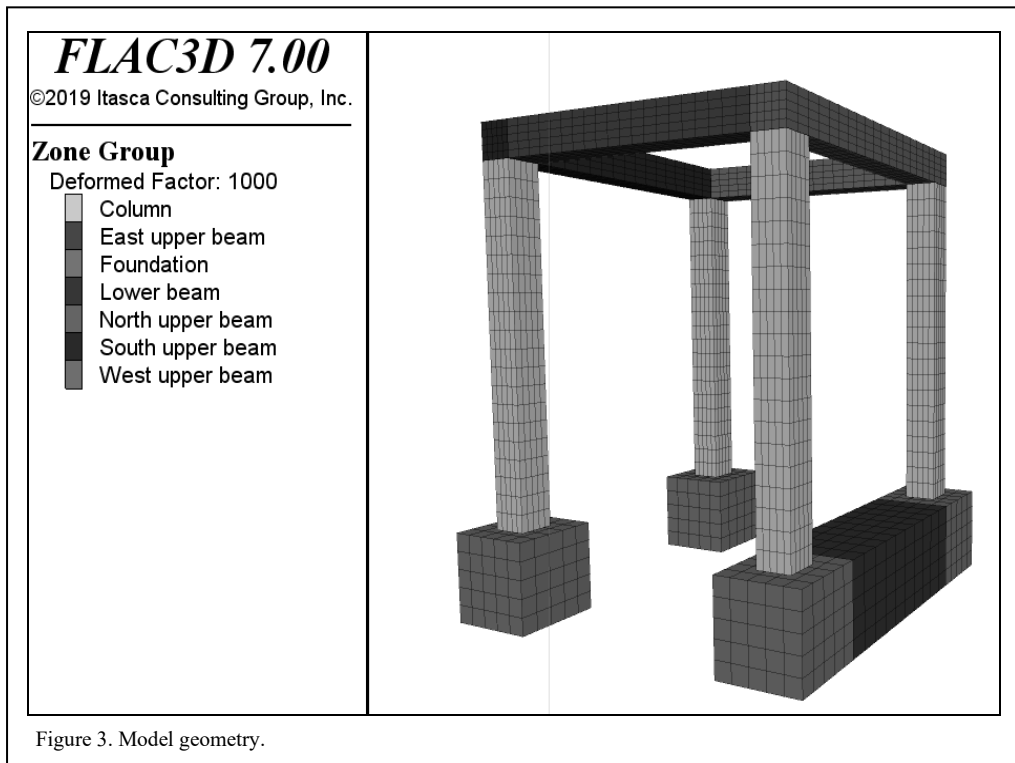
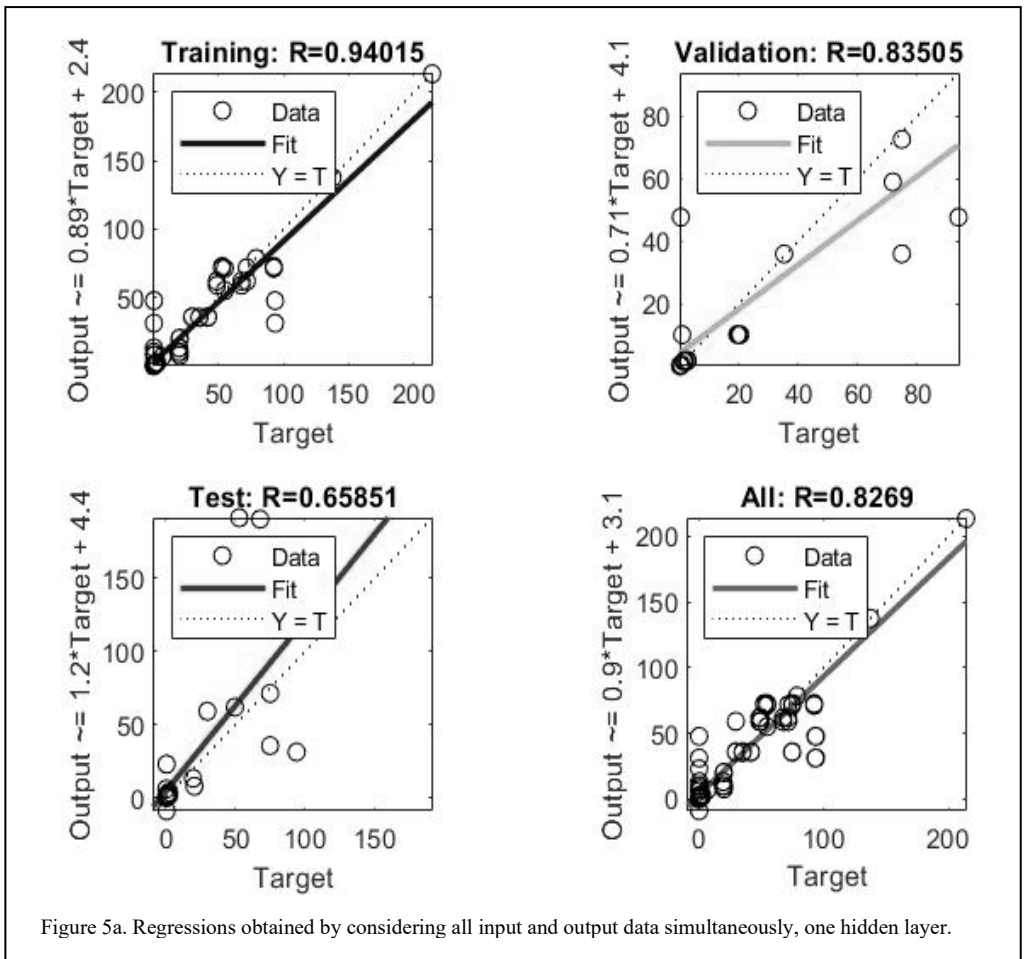
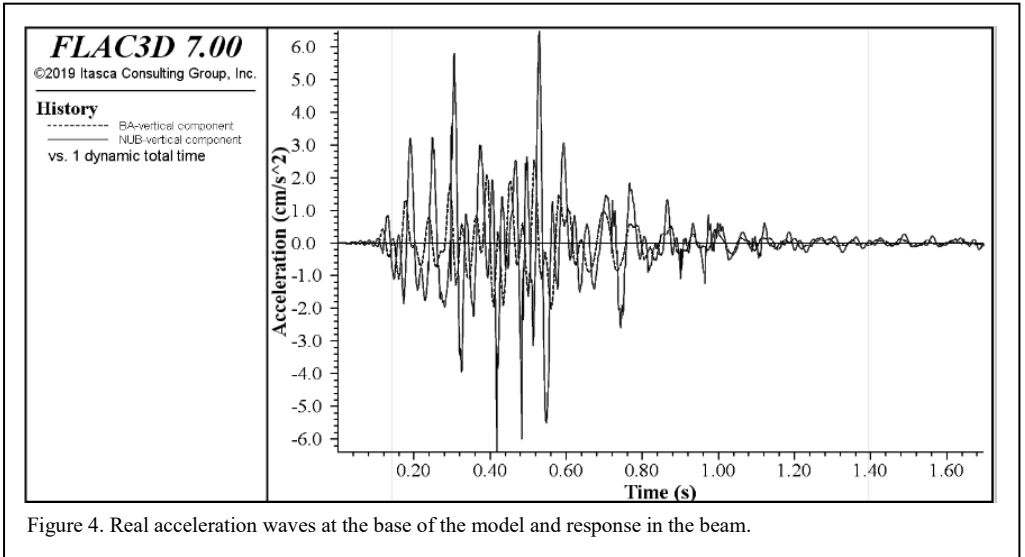
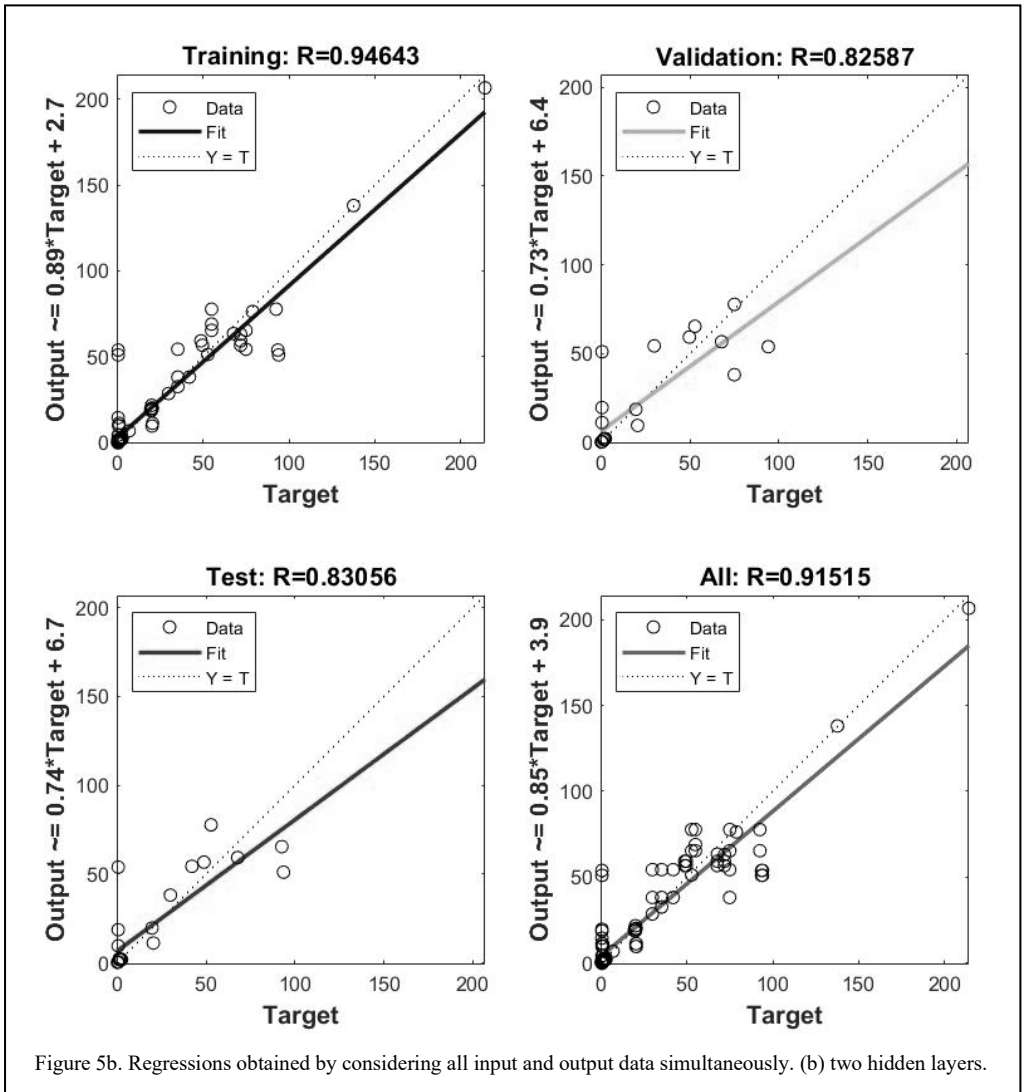


Figure 3. Model geometry.





4 DISCUSSION

4.1 Neural network

The calculation of the neural network with all input and output data, i.e. considering all axes at the same time and one hidden layer, show regressions over 0.94 for the training data items but they drop to 0.65 for the test items (Figure 5a). To improve these results, it was considered to work with two hidden layers with the same number of neurons in them and equal to 13. In this case, the results of the regression improve (Figure 5b), but the mean squared error presents very high values, so the calculation of different neural

networks for each axis with one and two hidden layers of 5 neurons in them were analysed.

On the X-axis, there is hardly any difference in the results obtained when one or two hidden layers are used, so as it is less computationally expensive, it is decided to work with the simplest network with regressions close to 0.9 (Figure 6) and a value of 0.06 for the mean square error.

On the Y-axis, the regression coefficient values, for a neural network with one hidden layer, are very high (Figure 7), and the mean square error is equal to 0.09.

On the Z axis, both the value of the regression coefficient and the value of the mean squared error is lower with two hidden layers decreasing from

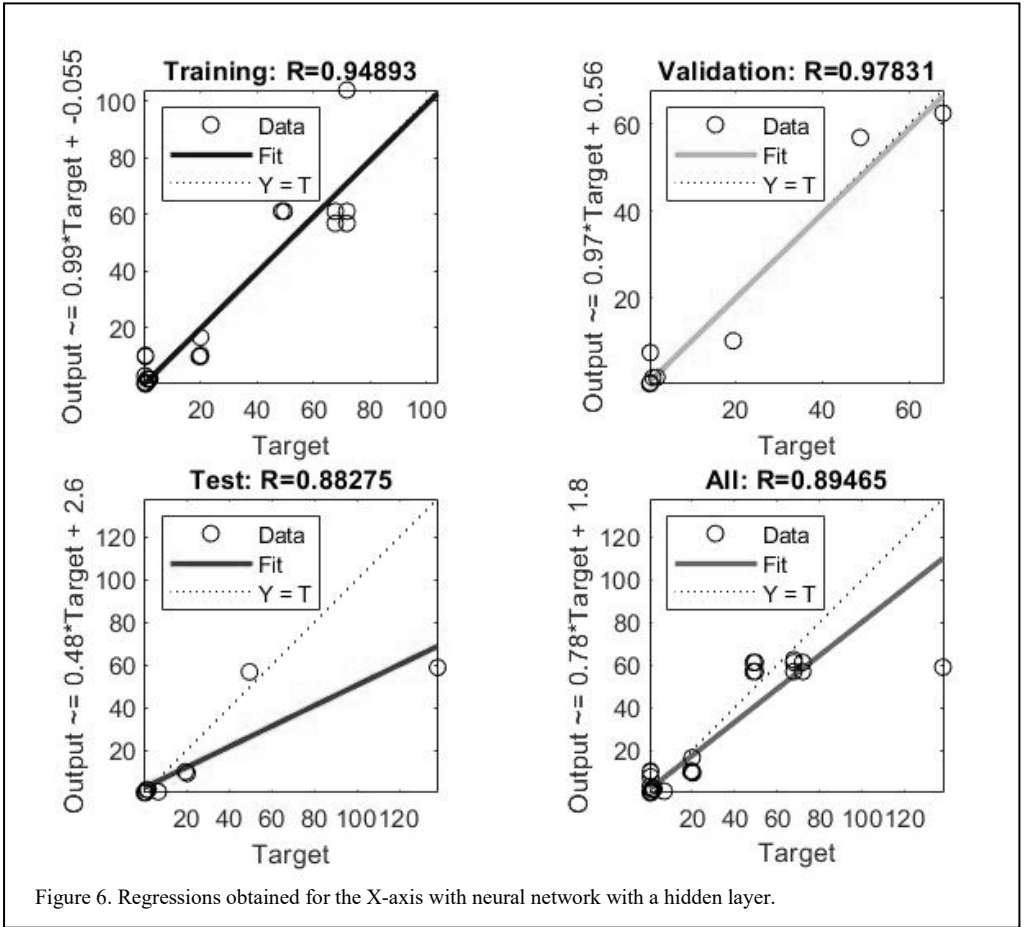


Figure 6. Regressions obtained for the X-axis with neural network with a hidden layer.

0.16 for one hidden layer to 0.05 for two hidden layers. In any case the value of the regression is very low for the validation data items and test data items (Figure 8).

4.2 Numerical simulation

The analysis of the models shows the influence of wave superposition and amplification of ground vibration, detecting situations of damping or amplification depending on the characteristics of the structure and the different elements.

On the other hand, the occurrence of unexpected natural frequencies in the structure can be observed and their predominance varies from one element to another. Thus, the dominant frequency for the spread foundation would be 14.4 Hz, while for the beams it would reach 48.6 Hz.

Figure 9 represents, on the deformed geometry of the structure, the vertical displacements (Figure

9a) and the deformations (figure 9b) in different phases of the calculation with a deformation increased 100 times.

5 CONCLUSIONS

The study shows that:

- One net should be used for each axis.
- The results of the neural network are not as expected, but the low volume of data available has to be taken into account. Therefore, a large improvement of the results can be expected when the training dataset is extended. Besides, a larger volume of data will allow better filtering of the data, enabling the elimination of outliers. This is expected to be done when the current situation stabilises.
- The numerical simulation has shown different situations that the neural network has not been detected as the damping or amplification

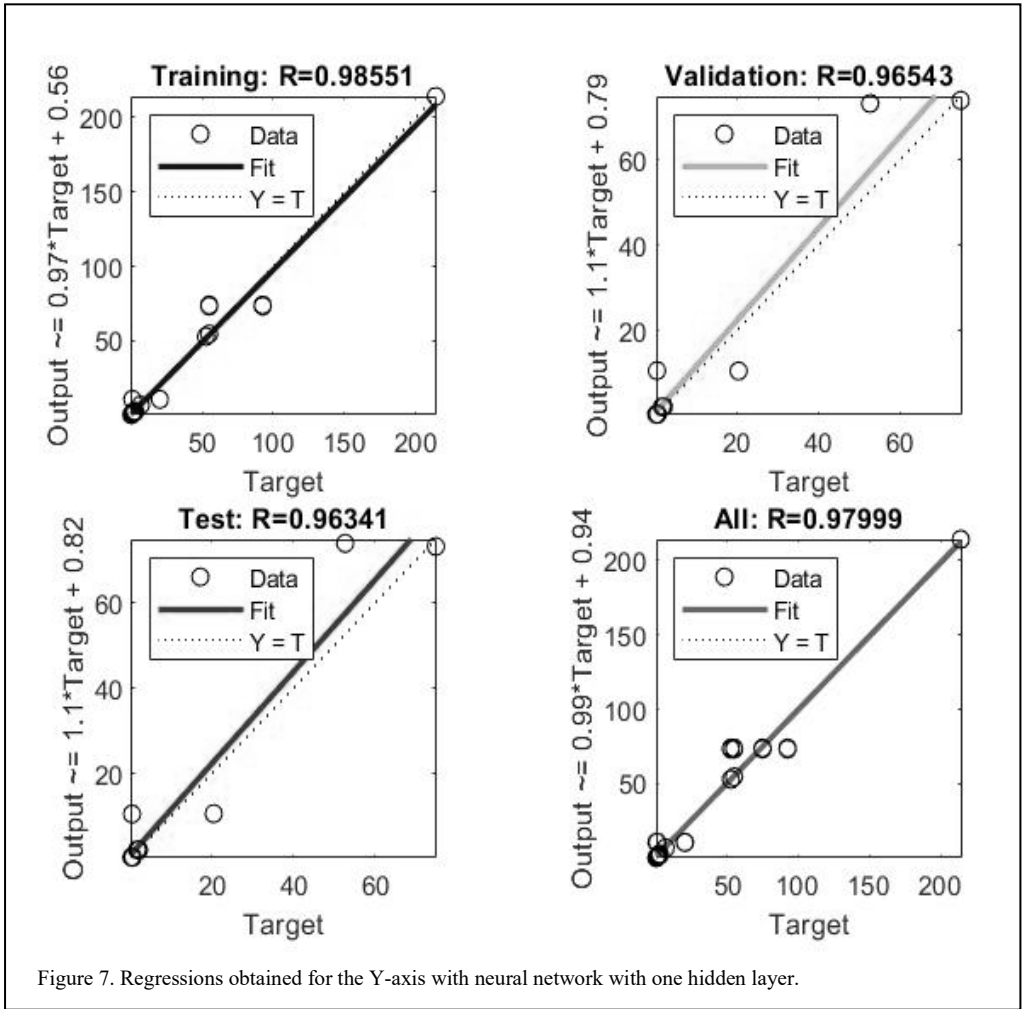


Figure 7. Regressions obtained for the Y-axis with neural network with one hidden layer.

of the vibration due to the superposition and amplification of ground vibration, and the unexpected natural frequencies of the elements.

6 ACKNOWLEDGMENTS

The authors acknowledge the financial support provided by the Spanish Ministry of Economy and Competitiveness through the following ‘Explora Project’ BIA2015-72928-EXP.

REFERENCES

- Al-Bakri, A.Y. & Sazid, M. 2021. Application of artificial neural network (ANN) for prediction and optimisation of blast-induced impacts. *Mining*, 1, 315-324.
- Álvarez-Vigil, A.E., González-Nicieza, C., López-Gayarre, F. & Álvarez-Fernández, M.I. 2012. Predicting blasting propagation velocity and vibration frequency using artificial neural network. *International Journal of Rock Mechanics and Mining Sciences*, 55, 108-116.
- Bender, W.L. 2006. Understanding blast vibration and airblast, their causes, and their damage potential. Spring 2006 and Fall 2007 workshops of the Golden West Chapter of the International Society of Explosives Engineers.
- Brinkmann, J.R. 1987. The control of ground vibration from colliery blasting during the undermining of residential areas. *Journal of the South African Institute of Mining and Metallurgy*, 87(2), 53-61.

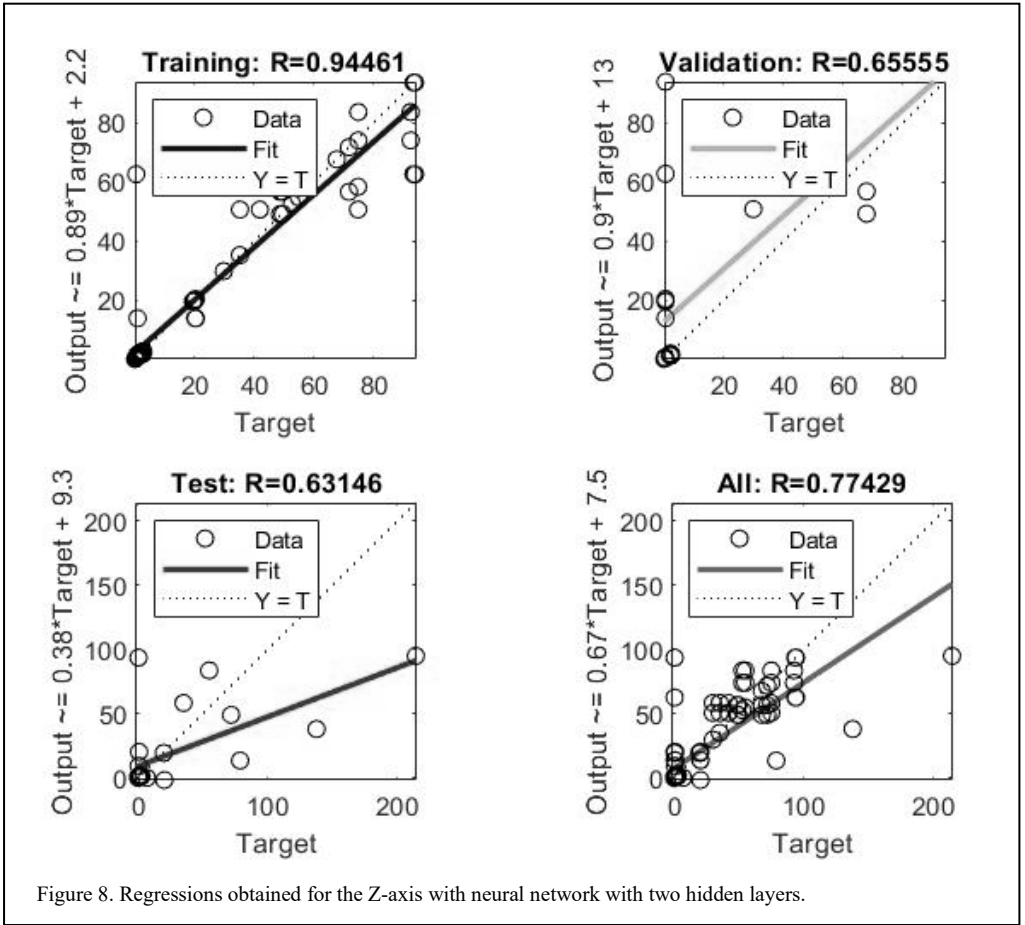


Figure 8. Regressions obtained for the Z-axis with neural network with two hidden layers.

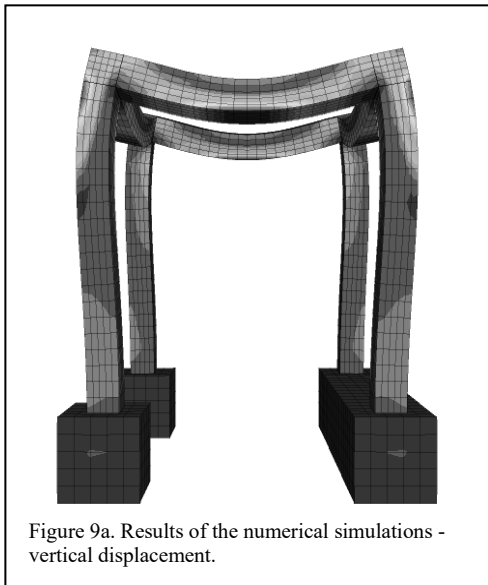


Figure 9a. Results of the numerical simulations - vertical displacement.

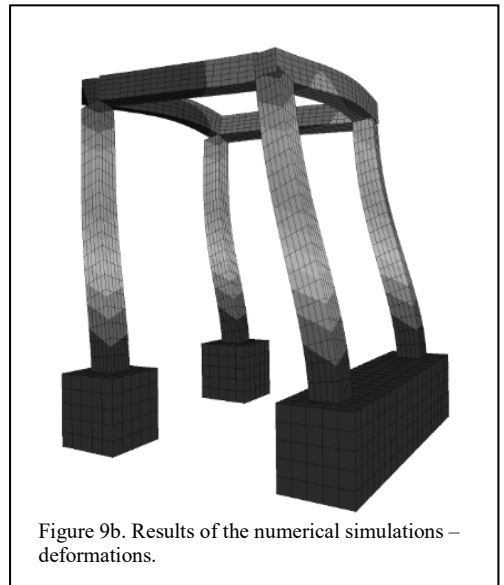


Figure 9b. Results of the numerical simulations - deformations.

- Chandar, K.R. & Sastry, V.R. 2015. A new method of estimating wave energy from ground vibrations. *Geomaterials*, 5, 45-55.
- Crandell, F.J. 1949. Ground vibration due to blasting and its effect upon structures. *Journal Boston Soc. Civ. Engrs*, 222-245.
- Das, A., Sinha, S. & Ganguly, S. 2018. Development of a blast-induced vibration prediction model using an artificial neural network. *The Journal of the Southern African Institute of Mining and Metallurgy*, 119. 187-200.
- Dennis, A.A., Pannell, J.J., Smyl, D.J. & Rigby, S.E. 2021. Prediction of blast loading in an internal environment using artificial neural networks. *International Journal of Protective Structures*, 12(3), 287-314.
- Dogan, O., Anil, O., Akbas, S.O., Kantar, E. & Erdem, R.T. 2013. Evaluation of blast induced ground vibration effects in a new residential zone. *Soil Dynamic Earthquake Engineering*, 50, 168–81.
- Dowding, C.H., Beck, W.K. & Atmatzidis, D.K. 1980. Blast vibration implications of cyclic shear behaviour of model plaster panels. *Geotechnical Testing Journal*, 3(2).
- Dowding, C.H. 1996. Construction vibrations. *Prentice-Hall*, Englewood Cliffs.
- Draganić, H., Varevac, D. & Lukić, S. 2018. An overview of methods for blast load testing and devices for pressure measurement. *Advances in Civil Engineering*, 3780482.
- Draganić, H. & Varevac, D. 2018. Analysis of blast wave parameters depending on air mesh size. *Shock and Vibration*, 3157457.
- Faramarzi, F., Ebrahimi, F., Mohammad, A. & Mansouri, H. 2014. Simultaneous investigation of blast induced ground vibration and airblast effects on safety level of structures and human in surface blasting. *International Journal of Mining Science and Technology*, 24, 663–669.
- González-Nicieza, C., Álvarez-Fernandez, M.I., Alvarez-Vigil, A.E., Arias-Prieto, D., López-Gayarre, F. & Ramos-Lopez, F.L. 2014. Influence of depth and geological structure on the transmission of blast vibrations. *Bulletin of Engineering Geology and Environmental*, 73(4), 1211-1223.
- Guosheng, Z., Jiang, L. & Kui, Z. 2011. Structural safety criteria for blasting vibration based on wavelet packet energy spectra. *Mining Science and Technology (China)*, 21, 35-40.
- Haris, A., Lee, H.P. & Tan, V.B.C. 2018. An experimental study on shock wave mitigation capability of polyurea and shear thickening fluid based suspension pads. *Defence Technology*, 14(1), 12–18.
- Husid, R. 1973. Terremotos. *Andrés Bello*, Santiago de Chile.
- Ivančo, M., Erdélyiová, R. & Figuli, L. 2019. Simulation of detonation and blast waves propagation. *Transportation Research Procedia*, 40, 1356-1363.
- Jing, L., Wang, Z., Shim, V. & Zhao, L. 2014. An experimental study of the dynamic response of cylindrical sandwich shells with metallic foam cores subjected to blast loading. *International Journal of Impact Engineering*, 71, 60–72.
- Khandelwal, M. & Singh, T.N. 2009. Prediction of blast-induced ground vibration using artificial neural network. *International Journal of Rock Mechanics & Mining Sciences*, 46, 1214-1222.
- Lacroix, D.N. & Doudak, G. 2018. Experimental and analytical investigation of FRP retrofitted glued-laminated beams subjected to simulated blast loading. *Journal of Structural Engineering*, 144(7).
- Masters, T. 1993. Practical neural network recipes in C++, Morgan Kaufmann: Massachusetts, MA, USA.
- McDonald, B., Bornstein, H., Langdon, G.S., Curry, R., Daliri, A. & Orifici, A.C. 2018. Experimental response of high strength steels to localised blast loading. *International Journal of Impact Engineering*, 115, 106–119.
- Medearis, K. 1996. The development of rational damage criteria for low-rise structures subjected to blasting vibrations. *Kenneth Medearis Associates*, Final Rept. to National Crushed Stone Assn., August 1976, Washington, DC. p. 93.
- Nicholls, H.R., Johnson, C.F. & Duvall, W. 1971. Blasting vibrations and their effects on structures. *V.S. Bureau of Mines, Bulletin*, 656.
- Poulin, M., Viau, C., Lacroix, D.N. & Doudak, G. 2018. Experimental and analytical investigation of cross-laminated timber panels subjected to out-of-plane blast loads. *Journal of Structural Engineering*, 144(2).

- Remennikov, A.M. & Mendis, P.A. 2006. Prediction of airblast loads in complex environments using artificial neural networks. *WIT Transactions on the Built Environment*, 87, 269–278.
- Remennikov, A.M. & Rose, T.A. 2007. Predicting the effectiveness of blast wall barriers using neural networks. *International Journal of Impact Engineering*, 34(12), 1907–1923.
- Rodriguez-Nikl, T., Hegemier, G. & Seible, F. 2011. Blast simulator testing of structures: methodology and validation. *Shock and vibration*, 18(4), 579–592.
- Schleyer, G., Lowak, M., Polcyn, M. & Langdon, G. 2007. Experimental investigation of blast wall panels under shock pressure loading. *International Journal of Impact Engineering*, 34(6), 1095–1118.
- Shahri, A.A. & Asheghi, R. 2018. Optimised developed artificial neural network-based models to predict the blast-induced ground vibration. *Innovative Infrastructure Solutions*, 3(1).
- Stewart, L.K., Freidenberg, A. & Rodriguez-Nikl, T. 2014. Methodology and validation for blast and shock testing of structures using high-speed hydraulic actuators. *Engineering Structures*, 70, 168–180.
- Trifunac, M.D. & Brady, A.G. 1975. A study on the duration of strong earthquake ground motion. *Bulletin of the Seismological Society of America*, 65 (3), 581-626.

Proposed methodology to reduce microfractures in working stopes utilising vibration modelling

N. Valencia

Ecole Centrale Nantes, Nantes, France

ABSTRACT: This article proposes a method that avoids the generation of microfractures caused by vibrations in working stopes in granodiorite rock with the purpose of predicting the damages generated by blasting operation at Consorcio Minero Horizonte mine in Parcoy, Peru. In order to evaluate the microfractures impact at the working stopes, ramps, etc. two methodologies were followed: Firstly, the algorithm based on finite element method in Matlab language for time discretisation and nodal variables (modelling of ultrasonic waves) and Secondly, the interpolation analysis to determine vibration levels (far and near field Devine's model). Final results: Shotcrete consumption reduction from 174.117 to 157 m³/month in July and September 2017 respectively; reduction of length microfractures from 25 to 23 mm per month on excavation of 15.6 to 12% and reduction of the dilution from 25% to 12%.

1 INTRODUCTION

A usual problem presented in the mining industry is to recognise the orientation and density of fractures generated by blasting in the mineral deposits: from the knowledge of this parameter one can identify the level of damages generated by the explosives (density of the explosive, VOD and drilling diameter) in the contours of the excavation. In addition, it is possible to evaluate and avoid the risks of accidents by rock falling and establishing parameters to optimise the design of excavation, improve the granulometry and the damages control on the rock mass.

From this operational problem, the microfractures after the blasting, has led us to carry out a study of vibrations to set up the influence of the damages on the last limit of the excavation by deviation and overload, applying Devine Far Field modelling.

Two teams were used Minimate Blaster and Minimate Plus seismographs with current calibration. The vibration measurement program

by blasting aims to establish the behaviour of the vibration produced by blasting (attenuation law) for a type of rock and by the BDI (Blast Damage Index) and thus estimate the damage, taking as a parameter the fracturing critical velocity of rock in working stopes.

2 PROCESS OF THE PROPOSED METHODOLOGY

The present study was developed in the mining company Auriferous that has its mining activities in an area of 25,000 hectares (61,776.345 ac). This operation is carried out entirely within the Pataz Batholith, District of Parcoy, La Libertad Region, Peru. It is estimated more than 80,000 m (262,467.19 ft) of mining works carried out between old and modern, both horizontal and vertical.

This study of vibrations initially consists in the characterisation and classification of rock (quality of bad rock, type IV-B, with an RMR = 21 - 30) to prove the intrinsic properties such as compressive

strength, wave propagation speed and modulus of elasticity of rock mainly. Then the vibration monitoring was performed at varied distances from the trigger point considering equal operating loads to interpret the curve of the attenuation behaviour of the signal between the maximum vibration velocity (VPP) and the scaled distance (DR) using the point cloud wave vibration for our rock mass, with this characteristic attenuation law we predict the damage influence halos of each detonated hole and thus determine permissible operating charge of explosives for each rock quality which were carried out from April 01 – 2017 to April 30 – 2017 with a total of 38 seismographs as a result of the lifting of 48 blasting's between working stopes and full – face advance mining works. The charging of the blast holes was made using dynamite cartridges dynamite 'A' 45% of 1 1/8" X 12" (2.85 cm x 30.48 cm) and dynamite 'B' 45% of 1 1/8" X 8" (2.85 cm x 20.32 cm). (Technical specifications of dynamite 'A', 'B' in Annex1).

3 VIBRATION ANALYSIS AND MODELLING

The conducted work includes the study of predictive vibrations and control, the objective is to obtain seismic information of the 'explosive-rock' interrelation by providing a tool to approximate and approach the real conditions of the blast. Data collection was obtained through field monitoring surveys (monitoring).

For each explosive at d=0.6 m from the centre of gravity of the shot with a permissible vibration, limit of 304.5 mm/s at a drilling length of 1.829 m.

In order to analyse the vibration wave model we have to calculate the following parameters:

3.1 Hoek & Diederich Equation

Table 1. Input Data for Hoek & Diederich equation.

Nomenclature	Value
RMR89 Bieniawski Rock Mass Classification	25
GSI geological strength index	25
D disturbance factor	0
Em modulus of deformation (MPa)	1050.4
Em/Ei modulus relation	0.06
Ei deformation modulus of the intact rock (GPa)	17.5
Ei dynamic deformation modulus of the intact rock (GPa)	19.8

Where: D = 0 → No damage, D=0.5 → Moderate damage, D=1.0 → Severe damage.

For calculation purposes, 'D' was considered with a value of 0.

3.2 Determination of wave propagation velocity (Vp)

We have (Equation):

$$V_p = 3500 + 1000 \log(Q) = \dots$$

$$3,500 + 1000 \log(0.12) = 2,583 \text{ m/s} \quad (1)$$

Where Q = Barton's Q rating.

3.3 Particle Critical velocity VPPc (VCRIT)

Level at which the altered casing rock presents incipient fracture formation.

$$V_{crit} = \frac{\sigma_t \times V_p}{E_{i \text{ Dynamic}}} = \frac{2,34 \times 2583}{19,8} = 304,5 \text{ mm/s} \quad (2)$$

3.4 Devine's model, 1962

The DEVINE criterion (far field) was used for a multiple regression analysis based on scalar distance and the peak velocities recorded in each monitoring.

$$V_{pp} = K \times \left[\frac{d}{Q^3} \right]^{-\alpha} \quad (3)$$

Here:

V = particle velocity (mm/s)

d = Distance to blasting point (m)

K = Velocity factor

Q = maximum charge per delay (kg)

α = slope of the best-fit line of the V vs. D/Q^{1/3} plot on a log-log scale

From (3) we obtain:

$$Q = \left[\frac{V}{K} \times d^\alpha \right]^{\frac{3}{\alpha}} \quad (4)$$

The geologist provided the parameters of the rock (table 2) corresponding to each of the 2 explosives used.

Table 2. Constants of the Rock Massif of the Dynamites at CMHSA.

Explosive	K	α
Dynamite A	230.36	1.12
Dynamite B	852.05	1.81

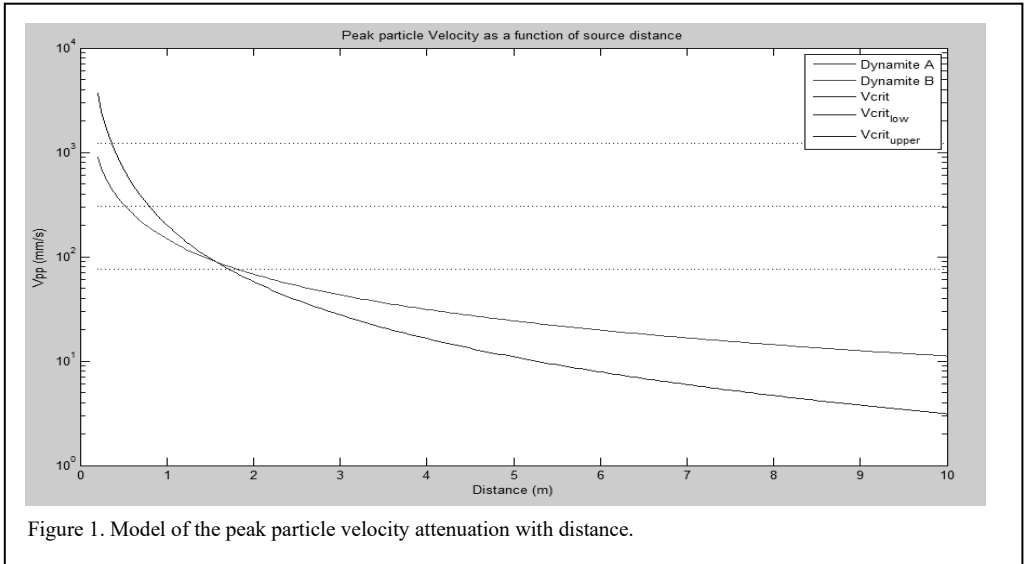


Table 3. Damage criteria.

Cameron McKenzie damage criteria	
4V_crit' → Intense Fracturing	4V_crit' → Intense Fracturing → 1218mm/s
1V_crit' → Creation of new invoices	1V_crit' → Intense Fracturing → 304,5mm/s
1/4 V_crit' → Existing fracture extension	1/4 V_crit' → Intense Fracturing → 76,13mm/s

Peak Particle Velocity V_{pp} is the maximum value of the speed of the particles during a vibration: it can be easily measured by seismographs. Knowing the distance from the source, the PPV at that point and the parameters of the rock, the evolution of the Peak particle velocity can be calculated using equation (3).

Seismic waves represent a transfer of kinetic energy: the energy is radiated in 3 dimensions from the source, so the energy flux decreases with the distance from the explosion. Moreover, due to non-elastic phenomena in the rock matrix, the wave dissipates energy. These factors induce a reduction of the wave amplitude and of the peak particle velocity with distance: this is accounted by the attenuation factor α of equation number 3.

According to the critical particle velocity, different damage levels can be identified.

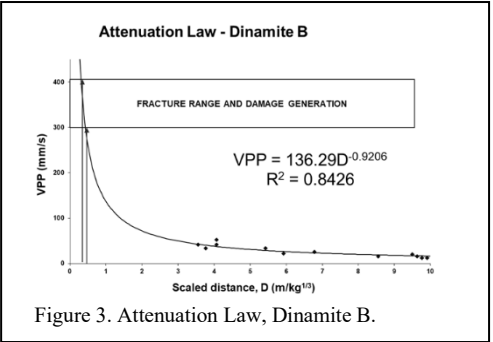
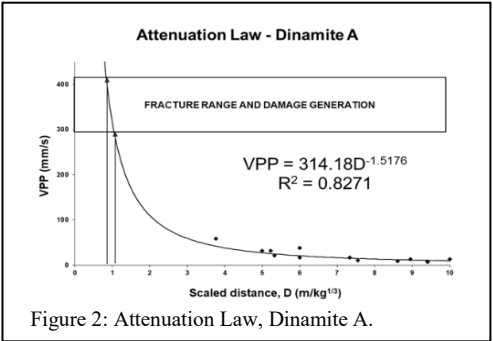
Using MATLAB, a simplified model has been produced, reported in figure (2).

3.5 Damage criteria: damage generation range for casing rock

Reference Table 3.

The maximum tolerable range for our case will be considered from 1 to 1.4 times the V_{crit} so we

have 304.5 mm / s (11.98 in/sec) at 426.3 mm / s (16.78 in/s).



3.6 Attenuation Law of Blasting wave

Each explosive has a certain release of energy to which a certain vibration level corresponds, so vibrographic data was taken from each type of explosive to determine its behaviour in the rock.

3.7 Maximum charge per delay

For each explosive at 0.6 m from the centre of gravity of the shot with a permissible limit vibration of 304.5 mm/s in a drilling length of 6 feet.

$$D = \frac{d}{\sqrt[3]{Q}} \quad (5)$$

Where:

d = Distance to blasting point (m)

K = Velocity factor

Q = maximum charge per delay (kg)

D: Scaled distance m/kg³, for cylindrical loads.

If d=0.6 m and replacing Eq. 2 in Eq. 4 maximum charge per delay is:

$$\text{DYNAMITE A} \rightarrow Q_{\max} = \left(\frac{304.5 \times 0.6^{1.5176}}{314.18} \right)^{1.977} = 0.203 \text{ Kg (2, 6 cartridges per delay period)} \quad (6)$$

$$\text{DYNAMITE B} \rightarrow Q_{\max} = \left(\frac{304.5 \times 0.6^{1.1191}}{230.36} \right)^{2.68} = 0.45 \text{ Kg} \quad (7)$$

6.25 cartridges per delayed period (one blast hole at a time) to 0.45 kg (0.992 lb) as maximum charge per hole and an influence from the centre of the 0.6 m (1.97 ft) blast is (Table 4):

Table 4. Type of damage.

Damage	
DYNAMITE – A → Q	Moderate
= 0,45kg → VPP	
= 455,44mm/s	
DYNAMITE – B → Q	Smooth
= 0,45kg → VPP	
= 302,91mm/s	

From the geomechanical characteristics of the rock we have the following summary table in which it is worth noting that the average wave propagation velocity (Vs) is 2,969 m / s (9,740.81 ft/s) and the average critical rock fracturing velocity (VPPcrit) is 376.9 mm / s (14.84 in/s).

3.8 Vibration analysis for the influence of damage

Clearing the formula of Devine (Equation 3) the distance 'd' and calculating the new formula with the constants 'K' and 'α' by type of explosive used in each blast hole we determine approximately the influence of damage by each one of the detonated blast hole sequentially as shown in the Table 6.

Table 5: Geomechanical parameters of rock.

CALCULATION OF SPEED PEAK CRITICAL PARTICLE OF THE ROCK			
CMHSA			
Field data:			
Underground mining	: Lourdes	Type of rock	: altered granodiorite
Work	: Cx2805	Squeeze of strata	: sub horizontal fracturing to the excav.
Analysis	: Vibration analysis	Material to blast	: clearance
Date	: 03/04/17	Filling of joints	: Qz. Closed, alteration to the ceiling
Zone	: North	Spacing of joints	: 0.13 - 0.18 cm
		State of rock	: deepening ramp
Geomechanical data:			
A	: Total number of fractures per cubic m	Max	Min
		10	7
			8.5
RMR _{sa}	: Rock Mass Rating (in dry conditions)	50	46
			48
RMR	: rock Mass rating (tight)	35	31
			33
δ	: Density of the rock (Ton/m ³)	3	2.8
			2.9
D	: Damage Index	0	0
			0
GSI	: Geological resistance index	30	26
			28
E _m	: Modulus of elasticity of the rock mass	1.65	1.15
			1.4
E _{mZ_i}	: Elasticity module relationship	0.08	0.06
			0.07
E _i	: Modulus of elasticity of intact rock (G)	20.2	18.1
			19.2
E _{id}	: Modulus of dynamic elasticity (Gpa)	22.8	20.5
			21.6
σ _o	: Uniaxial compressive strength, (Mpa)	30	25
			27.5
Output data:			
Calculation of RQD:			
RQD (%)	=	Min	Max
		44.00	70.00
Q	=	0.37	0.24
			0.30
Vs (m/s)	=	3,066.00	2,873.00
			2,969.00
Vs (ft/s)	=	10,059.06	9,425.85
			9,740.81
Vppc (mm/s)	=	402.70	351.10
			376.90
Vppc (ft/s)	=	1.32	1.15
			1.24
Calculation of tunnel quality index:			
Calculation of the sonic velocity of the rock mass:			
Calculation of critical particle peak velocity:			
Vppc (mm/s) = (0.1 x σ _c x Vs) / E			
Estimation of Damage Index			
Without damage	D	0	
Intermediate		0.5	
Severe		1	

Table 7. Maximum operating loads per type of explosive.

Explosive	Damage distance	Q average	Cartridges explosive/hole
Dynamite B 7/8" X7	0.2 m	0.06 kg	1.02
Dynamite A 1 1/8" X12	0.6 m	1.6 kg	7.98

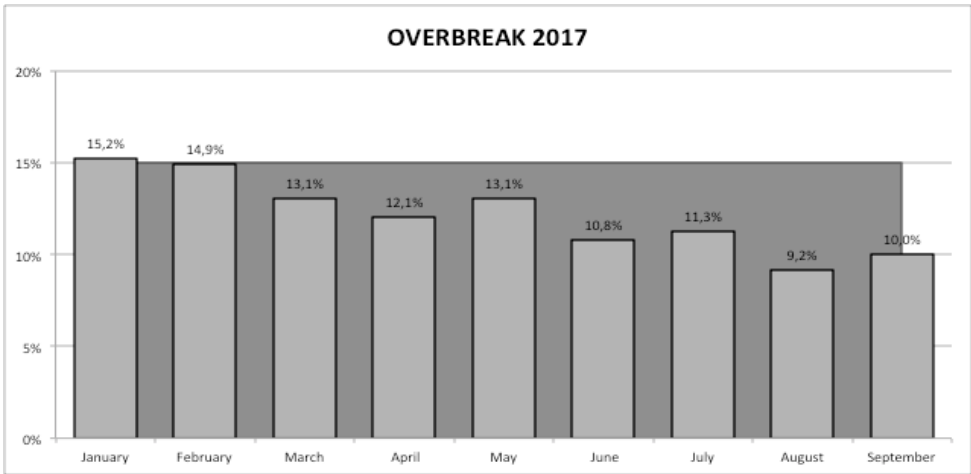


Figure 4. Overbreak by 2017.

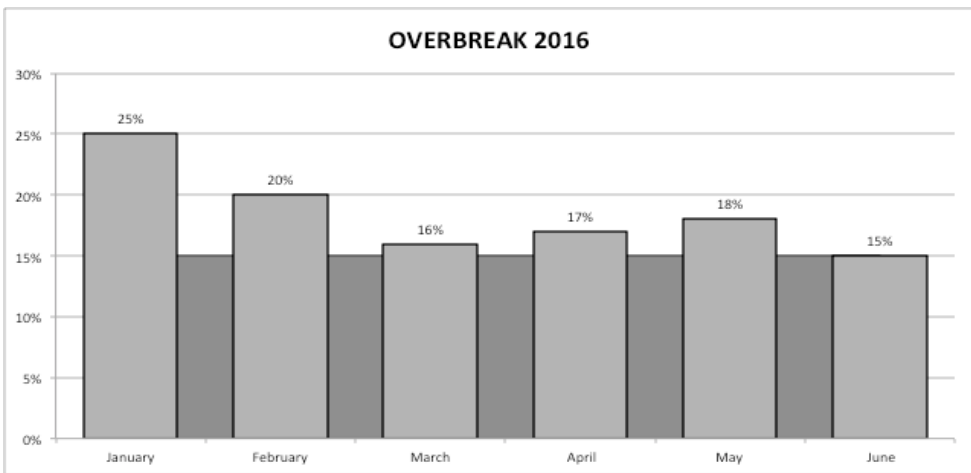


Figure 5. Overbreak by 2016.

4 RESULTS

4.1 Overbreak in full-face advance

Sampling was done in different works of exploration face or cross section, preparation and development of the mine, with different qualities of rock mass measuring the real section and comparing with the design section it was

determined that the factor of overbreak is 12% from January to August of 2017; while, for 2016 it was 15.6%. With the control and fulfilment of these changes it is expected to reduce the over excavation of 9.2% by the end of 2017.

Performing the analysis of vibrations as the main object involves reducing the overbreak rate, which directly involves extracting and hauling less

Table 8. Support cost 2016.

Waste Rocks	Cost \$ 15.6%	\$/TMS	Cost \$ 9.2%	Savings \$
308,121 TMS	1,468,995	4.8	1,333,847	98658

Table 9. Transportation cost 2016.

Waste Rocks	Cost \$ 15.6%	\$/TMS	Cost \$ 9.2%	Savings \$
308,121 TMS	352,967	1.15	320,494	32,473

Table 10. Underground extraction cost 2016.

Waste Rocks	Cost \$ 15.6%	\$/TMS	Cost \$ 9.2%	Savings \$
308,121 TMS	152,009	0.49	138,024	13,985

Table 11. Materials cost 2016.

Waste Rocks	Total rock break	Total \$	\$/TMS	Cost \$ 15.6%	Cost \$ 9.2%	Savings \$
308,121 TMS	822,458	2,317,336	2.82	868,154	788,154	58,305

waste, reducing the consumption of materials for maintenance, less energy consumption considered the most significant expenses in linear work. Below are attached 2 figures that represent the Overbreak during 2016 and 2017. The permissible limit of Overbreak is 15% for the quality of the rock mass. (60% with an RMR of 21-30).

The following costs analysis was performed with data from 2016 and costs at 15.6% and 9.2% in the forecast of overrun – see Tables 8 to 11.

In 2016, the cost of sustaining progress was US \$1,468,995 - see Table 8.

The cost average for waste rock transporting for the year 2016 was 1.15 (\$ / TMS), reducing the overbreaking in 9.2% would have \$ 32,473 annually. The waste rock is transported in dump trucks to a waste dam located 5 km (3.11 mi.) from Balcón mine entrance in Curaubamba – See Table 9.

The cost average of extraction of waste rock for the year 2016 was 0.49 (\$ / TMS), reducing the over excavation by 9.2% would have \$ 13,985 of savings – see Table 10.

The cost for materials concept for 2016 was US \$ / 2,317,336. This includes materials for rehabilitation work and sustaining liabilities – see Table 11.

In summary, there would be a projection in savings of 9.2% of \$ 203,421 annually compared to 2016.

As a result of these changes we have reduced overbreaking from 18.5% to 12%, which directly reduces the consumption of shotcrete from 175 to 110 m³/day, mucking times up to 25 minutes,

extraction of waste rock in 27% less, this summarises the increase in mineral contribution from 1800.0 t/day (1632.93 T/day) to 2000.0 t/day (1814.37 T/day) and achieve with the monthly progress from 75% to 96%, because of the reduction of operational problems on blasting. Maintaining and improving these historical data of efficiencies in the operation will be because of the constant monitoring and improvement on these works.

The implementation of pre-cut blasting technology and decoupling of peripheral charges with low-explosive (explosive used only in) have also made an important contribution.

4.1.1 Tests of Hess relied on dynamite as confirmation of low power explosives

The dynamite 'B' 45% of 7/8" X 7" (2.22 cm x 17.78 cm) and 1 1/8 "X 8" (2.85 cm x 20.32 cm) and dynamite 'A' 45% of 7/8" X 7" (2.22 cm x 17.78 cm) and 1 1/8 X 12" (2.85 cm x 30.48 cm) used in the work of production and advance have positive results regarding the control of the excavation. It is adapted to the poor quality of our work rock. With a VOD that fluctuates between 2,200 m/s and 3,800 m/s, Hess 7 mm and low levels of vibration, (Tests carried out in, Figure 8, 9 and 2,3 & 10, Annex 2).

4.2 Fragmentation analysis

The most common method to evaluate fragmentation after blasting is a simple visual estimation of the rocks on the pile of the broken

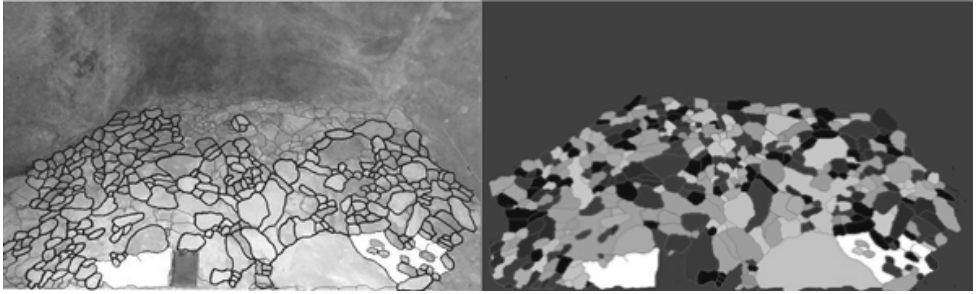


Figure 6. Granulometry of the rock after rock blasting.

material. While this is a way of detecting the most superficial problems, it is a too subjective way to carry out a program of deep evaluation of blasting. The fragmentation analysis is presented below, using the WipFrag software, which performs this operation through photographic analysis of the explosive charge.

4.2.1 Fragmentation Analysis in a production work: Tajo 2926 S Mina Lourdes Split

For this working stope, a 15 cm (5.90 in.) scale was used to estimate the P80. The result obtained after this analysis indicates a P80 of 7 cm (2.76 in.).

5 CONCLUSIONS

The operating costs (2,016 were as detailed):

- Reinforcement 4.80 (\$ / TMS)
- Transport 1.15 (\$ / TMS)
- Extraction 0.49 (\$ / TMS)

- Materials 2.82 (\$ / TMS)

These items make a total of US\$ 9.26 / TMS, it means that in 2016 were moved 308,121.0 TMS with a total cost of US\$ 4,476,998.13. That year the overbreak was estimated at 15.6% (Annex 2) in linear works. For 2006 the break was 265,019.54 TMS with a total of \$ 3,103,378.81 with 14% overbreak.

Considering the design adjustment in the Blasting by vibration modelling, there would have been savings of 9.2% over break, of \$ 286,527.88 for 2016 and \$ 148,962.183. With an annual projection of US\$ 203,421.00 of savings without considering the specific consumption of explosives.

The characterisation of the rock mass has a great importance to carry out the damage analysis according to the particle vibration limit levels that it offers, being able to establish a rock classification according to the speed of wave propagation according to the particularity of each mineral deposit for the measurement and control

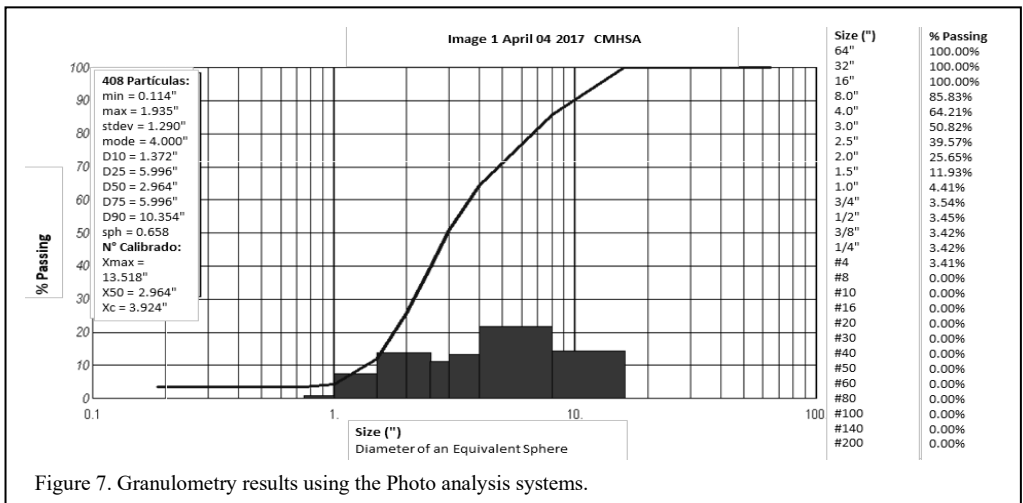


Figure 7. Granulometry results using the Photo analysis systems.

of blasting damage.

The near-field modelling of Devine requires a greater collection of data (monitoring) to get closer to the real ground conditions that allow us to adjust the initial mathematical models and establish design parameters such as operating charges and intensity of damage according to real conditions.

The use of low VOD dynamites and breaking power such as the dynamite 'B' allows the charged column to be lengthened without having to increase the operating charge used as a continuous charge, generating a smooth cut in the contours of the excavation that avoid maintenance problems, considering that the biggest problem of blasting is not the fragmentation but the stability of the mining labors because of the poor quality mass rock of the mineral deposit which goes from very fractured to intensely fractured, making difficult the mining works.

The delay time is also very important as a reductive factor of vibration that was already established, effects of destructive couplings to 25 ms that are counted with the triggering of a drilling at the same time, avoiding exceeding 0.45 Kg (0.992lb) / challenged as operating load pattern.

According to the results obtained in the fragmentation analysis, the P80 in the pit 2926 S Lourdes was 7 cm (2.76 in.).

The additional cost of advancing to 25% of over-excavation is \$ 189/m (\$57.61/ft), so the forecast by the end of the year with the application of these controls is expected to have over-excavation of 9.2% that would be \$ 65 /m (\$19.82/ft) cost reduction of 65%.

REFERENCES

Sandoval, O. & Guillen H. 2011. Determination of the width of mining with mechanised support. *Perumin 30th Mining Convention* (pp. 2). Arequipa: Perumin.

Instantel. (2013). *Minimate Plus Operator's Manual*. Ottawa, Ontario, Canada.

Practical blasting manual 5th edition, EXSA.

APPENDICES

Appear on the following pages.

APPENDIX 1. Technical specifications of dynamite 'B' and 'A'.

Technical Characteristics			
Technical Specifications.	Units	Dynamite B	Dynamite A
Density	g/cm ³	0.8 ±3%	1.08 ±3%
Detonation Velocity *	m/s	2,800 ± 200	3,800 ± 200
Detonation Pressure **	kbar	23	87
Energy**	KJ/Kg	1,720	3,060
RWS**	%	47	83
RBS**	%	45	109
Water Resistance		Nula	Ok
Category Smoke		1 era	1 era

* Unconfined in 30 mm diameter triplate tube

**Calculated with a TERMODET simulation program.

APPENDIX 2. Tests performed at Dynamite 'A' and 'B'.

Table 12: Results of quality controls, detonation speed, Hess, water resistance and sympathy Dynamite A.

Dynamite specifications	Detonation velocity	Hess	Water resistance	Sympathy
	3,600 – 4,000	17 - 20		2Φ
Dynamite A 45% 1 1/8"X12"	3,805 m/s	19.52 mm	2 hr 40 min	OK
Dynamite A 45% 1 1/8"X12"	3,917 m/s	19.36 mm	2 hr 40 min	OK

Table 13: Results of quality controls, detonation speed, Hess, water resistance and sympathy Dynamite B.

Dynamite specifications	Detonation velocity	Hess	Water resistance	Sympathy
	2,600 – 3,000	13 - 16		2Φ
Dynamite B 45% 1 1/8"X12"	2,821 m/s	13.88 mm	Null	OK
Dynamite B 45% 1 1/8"X7"	2,756 m/s	13.89 mm	Null	OK

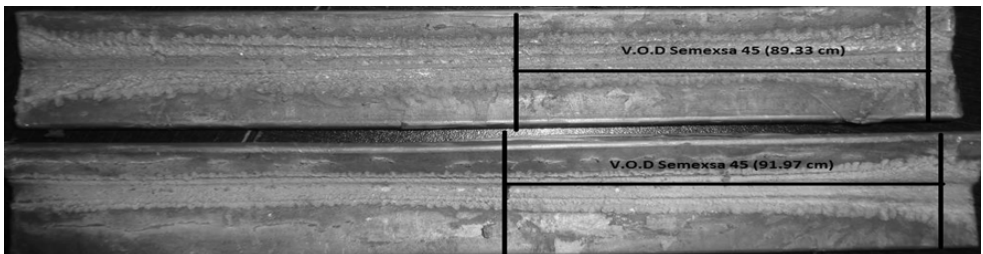


Figure 8. Results of Dynamite "A" 45% Detonation Rate measurement (VOD).

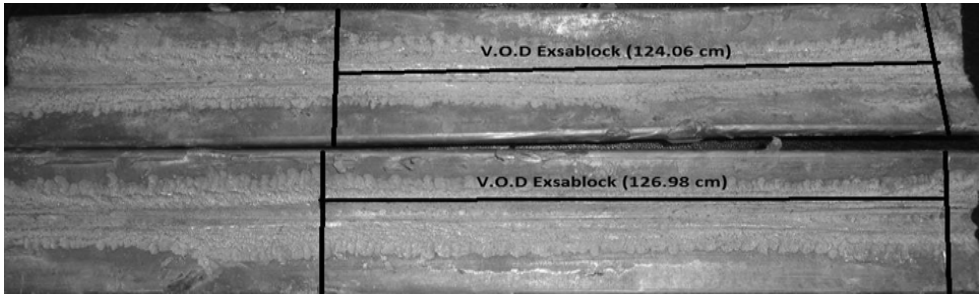


Figure 9. Results of Dynamite "B" 45% Detonation Rate measurement (VOD).



Figure 10. Results of the Hess after the detonation Dynamite 45% "A" and "B".

APPENDIX 3. Nomenclature

- CMHSA: Mining Consorcio Minero Horizonte SA
- P80: This value means that 80% (by mass) of the solid matter has a smaller grain size P80.
- Q: Operant charge weight of the explosive charge that detonates by delayed period.
- Dynamite A: Semexsa 45%
- Dynamite B: Exsablock 45%

Rock blast induced pore pressures in quick clay

J. Johansson, S. Gjengedal, J. Park, K.H. Andersen, C. Madshus, & S. Rønning
Norwegian Geotechnical Institute, Oslo and Trondheim, Norway

ABSTRACT: In 2009 rock blasting for a road construction pushed a block of rock into a quick clay area resulting in a large landslide in Namsos, Norway. This slide also triggered the question of whether vibrations other than earthquakes can cause quick clay landslides. A first study in 2012 resulted in a Norwegian standard (NS 8141-3) for a vibration limit and measurement procedure for safer blasting near quick clay. Recent projects have shown the need to better understand how blast vibrations affect quick clay and how to deal with it during road and railroad construction. In connection with a road construction, we measured blast vibrations both in and on rock and on ground surface and at 2 depths in clay as well as pore pressure in the clay at 5 and 10 m depths. Blast vibration peak value of about 90 mm/s (vector sum) caused a modest pore pressure increase of less than 3 kPa in the quick clay, which is smaller than the natural variation over a season. Nevertheless, since pore pressure increase reduces the quick clay strength it is recommended to stay below set limit of 25 mm/s in the standard if not a more detailed site-specific analysis show higher vibration values can be allowed.

1 INTRODUCTION

Rock blast induced quick clay landslides are fortunately fairly uncommon in Scandinavia (Bouchard *et al.* 2018). However, in 2009 blasting triggered an initial slide by pushing a block of rock into the quick clay resulting in a large landslide (Saygl *et al.* 2017). This slide also re-initiated the discussion of whether blast vibrations can trigger landslides in sensitive soils. In a follow up research study in 2010-2012 a vibration limit was suggested and later implemented in the NS 8141-3:2013.

However, the current standard does not cover tunnel blasting nearby slopes. Therefore, to gather more field data to understand better how blasting may cause strength reduction in quick clay due to pore pressure build up, an extended monitoring program was executed in connection with a road construction project. Vibrations were recorded for over 20 blasts, and pore pressure was monitored

for some 12 blasts. Some key observations and analysis are described below.

2 EFFECT OF BLAST VIBRATIONS ON QUICK CLAY SLOPES

There is still a lack of knowledge about the mechanisms for how blast vibrations can trigger landslides. For some landslides it is clear large vibrations contributed to the slide, e.g. the Fröland (Bjurström 1982) slide in Uddevalla, Sweden, the more recent La Romaine slide in Canada (Bouchard *et al.* 2018) where the slide occurred right after the blast. For other landslides where vibrations may have been a contributing factor, the slides have occurred some hours after the blast. A recent example is the landslide in April 2021 at Steinvika in Tana in Eastern Finnmark, Northern Norway, where the slide occurred some 10-15 hours after a large blast.

Contrary to, for example, earthquake shaking, blast vibrations decrease rapidly with the distance from the blasting area and therefore it is assumed that the pore pressure build-up and thereby strength reduction occurs locally near the contact between rock and clay, closest to the blasting. If blast-induced pore pressure cannot dissipate rapidly enough to rock fractures and/or more permeable soil layer, often present between rock and clay in Norway, a possible mechanism for causing a failure may be that pore pressure propagates to surrounding areas with lower stability contributing to a reduction in material strength and resulting in an accelerating creep failure in the slope and possibly to a progressive failure.

Quick clay often has embedded layers of loose silt of varying thickness. It is not understood whether a failure starts in the silt layers and pore pressure propagates into the clay, reducing its strength, or if it is the clay between the silt layers which fails due to blast vibrations, or a combination of both.

Another issue is the blast induced cyclic strain rates in the soil are much higher than, for example, earthquake vibrations. The effect of these high strain rates on pore pressure generation and accompanying effects on the stiffness and strength of Scandinavian quick clays are not well understood due to very few investigations with cyclic tests (Johansson 2013) on such clays. Since earthquakes are more common in Canada than

Scandinavia, there are several studies on Canadian quick clays which provide useful insights to their cyclic behaviour (Abdellaziz 2021, Quinn *et al.* 2012, and Lefebvre 1989). However, transferring experiences has to be done carefully since quick clay properties vary from site to site, and even more so between countries.

3 SITE DESCRIPTION AND INSTRUMENTATION

For the construction of a new highway stretch of the E6 North of Trondheim in central Norway, a small hilly rock outcrop, some 15 m high has been trenched down with a total of 23 bench blasts as shown in Figure 1, in April-June 2021. An extensive blast monitoring program was executed, measuring vibrations in both rock and clay, and pore pressures at several locations in the clay.

The ground conditions are relatively well characterised with several rock depth soundings, a few soil (CPTU) soundings, and samples were also taken up for laboratory index and shear stress tests on the quick clay. The site is an old quarry infilled bay between a county road to the south and the hill trenched down to the North. The depth to gneiss bedrock increases from a few metres in the East to some 13-20 metres in the West.

Figure 2 shows a plan view of the vibration and pore pressure sensor locations. Triaxial geophones (Infra V12 and V12 b prod. Sigicom) were used to monitor vibrations. Three geophones were

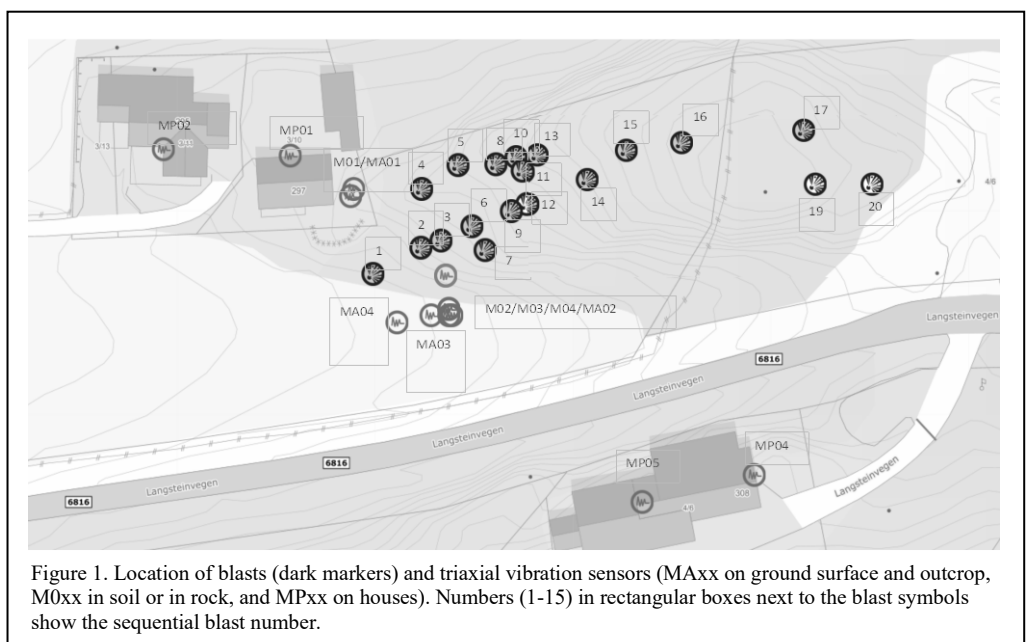


Figure 1. Location of blasts (dark markers) and triaxial vibration sensors (MAxx on ground surface and outcrop, M0xx in soil or in rock, and MPxx on houses). Numbers (1-15) in rectangular boxes next to the blast symbols show the sequential blast number.

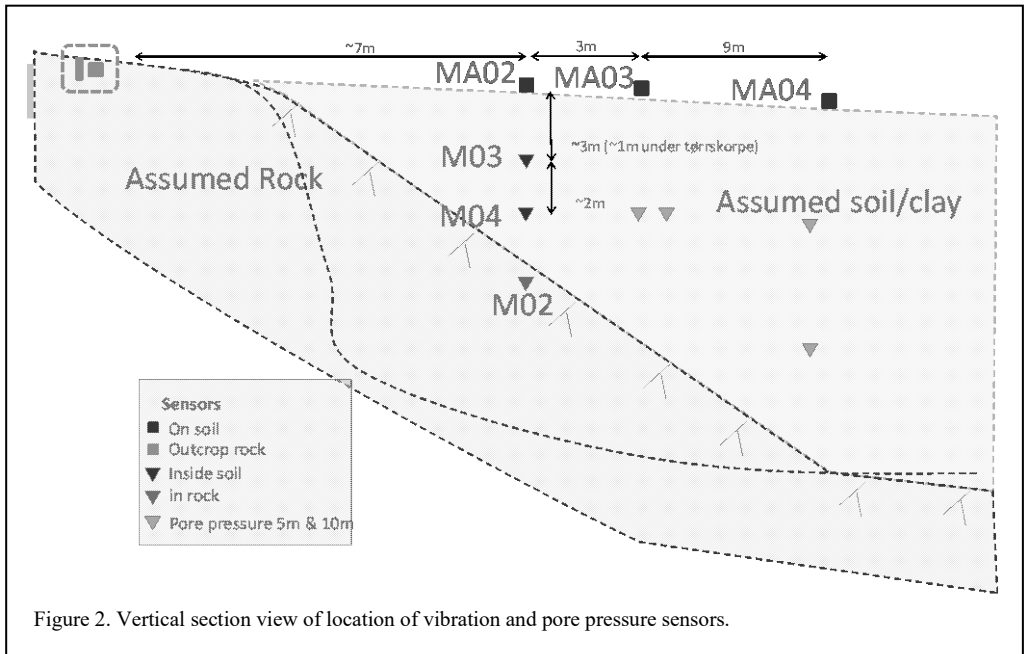


Figure 2. Vertical section view of location of vibration and pore pressure sensors.

installed on the concrete blocks placed on line with 3 m and 9 m in between and pushed with an excavator down into the top soil in the ground surface, two geophones were installed in clay at 3.5 m and 5 m depth from ground surface (below dry crust), one on outcrop rock and one in rock at 7.5 m depth. 4 pore pressure meters from Geotech were installed at 2 locations at 5 and 10 m depths. The geophones were installed in clay at the desired depth in clay as follows. The geophone was attached to a plastic pipe, inserted in a bore hole with casing, then pushed half a metre into the clay below the bore hole and finally released from the plastic pipe. Similarly, the geophone in rock, was inserted beneath the clay through a cased hole and fixed with swelling bentonite pellets. High signal coherency between the sensors on outcrop and in rock gave confidence to the installation method and the measured vibrations.

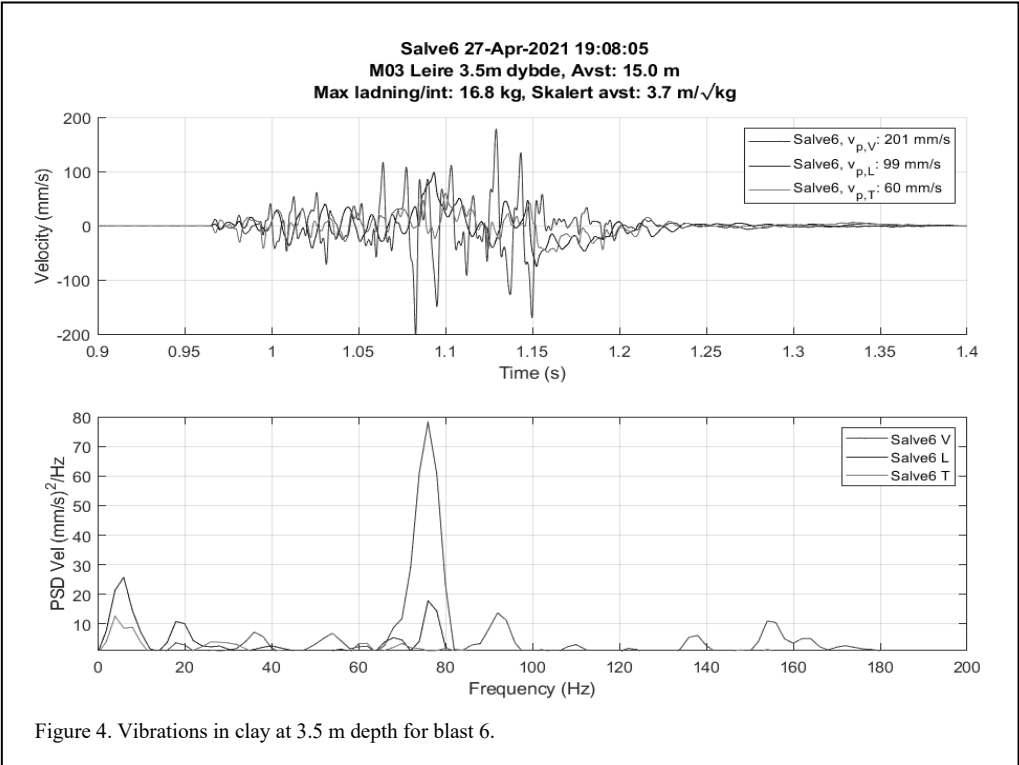
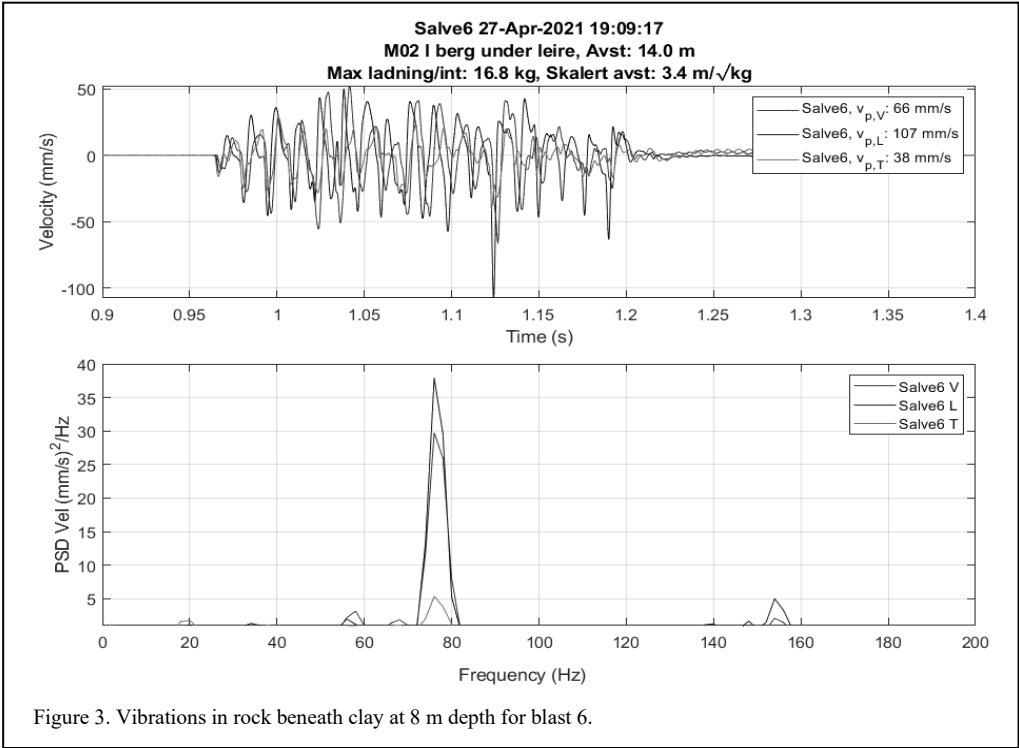
4 BLAST INDUCED VIBRATIONS

The measured blast vibration duration ranges between 0.2 – 1.0 seconds, depending on time delay between charges, number holes, and decks in the blast. The vibrations in rock tend to be dominated by 1-3 frequencies between 10 to 150 Hz. These frequencies appear to correspond to the time delays (10-20 ms) between charges and blast rows (70 ms). Vibrations in soil are also dominated by a few or sometimes only one frequency. One of the dominant frequencies, often

seem to agree with the time delay between charges. The geometry and mechanical properties of the rock and soil do also affect the frequencies in the soil, and further evaluation of this is underway. The number of stress cycles in the soil, which is important for strength reduction in soil due to pore pressure build up, appears closely related to the number of charge holes in the blast design.

The largest vibrations in rock and soil were recorded for blast number 6. Most of cycles in the rock vibrations are around 50 mm/s with one pulse of 100 mm/s (Figure 3) and dominating frequency of about 75 Hz, which is within 5% of the time delay of 14 ms. The vibrations in clay at 5 m depth (not shown) are overall similar to those in rock, only with slightly larger amplitudes of 60 mm/s. In the clay at 3.5 m depth (Figure 4) the vibrations have larger vertical amplitudes with several cycles above 100 mm/s and one pulse over to 200 mm/s with vibration frequency of about 75 Hz.

Vibrations on the ground surface are to some extent affected by the stiffness and thickness of the layer with softer top soil above the clay's dry crust, and show a distinct frequency around 25-30 Hz. Therefore, it appears better to measure vibrations down in the clay instead of on the soil surface, to identify amplitudes, frequency content and duration for correlation with the pore pressure measurements.



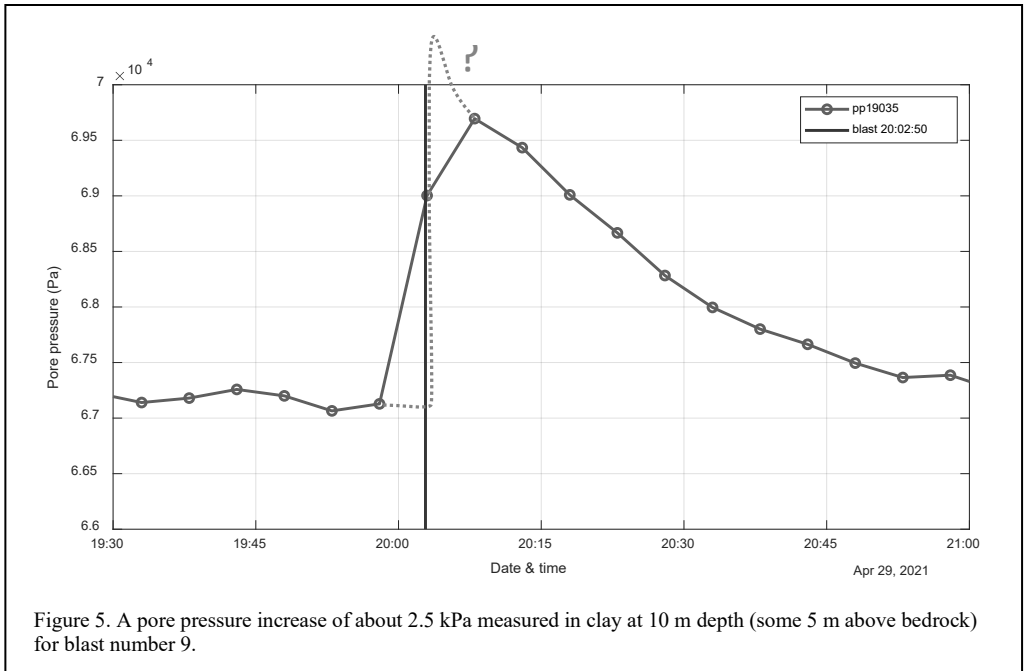


Figure 5. A pore pressure increase of about 2.5 kPa measured in clay at 10 m depth (some 5 m above bedrock) for blast number 9.

The vibrations measured during the blasts, are in general stronger in the soil than they are down in the rock. More analysis is needed to better understand how the vibrations are transmitted from the rock on the side of and beneath the soil and possible wave amplification in the soil. Measurement data should be further interpreted accounting for the different vibration directions and frequency content, distance and direction to blast, and geometry and properties of the rock and soil.

5 BLAST INDUCED PORE PRESSURES

In general, the larger vibration amplitude and the more load cycles, the higher pore pressure is built up in soil. Therefore the blasts closest to the border between the boundary between the rock and clay are of most interest for observing pore pressure increase since they give the largest vibrations in the soil. The first 15 blasts caused vibration levels above 20 mm/s (vector sum) at the sensor in clay at 5 m depth. For this vibration level some pore pressure is expected to have been built up. Some small increases in pore pressure of 0.5-2.5 kPa have been measured after 4 of the blasts. For another 3 blasts pore pressure may have increased, but the natural variation in pore pressure makes interpretation difficult. Furthermore, some of the early blasts may have contributed to soil densification making it less prone to build up pore

pressures in the subsequent blasts. The largest pore-pressure increase of 2.5 kPa (shown in Figure 5) was measured for blast number 9 with the corresponding vibration values (vector sum of top values) in clay of 87 mm/s at 5 m depth and 52 mm/s at 3.5 m depth. The largest vibrations were measured for blast 6 (Figure 4), unfortunately the piezometers were not installed until blast 8, during which about 1 kPa increase was observed for vibration level of about 30 mm/s.

Maximum pore pressure occurred some few minutes after blasting and was reduced to background pore pressure within 1-2 hours. Due to low sampling frequency of the pore pressure its peak value may have been larger as indicated by the dotted curve in Figure 5. The time delay between the blast and the pore pressure peak hints at the pore pressure possibly migrating from an area where larger pore pressures are induced by large shear strains / stresses in the clay. Numerical calculations show that the largest cyclic shear strains are induced in the zone in the clay up to the rock wall while the pore pressure was measured in the clay at a distance of 5-10 m from the transition between rock and clay (an example is shown in Figure 6). Due to the relatively rapid build-up and diffusion of pore pressure, more frequent sampling of pore pressure, at least every minute or faster, is recommended.

The time it takes to reduce blast-induced pore pressure is much faster than what lab tests indicate. It is likely that the field permeability is much higher than measured in the laboratory. For example, it is often the case that horizontal permeability is higher than vertical permeability. It is possible that coarser material (moraines) that has been observed between the quick clay and the rock, and cracks in the rock as well, contribute to the relatively rapid reduction of pore pressure.

The pore pressures measured so far are not of concern with respect to slope stability since they have been for stable slopes with small ground inclination. However, it is important both vibrations and pore pressure are monitored when blasting near less stable slopes, since larger pore pressures may be generated by vibrations due to higher static shear stresses mobilised in the soil.

We have assumed here that vibrations transmitted from rock to clay is the cause of the measured pore pressure increase. It is also possible that blast gas pressures, propagating through cracks in the rock out into the clay, may contribute to the pore pressure build up. Further evaluation of this mechanism should be conducted.

6 COMPUTATION OF VIBRATIONS AND PORE PRESSURES

In general, larger vibration amplitude and more load cycles cause larger pore pressure increase in the soil. To correlate measured vibrations and pore pressures, equivalent linear numerical analyses have been performed to compute cyclic shear strain and stresses in the soil with the same approach as in Johansson *et al.* (2020). The numerical analyses justify the simple approach of estimating cyclic shear strain in the clay by taking the ratio of the particle velocity and the secant shear wave speed. Shear wave speeds were estimated with empirical formulas (LHeureux 2018) based on sounding (CPT) values and undrained shear strength values in the clay. The nonlinearity of the clay was accounted for by NGI's in-house cyclic database (Andersen 2015). Back calculation of pore pressure was performed, based on contour diagrams, similarly to the approach for computing permanent shear strains (Johansson *et al.* 2013). The analyses indicate that moderate pore pressures should be expected to be built up for 10 vibration cycles of 25 and 50 mm/s. However, for vibrations of 100 mm/s, the

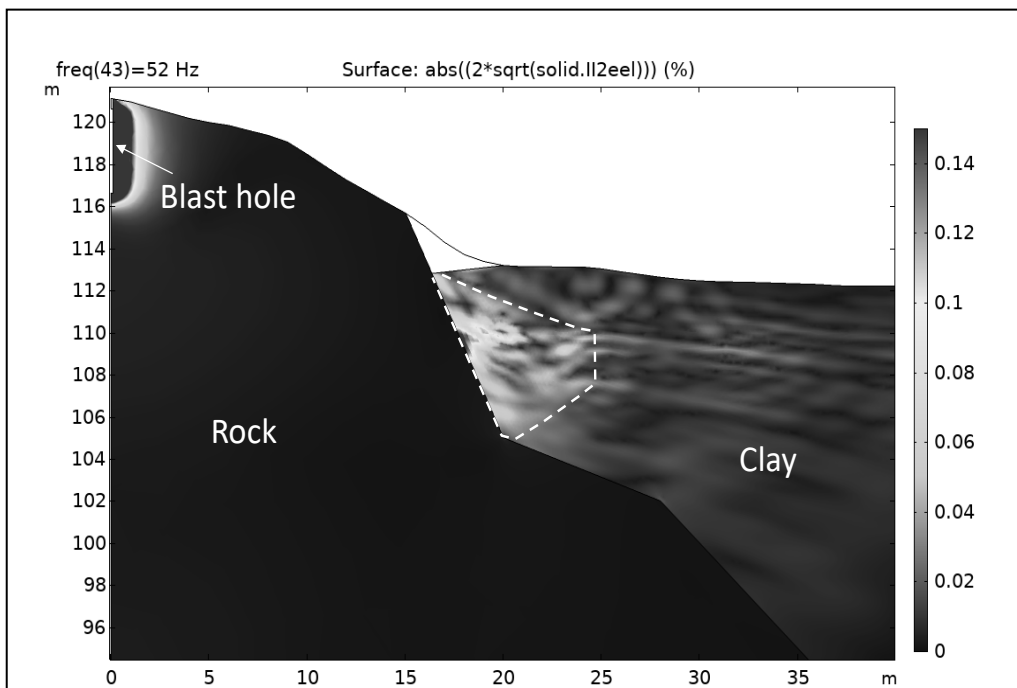


Figure 6. Maximum shear strain plot from dynamic FE simulations of a rock blast in rock close to soft clay. A zone with large shear strains marked with a white dashed line delineates a zone where excess pore pressure could be generated.

substantial amount of pore pressure increases should be expected, as Table 1 illustrates.

The computed pore pressures seem to be of the correct order of magnitude. However, for a better comparison, the computed pore pressures with the measured ones further numerical analysis of pore pressure generation and spreading in the soil is necessary. If the pore pressure is generated at the boundary between the rock and the clay, and then propagate out to the surrounding soil, the pressures should likely decrease rapidly with distance from the generation zone. Thus, the piezometer location in relation to this zone may have a large effect on the observed pore pressures.

The computed pore pressures are based on material data from laboratory experiments performed at a load frequency of 1 Hz. The blast induced vibrations are in general around 10 Hz or higher. Thus, the strain rates are at least an order of magnitude larger due to blasting compared to lab tests. Increasing the lab test frequency from 0.1 Hz to 1 Hz reduces pore pressure generation with at least a factor of 2. It is therefore expected for blast induced vibrations at frequencies of 10 Hz and above, the pore pressure generation should be even lower. Further exploration with high frequency lab test may further clarify the issue of strain rate effects on pore pressure build up.

Table 1. Computed pore pressures based on cyclic loading contour diagrams for different vibration amplitudes.

Vibration amplitude (mm/s)	25	50	100
Pore pressure increase for 10 stress cycles (kPa)	2	5	30

7 SUMMARY AND CONCLUSIONS

A rock blast induced landslide in 2009 in Norway re-ignited the question of whether blast vibrations can cause instability in slopes with quick clay. A follow-up research project resulted in recommendation to keep blast vibration under a limit of 25 mm/s, under such conditions. This was implemented in the Norwegian standard NS 8141-3. However, the present issue of the standard only covers limited slope and blast geometries, and not, for instance, tunnel blasting beneath quick clay slopes. Therefore, in 2021 in connection with road construction, vibrations and pore pressures in quick clay has been measured during both surface and tunnel blasting.

Even though the measured vibrations superseded the NS 8141-3 vibration limit of 25 mm/s with a factor of 4 and more, only small or moderate pore pressure increase of some 3 kPa have been observed in soil some 2-5 m above the bedrock. The pore pressures increase with the cyclic shear strain amplitude in the soil and the number of cycles. Cyclic laboratory tests indicate a strong inverse dependence on the vibration frequency. Increasing the loading frequency in the laboratory from 0.1 s to 1 reduces the pore pressure build up by a factor of about 2 or even more for the same load amplitude and number of load cycles. The high frequency of the blast vibrations may explain the relatively low excess pore pressures observed.

The measured pore pressures increase nearly instantaneously due to the blasting and then dissipate relatively quickly to the previous level within 1-2 hours after the blast. The pore pressures so far measured from the blasts are lower than seasonal pore pressure variations in the area and smaller than measured pore pressures due to pre-injection grouting of the rock ahead of the tunnelling. The blast vibration induced pore pressures are therefore of no concern to slope stability at the locations where it has now been measured as reported herein. When blasting near less stable slopes, larger pore pressures may be generated by the vibrations due to higher static shear stresses mobilised in the soil. The propagation of pore pressure may lead to an undesirable strength reduction in parts of a slope which is highly mobilised (high shear stresses in relation to strength). It is therefore important to monitor both vibrations and pore pressures closely at critical locations. If induced pore pressures are high, they should be allowed to dissipate before the next blast is set off. Vibration sensors placed inside the clay at some depth intervals give a better indication of the vibration loads than sensors placed on the ground surface. Sensors placed on houses may give a factor 3 or lower vibrations than in the clay, and are not recommended for this type of evaluation.

The blast induced pore pressures are most likely generated in a boundary zone between rock and clay closest to the blast area. The pore pressures then propagate away from this zone out to the surrounding soil. Recent measurements not described here indicate the propagation speed is of the order of 1 m/minute in a typically quick clay, possibly controlled by the soil's hydraulic conductivity and stiffness. Further investigations are needed to understand the mechanism for pore

pressure generation and propagation. The hypothesis so far is that pore pressure is caused by vibrations in the clay, in a similar way as for earthquake soil liquefaction. However, it may also be possible that blast gas pressures may contribute to the pore pressures near tunnel blast sites.

The data set of vibrations and pore pressures described in this paper and a corresponding set from another recent tunnel blasting project will allow for further and more detailed studies to better understand how rock blasting affects quick clay slopes.

8 ACKNOWLEDGMENT

The permission to publish this material was granted by Nye Veier (Norwegian public road company) and is highly appreciated. Contributions to the work from the contractor Hæhre, from rock engineering specialists at Sweco and specialist providers of vibration and pore pressure measurements at Nitroconsult and Geotech are gratefully acknowledged.

REFERENCES

- Abdellaziz, M., Karray, M., Chekired, M., Delisle, M.C., Locat, P., Ledoux, C. & Mompin, R. 2021. Shear modulus and hysteretic damping of sensitive eastern Canada clays. *Canadian Geotechnical Journal*, 58: 1118–1134. Canadian Science Publishing. doi:10.1139/cgj-2020-0254.
- Andersen, K.H. 2015. Cyclic soil parameters for offshore foundation design. The 3rd ISSMGE McClelland Lecture. *Frontiers in Offshore Geotechnics III, ISFOG'2015, Meyer (Ed)*. Taylor & Francis Group, London, ISBN: 978-1-138-02848-7. Proc., 5-82. Revised version in: <http://www.issmge.org/committees/technical-committees/applications/offshore> and click on 'Additional Information'.
- Bjurstrom, G. 1982. The landslide at Froland, June 5, 1973. In *Symposium on Slopes on Soft Clays, Swedish Geotechnical Institute Report No. 17*, Linköping, 113-126.
- Bouchard, S., L'Heureux, J.S., Johansson, J., Leroueil, S. & LeBoeuf, D. 2018. Blasting induced landslides in sensitive clays. In *Landslides and Engineered Slopes. Experience, Theory and Practice*. edited by S. Aversa, L. Cascini, L. Picarelli, and C. Scavia. CRC Press. pp. 497–504.
- Lefebvre, G., LeBoeuf, D. & Demers, B. 1989. Stability threshold for cyclic loading of saturated clay. *Canadian Geotechnical Journal*, 26: 122–131. Canadian Science Publishing. doi:10.1139/t89-013.
- L'Heureux, J.S. & Long, M. 2017. Relationship between shear-wave velocity and geotechnical parameters for Norwegian Clays. *Journal of Geotechnical and Geoenvironmental Engineering*, 143(6), 4017013. [https://doi.org/10.1061/\(asce\)gt.1943-5606.0001645](https://doi.org/10.1061/(asce)gt.1943-5606.0001645)
- Johansson, J., Løvholt, F., Andersen, K., Madshus, C. & Aabøe, R. 2013. Impact of blast vibrations on the release of quick clay slides. In *Proceedings of 18th international conference on soil mechanics and geotechnical engineering*, ICSMGE, Paris.
- Johansson, J., Park, J., Madshus, C., & Wersäll, C. 2020. Reducing impact of vibrations from compaction on slope stability. In *EURODYN 2020: Proceedings of the XI International Conference on Structural Dynamics*.
- Quinn, T.A.C., Robinson, S. & Brown, M.J. 2012. High strain rate characterisation of Kaolin and its application to Statnamic pile testing. In *9th International Conference on Testing & Design Methods for Deep Foundations*. Kanazawa, Japan.
- Saygl, G., Madshus, C., Nordal, S. & Engin, H.K. 2017. Numerical modelling of a blast-induced landslide. In *Geotechnical Frontiers 2017. American Society of Civil Engineers*. <https://doi.org/10.1061/9780784480458.040>
- Yang, J.H., Lu, W.B., Jiang, Q.H., Yao, C. & Zhou, C.B. 2016. Frequency comparison of blast-induced vibration per delay for the full-face millisecond delay blasting in underground opening excavation. *Tunnelling and Underground Space Technology*, 51: 189–201. Elsevier BV. doi:10.1016/j.tust.2015.10.036.